AUTHOR: **Salvio Chacko**   DEGREE: **Ph.D.**

TITLE: **Numerical analysis of unsteady heat transfer for thermal management**

DATE OF DEPOSIT: ....

I agree that this thesis shall be available in accordance with the regulations governing the University of Warwick theses.

I agree that the summary of this thesis may be submitted for publication.

I **agree** that the thesis may be photocopied (single copies for study purposes only).

Theses with no restriction on photocopying will also be made available to the British Library for microfilming. The British Library may supply copies to individuals or libraries. subject to a statement from them that the copy is supplied for non-publishing purposes. All copies supplied by the British Library will carry the following statement:

"Attention is drawn to the fact that the copyright of this thesis rests with its author. This copy of the thesis has been supplied on the condition that anyone who consults it is understood to recognise that its copyright rests with its author and that no quotation from the thesis and no information derived from it may be published without the author's written consent."

AUTHOR'S SIGNATURE: ....
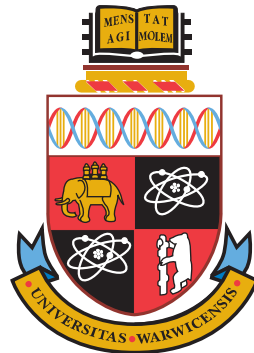

<u>USER'S DECLARATION</u>

1. I undertake not to quote or make use of any information from this thesis without making acknowledgement to the author.

2. I further undertake to allow no-one else to use this thesis while it is in my care.

DATE   SIGNATURE   ADDRESS

....

....

....

....

....

Numerical analysis of unsteady heat transfer for thermal management

by

Salvio Chacko

Thesis

Submitted to the University of Warwick

for the degree of

Doctor of Philosophy

Department of Engineering

October 2012

THE UNIVERSITY OF
WARWICK

THE UNIVERSITY OF WARWICK

School of Engineering and Centre of Scientific Computing

Numerical analysis of unsteady heat transfer for thermal

management

by

SALVIO CHACKO

Supervisor

Dr. Yongmann M Chung

This thesis is submitted in partial fulfilment of the

requirements for the degree of

Doctor of Philosophy in Engineering

October 2012

Abstract

In this study, thermal management of Lithium ion (Li-ion) battery pack used in electric vehicle (EV) is considered. Li-ion cells generate a significant amount of heat during normal operation. Previous study has clearly identified that temperature affects the efficiency, safety, reliability and lifespan of the Li-ion battery. Therefore, a battery thermal management system (BTMS) enabling effective temperature control is essential for safety and overall performance of the Li-ion battery. Two critical aspects are key to design of efficient BTMS: firstly being able to predict the heat generated from Li-ion cells, and secondly to predict how the generated heat is removed though the cooling plate of the BTMS.

To predict the heat generated from the Li-ion cell, a time-dependent, thermal behavior of a Li-ion polymer cell has been modelled for electric vehicle drive cycles with a view to developing an effective battery thermal management system. The fully coupled, new three-dimensional transient electrothermal model has proposed and implemented based on a finite volume method. To support the numerical study, a high energy density Li-ion polymer pouch cell was tested in a climatic chamber for various electric load cycles consisting of a series of charge and discharge rates, and a good agreement was found between the model predictions and the experimental data.

To predict the heat removed, a numerical study has been performed on a cooling plate of a indirect liquid cooled BTMS. The BTMS has a battery cooling plate with coolant flowing through rectangular serpentine channels. The temperature distribution as well as the pressure drop across the battery cooling plate were investigated.

Particular emphasis was placed on the temperature uniformity on the cooling plate surface as the lifespan of a battery is severely affected by non-uniform temperature distribution. From the simulations, it is found that the aspect ratio and the curvature have a significant effect on the surface temperature uniformity, and that a compromise of the battery cooling plate design would be required between the temperature uniformity and the pressure drop penalty.

Thermal management of batteries for high discharge applications, for instance, in hybrid electric vehicle, is more challenging and typically requires turbulent heat transfer. In turbulent heat transfer not only mean temperatures but also temperature fluctuations need to be predicted correctly. For this, a numerical turbulent heat transfer of a triple jet is considered. In this study, a large eddy simulation (LES) technique was applied to predict the unsteady heat transfer behavior of turbulent flow. It is found that LES predicted the correct amplitude of temperature fluctuations which was in good agreement with the available experimental data in terms of mean, RMS, skewness and kurtosis. RANS simulations with two turbulence models were also conducted along with LES. The RANS based turbulence models produced a very small amplitude of fluctuations, and failed to predict the correct magnitude of unsteady thermal fluctuations, highlighting its limitations in unsteady turbulent heat transfer simulations.

Acknowledgement

List of publications

During the course of PhD research, three journal papers and one patent have been submitted for publication.

Paper I: S. Chacko and Y. M. Chung. Thermal modelling of Li-ion polymer battery for electric vehicle drive cycles, Journal Of Power Sources 213: 296-303, 2012.

Paper II: S. Chacko and Y. M. Chung. Laminar conjugate heat transfer of rectangular serpentine channels for EV battery thermal management, Submitted, 2012.

Paper III: S. Chacko, Y. M. Chung, S. K. Choi, H. Y. Nam, and H. Y. Jeong. Large eddy simulation of thermal striping in non-isothermal triple jet. International Journal of Heat and Mass Transfer, 54(19-20):4400-4409, 2011.

Patent: S. Chacko, S. Charmer, An arrangement for battery thermal management, Application no. 1448/mum/2011(India), (Patent Pending).

Contents

List of Figures

List of Tables

1

Introduction

1.1 Background

Environmental regulations, rising energy prices, and increasing public awareness on global warming coupled with government incentives are creating opportunities for alternative powertrain vehicles. Electric Vehicles (EVs) offer zero emissions at point of use and are a route to zero total green house gas as carbon neutral electricity generation develops. It is anticipated that EV penetration in Europe will grow to around 1.2 million cars with around 43 original equipment manufacturers (OEM) and a total of 74 EV models available by 2015 [5]. Research carried out by Boston

Consulting Group (BCG) [6] in 2008 identified that 26% of vehicles would be fully electric by 2020 and that the battery costs would decline by $60 - 65\%$ by 2020. A critical element to the viability of low carbon technology vehicles like EV and HEV is the right selection of power source. The high specific energy and power capability of lithium ion cell enable its use in low carbon vehicle applications.

The implementation of electric vehicle technology is dependent on various factors. The electric car industry, like any new industry, is facing a number of challenges. The major challenge is costs. Battery technology is expensive, and because batteries in electric cars need to be able to hold massive amounts of charge to make the cars practical for most drivers, they have to be built using expensive materials, most of which are tough to procure. Because electric cars cost a lot to build, they also cost more than comparable gasoline cars to buy. That makes consumers reluctant to adopt them. Beyond the costs, electric car makers have a lot of convincing to do with consumers. Not everyone is sold on the idea that electric cars make sense for their life. That's because of range anxiety. And, unless you have access to a specialized charging station (which are currently in short supply), getting a full charge takes around eight hours. To add to it the safety, manufacturing and reliability are also seen as key challenges facing the successful electric vehicle implementation.

So the success of EV/HEV is heavily dependent on the range, efficiency, performance, reliability and life of the Li-ion battery. Li-ion batteries are, however, sensitive to their thermal environment and it is important that their operating temperature is carefully controlled in order to meet the various targets. Charging or discharging Li-ion batteries generates powerful electrical currents, and this in turn generates heat inside the Li-ion cells, which needs to be managed effectively.

1.1.1 Thermal management of Li-ion cells

Current and previous research has clearly identified that temperature affects the battery's ability to charge, provide energy/power to the powertrain, its safety, range, reliability and overall life. It has been observed that the ideal temperature gradient within a battery cell, and from a battery cell to another, is believed to be within 5 to 10°C [7]. Figure 1.1a illustrates the effect of cell temperature on the discharge characteristics of a high capacity EIG Li-ion cell. It is evident that as the ambient temperature changes, the available cell capacity is significantly affected. As the temperature increases the cell capacity rises until about 40°C, beyond which the capacity increase is not substantial. With reduction in temperature the discharge characteristics curve becomes shorter and steeper, leading to reduced cell capacity. It should also be noted that in order to avoid damage to the cell, charging is also severely limited at temperatures much below 0°C.

Figure 1.1b shows the relationship between cell capacity versus cell life for various ambient temperatures for an typical Li-ion cell. The figure shows that the cell life is sensitive to ambient temperature. The characteristic curve becomes shorter with increase in cell temperature leading to reduction in the cell life. The cell has maximum life at 25°C, while the life reduces significantly at higher temperature of 55°C with the cell capacity also reducing below the acceptable level.

Based on the above, it can be concluded that operating Li-ion cells at temperatures further away from 25°C affect the ability to retain the capacity and also effectively reduce the life span. The solution is therefore, to ensure that cell temperatures are kept in the optimum range for the majority of its operating life.

Hence, managing the thermal environment of the Li-ion cells and the overall battery is critical. The battery thermal management system (BTMS) has to maintain the Li-ion cells at the optimum temperature range for maximum performance and
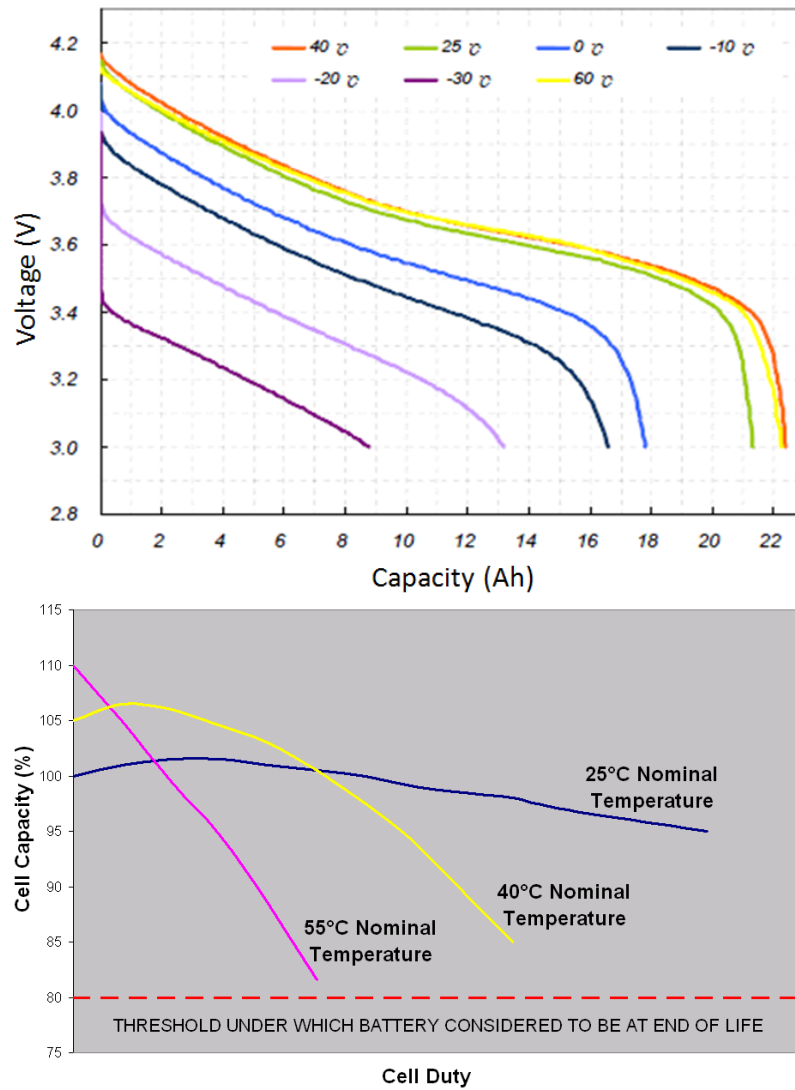
Figure 1.1: Typical effect of temperature on Li-ion cell. a) Capacity, and b) life. (Source: EIG Li-ion cell product data sheet [8])
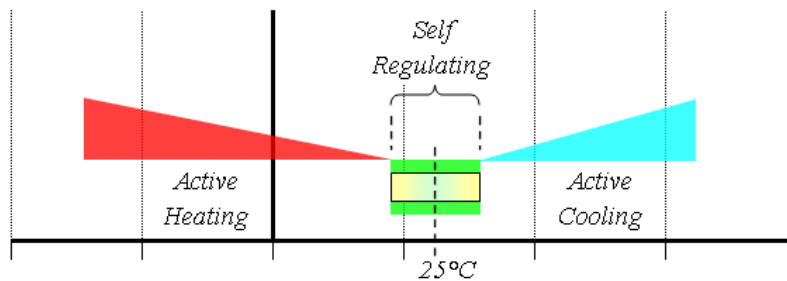
Figure 1.2: Li-ion cell efficiency map-in relation to vehicle operating condition.

life. The ideal operating temperature range is represented by the yellow/green zone
in Figure 1.2. A typical liquid based BTMS [9] controls the Li-ion cell temperature
by flowing conditioned (hot or cold) coolant through the rectangular channels of a
coolant plate. The cell temperature is regulated to the ideal zone by active heating
in a cold ambient and active cooling in a hot ambient. In addition to this, the BTMS
also keeps the temperatures of the individual cells within the battery pack uniform
in order to avoid reduced performance and life.

1.2   Aims and objective

The aim of the current research is to enable advanced thermal management. Op-
timal thermal management systems not only help improve battery performance,
safety and life but also help reduction in parasitic loses thereby increasing vehicle
range. Hence being able to understand the heat rejection from the cell under vari-
ous conditions and heat removed from coolant plate of the BTMS accurately enables
optimum design of a battery thermal management system. Such understanding is
currently dependent on detailed vehicle level testing and heavy instrumentation.
Considering that the tests have to be repeated for varying load, drive cycles and
ambient conditions to gain an overall understanding, the thermal management sys-
tem development is a challenging task.

Currently, there is limited published numerical work, which can predict three di-
mensional unsteady heat generation from a Li-ion cell for various load, drive cycles
and ambient conditions. There is also limited numerical work done on understand-
ing how coolant plate channel parameters like aspect ratio, gap between channels
affect the pressure drop, cell maximum temperature and uniformity. Being able to
predict these two key aspects would help design efficient battery thermal manage-
ment systems. Hence, the main objectives of the current research focus on numerical

modelling of those key aspects:

- Predicting the heat generated by Li-ion cells. This has been covered in Chapter 4.

- Predicting how the generated heat is removed through the cooling plates of the battery thermal management system. This has been covered in Chapter 5 and also in Appendix.

For the heat generation predictions, an electro-thermal numerical model has been proposed and validated for Li-ion cells. The fully coupled, three-dimensional transient electro-thermal model has been implemented for a high energy density Li-ion polymer pouch cell. In terms of predicting heat removal, a laminar flow through serpentine channels of rectangular cross section is modeled to study the conjugate heat transfer through the cooling plate of the thermal management system. In this study, the effect of the aspect ratio and the radius of curvature of the serpentine channel on the thermal performance of the cooling plate was considered. Laminar conjugate heat transfer simulations of a battery cooling plate were carried out at several Reynolds numbers. Laminar flow through serpentine channels enables lower power draw from the batteries, resulting in lower parasitic loses and hence enabling maximum electric vehicle range whilst providing efficient thermal management.

For very high battery discharge applications (*i.e.*, hybrid or range extender vehicles) with onboard conventional engine for continuous battery charging, management of high heat generation would be primary. For maintaining temperature on batteries in the ideal range for such high discharge applications turbulent heat transfer is considered. A numerical turbulent heat transfer problem is studied (due to data available for model validation) for accessing various turbulence modelling methods. Numerical simulations of a non-isothermal triple jet were performed to validate the

numerical model, assess the capability and accuracy of LES along with two other available RANS based models for turbulent heat transfer applications.

1.3   Structure of the thesis

The following provides a brief summary of the subsequent chapters in the thesis.

- **Chapter 2**: This chapter serves as an introduction to the Li-ion technology, understanding on various critical processes and terminology used in Li-ion cells. Also looks at various types commercially available chemistry, types and formats of li-ion batteries for electric/hybrid vehicle application.

- **Chapter 3**: This chapter serves as a review on thermal management for Li-ion batteries, introducing various types of thermal management systems used for electric/hybrid vehicle applications.

- **Chapter 4**: This chapter describes the electro-thermal model developed to predict the thermal behavior of cells. The study also describes the performance testing and Li-ion cell electro-thermal characterisation performed for the validation of the numerical electro-thermal model.

  This work has been published : S. Chacko and Y. M. Chung. Thermal modelling of Li-ion polymer battery for electric vehicle drive cycles, Journal of Power Sources 213: 296-303, 2012.

- **Chapter 5**: This chapter describes the numerical study on a cooling plate with serpentine channels used for battery thermal management. Channels with a rectangular cross section were considered.

  This work has submitted for publication : S. Chacko and Y. M. Chung. Laminar conjugate heat transfer of rectangular serpentine channels for EV battery thermal management, Submitted, 2012.

- **Chapter A**: This chapter describes the numerical study of turbulent heat transfer. Various turbulence models have been used and compared against experimental data for a triple jet.

This work has been published : S. Chacko, Y. M. Chung, S. K. Choi, H. Y. Nam, and H. Y. Jeong. Large eddy simulation of thermal striping in non-isothermal triple jet. International Journal of Heat and Mass Transfer, 54(19-20):4400-4409, 2011.

2

Li-ion cell technology

2.1 Background

In this chapter the concepts related to Li-ion technology is discussed and reviewed. As the environment pollution is a serious problem, automobile manufacturers are forced to shift part of their productions from pure internal combustion systems to new energy saving vehicles [10]. The proposed solution is to produce clean vehicles such as pure EVs, HEVs, plug-in hybrid electric vehicles (PHEV) and fuel cell electric vehicle (FCEV). EVs offer zero emissions at point of use and are a route to

zero total green house gas as carbon neutral electricity generation develops. It has been estimated that electric systems would be widely used in the near future [5, 10].

EV was first built in Britain by Robert Davidson [11] in 1873, nearly 12 years earlier than the first gasoline-powered vehicle. It had an energy source, a power converter, an electric motor and a mechanical transmission. While EV rely completely on batteries for propulsion, HEV combines a internal combustion engine along with an electric propulsion system. FCEVs use fuel cell for propulsion, have high efficiency, low operation noise and little or no emissions [12]. In principle, the electricity used by EVs or the hydrogen used by FCEVs could be generated by clean and CO_2 free processes, using renewable sources such as solar energy or fossil energy with CO_2 capture and storage techniques. EVs, FCEVs remains the only potential zero-emissions-vehicle replacements for the internal combustion engine [13, 14, 15]. That is why they are often regarded as the long-term complete solution to the problem of pollution and energy shortage. EVs, FCEVs create social benefits by generating power without polluting emissions, and HEVs by reducing gasoline combustion. Until now, many researchers have concluded that EVs, HEVs and FCEVs offer the best possibility for the use of new energy sources [12, 10, 16, 13]. Andersen *et al.* [17] have shown that, by using EVs instead of gasoline-consuming vehicles, green house gas (GHG) emissions would be reduced up to 20% and could be further up to 40% as the electric power generated from renewable sources.

2.1.1 Batteries for low carbon vehicles

A critical element to the success of new technologies like EV, HEV vehicles is the right selection of power source. There are numerous rechargeable power batteries such as lead-acid, nickel-based, zinc/halogen, metal/air, sodium-beta and Li-ion [11]. The power battery is by far the largest cost item and a key barrier to the viability of the battery powered vehicles [18, 19]. At the beginning of the 1990s, the lead-acid

battery was available for consideration in electric vehicles because of promising cost
and specific-power characteristics [20]. The lead-acid battery had a poor cycle-life
and significant research has gone to improving its cycle-life performance [20, 21]. In
2000, the UK Foresight Vehicle Programme started with the objective of developing
an optimised lead-acid battery as a solution for HEVs [16]. The market acceptabil-
ity of lead-acid had been limited for battery EVs, prompting active development
of higher-specific energy batteries. Nickel metal hydride (NiMH) batteries started
becoming the next choice for the emerging electric vehicle market [22, 23]. It became
widely used due to its comparatively high specific power, energy and life cycle [24].
In 1991, a Japanese company [25, 26] invented the Li-ion battery which provides
longer cycle life, high energy and power, and higher voltages. The capacity and
power output of Li-ion batteries is over three times that for NiMH batteries and
two times that for lead-acid batteries, leading to its commercially proliferation in
EV/HEV [27, 6, 28] and very recently in FCEV applications [29].

2.1.2   Comparison of available batteries

Several electrical energy storage and conversion devices have been considered for use
in EV/HEV vehicle applications [29, 28]. These are illustrated in Figure 2.1 in the
form of a Ragone plot, wherein the abscissa is specific power (which can be thought
of as acceleration in a vehicle) and the ordinate is specific energy (or range in an EV).
The graph shows these quantities for various batteries, electrochemical capacitors,
and fuel cells. Note that this plot shows specific energy and power on a cell level for
batteries made for many different applications, from consumer electronic to vehicles.
From a performance standpoint, the figure shows that Li-ion batteries are superior
to NiMH batteries for EV/PHEV and HEV applications [30]. The figure also shows
that no battery system has the ability to provide energy close to what is possible
with gasoline (internal combustion engine). Finally, the figure also suggests that
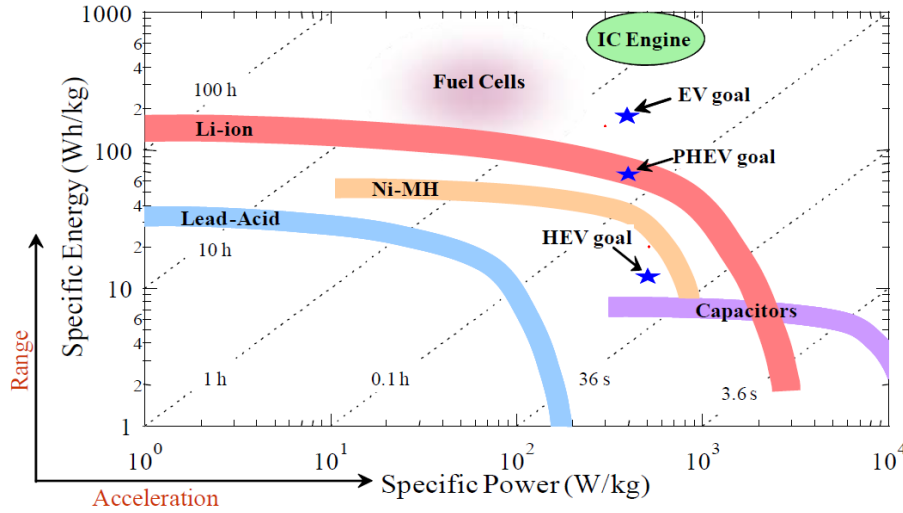
Figure 2.1: Ragone plot of various electrochemical energy storage and conversion devices.(Source: Product data sheets)

batteries are superior to capacitors for applications where the time of discharge is greater than the order of seconds [29].

The United States Advanced Battery Consortium (USABC) has set the requirements needed for batteries to be used in EV, PHEV and HEV applications [31]. These requirements cover a wide range of issues and include energy and power. In order to compare the requirements to the performance of these devices illustrated in Figure 2.1, a few assumptions have to be made, which are done here for the sake of simplicity. While the USABC requirements for power represent a peak power for a 10 s charge/discharge, the systems in Figure 2.1 show average power. Similarly, the USABC requirements show energy as an available energy, which is less than the total energy of the cell. For a HEV, available energy can be as little as $20-30\%$ of the total energy, while for an EV or PHEV, this could be as large as $70-80\%$. Despite these differences, a superposition of the USABC requirements onto Figure 2.1 is illustrative. The figure shows that while Li-ion batteries can easily satisfy HEV requirements, the energy is much smaller than the requirements for EVs. Similarly, the energy needs of a 40 mile PHEV (96 Wh/kg available energy) could be achieved by a high-energy Li-ion cell (similar to the batteries used in the Tesla Roadster)

[32, 33].

While Figure 2.1 captures the performance map of various batteries, other criteria need to be considered, including cost, cycle and calendar life, and safety [34]. For example, while PHEVs appear possible with Li-ion batteries today from an energy standpoint, this would require the use of batteries that are not made for EV applications, and that are cycled over a very wide state of charge (SOC) range, thereby limiting cycle life [35]. One could increase the life by limiting the extent to which these batteries are charged, however, this would limit the energy of the cell, and thereby increase the cost, and the volume and weight of the final battery. Indeed, an analysis of presently-available EV batteries with characteristics that enhance cycle/calendar life suggests that meeting the energy requirements for a 40 mile PHEV is difficult [36]. The typical characteristics of EVs and HEVs power batteries studied are shown in Figure 2.2. It can be seen that the Li-ion batteries have a better performance in terms of energy and power than others [29, 30]. Finally, the importance of

Chemistry Type	Ni-Cd	Ni-MH	Lead acid	Li-ion Cylindrical	Li-ion Prismatic	Li-Po
Nominal Voltage (V)	1.2	1.2	2,1	3.6	3.6 / 3.7	3.6
Specific Energy (Wh/Kg)	50	70	30	80	100-160	140
Specific Energy (Wh/L)	150	200	-	-	250-360	-
Cycle Life	500	560	-	1000	1000	-
Environmental hazard	low	medium	medium	high	high	high
Safety	High	High	medium	low	low	low
Cost	low	medium	low	high	high	high
Self-Discharge Rate (%/month)	25-30	30-35	-	6-9	6-9	-
Memory Effect	yes	yes	yes	no	no	no

Figure 2.2: Performance comparison of power batteries. (Source: [1])

each of these factors like power, energy etc change from application to application. Therefore, while peak power could be an important criterion for an HEV, energy density would be a critical parameter in an EV [24]. Some criteria, such as cost and safety, remain challenges in all applications [18, 34]. While complicated, the interplay between these various factors is tractable and Li-ion batteries remain the most promising candidate for use in vehicular applications. The three main reasons

for this conclusion are the higher energy, higher power, and the potential for lower cost of Li-ion batteries when compared to NiMH batteries [28, 30]. This conclusion has been the reason why significant research efforts have been directed toward Li-ion batteries [32, 37].

2.2   Li-ion cell structure and chemistry

Lithium-ion batteries are comprised of cells that employ lithium intercalation compounds as the positive and negative materials [38]. As a battery is cycled, lithium ions (Li^+) exchange between the positive and negative electrodes. They are also referred to as rocking chair batteries as the lithium ions rock back and forth between the positive and negative electrodes as the cell is charged and discharged [2]. The positive electrode material is typically a metal oxide with a layered structure, such as lithium cobalt oxide ($LiCoO_2$), or a material with a tunneled structure, such as lithium manganese oxide ($LiMn_2O_4$), on a current collector of aluminum foil. The negative electrode material is typically a graphitic carbon, also a layered material, on a copper current collector.

In the charge/discharge process, lithium ions are inserted or extracted from interstitial space between atomic layers within the active materials. The first batteries marketed, and the majority of those currently available, utilize $LiCoO_2$ as the positive electrode material. Lithium cobalt oxide offers good electrical performance, is easily prepared, has good safety properties, and is relatively insensitive to process variation and moisture. More recently lower cost or higher performance materials, such as $LiMn_2O_4$ or lithium nickel cobalt oxide ($LiNi_{1-x}Co_xO_2$), have been introduced, permitting development of cells and batteries with improved performance [37, 18]. The batteries that were first commercialised employed cells with coke negative electrode materials [39]. As improved graphites became available, the interest

has shifted to graphitic carbons as negative electrode materials as they offer higher specific capacity with improved cycle life and rate capability [35, 36].

Intercalation processes

Li-ion batteries typically consist of two electrodes, an anode and a cathode with a separator between them to prevent shorting [40]. The cell is filled with electrolyte. Figure 2.3 illustrates a typical Li-ion cell sandwich consisting of a graphite anode and a $LiCoO_2$ cathode. The electrodes consist of active materials bound together
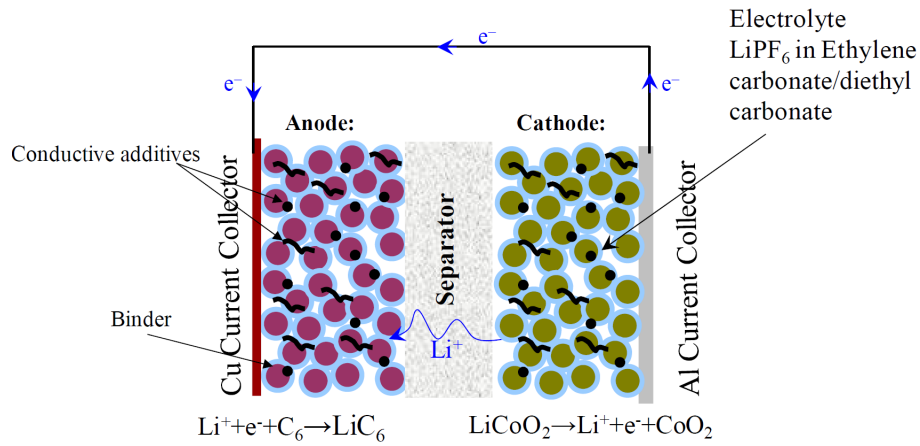
Figure 2.3: Schematic of a typical Li-ion cell.(Source: [1])

with an electronically insulating binder and conductive additives. Each electrode is pasted onto current collectors. During charge, Li is removed from the cathode (or positive electrode), transferred through the separator via the electrolyte and is inserted into the anode [41]. The reverse occurs on discharge. The difference in voltage of the cathode and anode is the cell voltage. The amount of Li that is stored in each of these materials is related to the capacity (often given in mAh/g). The product of the voltage and the capacity is the energy. How quickly the Li is transferred from one electrode to the other (or how quickly the energy is removed) is related to the power [38].

Figure 2.4 shows the typical steady-state charge (constant current) of the anode and cathode of a Li-ion cell with a graphite anode and a $LiCoO_2$ cathode in an organic electrolyte consisting of a Li salt (lithium hexafluoro phosphate, $LiPF_6$) in a solvent (e.g., ethylene carbonate and diethyl carbonate) [37]. This is the battery
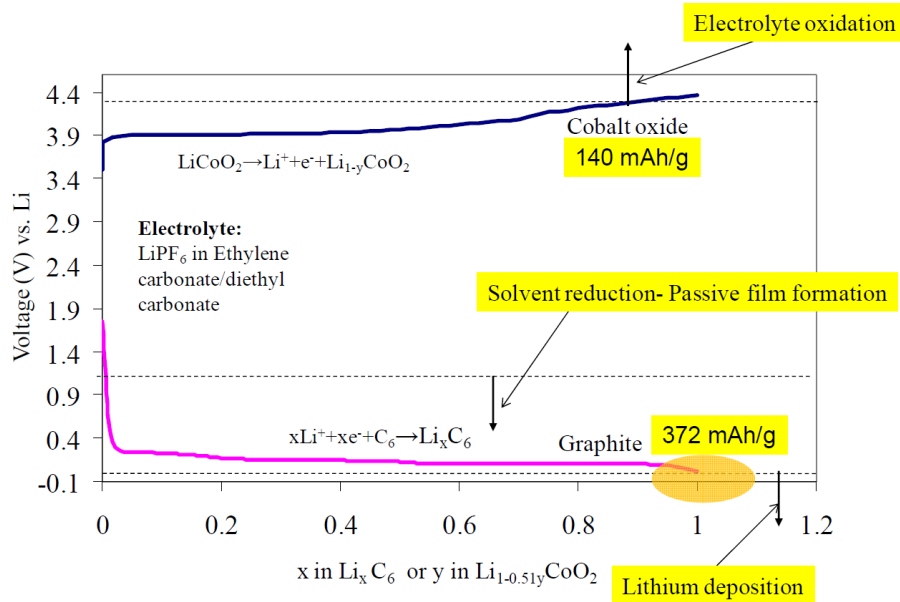
Figure 2.4: Steady state charge curve of a Li-ion cell.(Source: [1])

used in laptops and cell phones [28]. The voltage of each electrode is represented with respect to a Li-metal reference electrode. As the Li is removed from the cathode, its potential increases, while the potential of the anode decreases with insertion of Li. The process of Li moving in and out of the electrodes is referred to as intercalation/deintercalation. The voltage of the battery is the difference in voltage of the cathode and the anode, which increases as charge proceeds. The abscissa represents how much Li is stored in the cell, while the ordinate shows at what voltage the Li is inserted/removed from the materials. In order to increase the energy of the battery three avenues can be pursued, namely:

- Increase the voltage of the cathode

- Decrease the voltage of the anode

• Increase the capacity of the cell

However, the thermodynamics of electrochemical reactions other than the intercalation of Li (referred to as side reactions) limits these quantities [41]. The three side reactions worth mentioning in this figure are the oxidation of the solvent that occurs above 4.2 V, Li-metal deposition that occurs below 0 V, and solvent reduction that occurs below 1 V . These reactions not only limit the energy of the cell, but they are also implicated in the life and safety problems associated with Li-ion batteries. Fortunately, it has been observed that Li can intercalate into many different anode and cathode materials. At present, three classes of cathodes, four classes of anodes, and four classes of electrolytes are being considered for use in Li-ion cells. Depending on the combination of the anode, cathode, and electrolyte, one can have a completely new battery with changes to the energy, power, life, safety characteristics and low temperature performance [39, 34]. These classes are illustrated in Figure 2.5 for the three components of the battery.
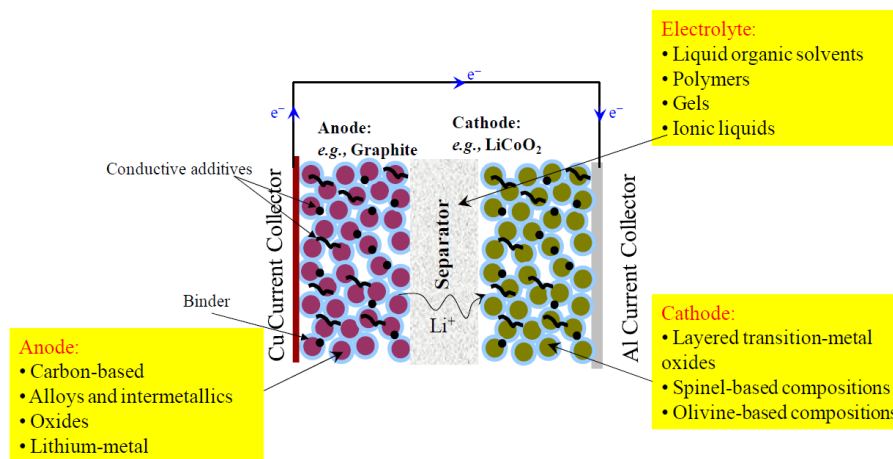
Figure 2.5: Schematic of a Li-ion cell with the various anode, cathode, and electrolytes that are presently being considered. Changing the combination results in changes to the energy, power, safety, life, and cost.(Source: [1])

2.3   Li-ion performance characteristics

A few key parameters used to define Li-ion performance characteristics are described
below [38]:

- Energy density: The energy density of a battery is a measure of how much
  energy the battery can supply relative to its weight or volume. A battery with
  an energy density twice that of another battery should, theoretically, have an
  active lifetime twice as long.

- Energy per mass: It is the gravimetric energy density of a battery.

- Energy per volume: It is the volumetric energy densities of a battery.

- Voltage profiles: The voltage profile of a battery is the relationship of its
  voltage to the length of time it has been discharging (or charging). In most
  primary batteries, the voltage will drop steadily as the chemical reactions in
  the cell are diminished [40]. At some point near the end of the cycle, the
  voltage drops sharply to nearly zero volts.

- Self-discharge rates: All charged batteries (except thermal batteries and other
  batteries specifically designed for a near-infinite shelf life) will slowly lose their
  charge over time, even if they are not connected to a device. Moisture in the
  air and the slight conductivity of the battery housing will serve as a path for
  electrons to travel to the cathode, discharging the battery. The rate at which
  a battery loses power in this way is called the self-discharge rate [42].

- Operating temperature: As a general rule, battery performance deteriorates
  gradually with a rise in temperature above 25°C, and performance deteri-
  orates rapidly at temperatures above 55°C [43]. At very low temperatures
  −20°C to 0°C, battery performance is only a fraction of that at 25°C. At low

temperatures, the loss of energy capacity is due to the reduced rate of chemical reactions and the increased internal resistance of the electrolyte. At high temperatures, the loss of energy capacity is due to the increase of unwanted, parasitic chemical reactions in the electrolyte. Li-ion batteries as a general rule have a recommended temperature range of 25°C to 45°C [44, 7].

- Cycle life: The cycle life of a battery is the number of discharge/recharge cycles the battery can sustain, with normal care and usage patterns, before it can no longer hold a useful amount of charge [45, 19].

Many factors influence the operational characteristics, capacity, energy output and performance of a battery. The effect of these factors on battery performance is discussed:

Voltage Level

Voltage of a cell or battery is an important parameter, and there are several different references:

- The theoretical voltage is a function of the anode and cathode materials, the composition of the electrolyte and the temperature (usually stated at 25°C) [46].

- The open-circuit voltage is the voltage under a no-load condition and is usually a close approximation of the theoretical voltage.

- The closed-circuit voltage is the voltage under a load condition.

- The nominal voltage is one that is generally accepted as typical of the operating voltage of the battery as, for example, 1.5 V for a zinc-manganese dioxide battery.

- The working voltage is more representative of the actual operating voltage of the battery under load and is lower than the open-circuit voltage.

- The average voltage is the voltage averaged during the discharge.

- The midpoint voltage is the central voltage during the discharge of the cell or battery.

  The end or cut-off voltage is designated as the end of the discharge. Usually it is the voltage above which most of the capacity of the cell or battery has been delivered. The end voltage may also be dependent on the application requirements [47, 48].

When a cell or battery is discharged its voltage is lower than the theoretical voltage. The difference is caused by internal resistance (IR) losses due to cell (and battery) resistance and polarization of the active materials during discharge. This is illustrated in Figure 2.6. In the idealized case, the discharge of the battery proceeds at the theoretical voltage until the active materials are consumed and the capacity is fully utilized. The voltage then drops to zero. Under actual conditions, the discharge curve is similar to the other curves in Figure 2.6. The initial voltage of the cell under a discharge load is lower than the theoretical value due to the internal cell resistance and the resultant IR drop as well as polarization effects at both electrodes [41]. The voltage also drops during discharge as the cell resistance increases due to the accumulation of discharge products, activation and concentration, polarization, and related factors. Curve 2 is similar to curve 1, but represents a cell with a higher internal resistance or a higher discharge rate, or both, compared to the cell represented by curve 1 [49, 50]. As the cell resistance or the discharge current is increased, the discharge voltage decreases and it shows a more sloping profile. The specific energy that is delivered by a battery in practice is, therefore, lower than the theoretical specific energy of its active materials, due to:
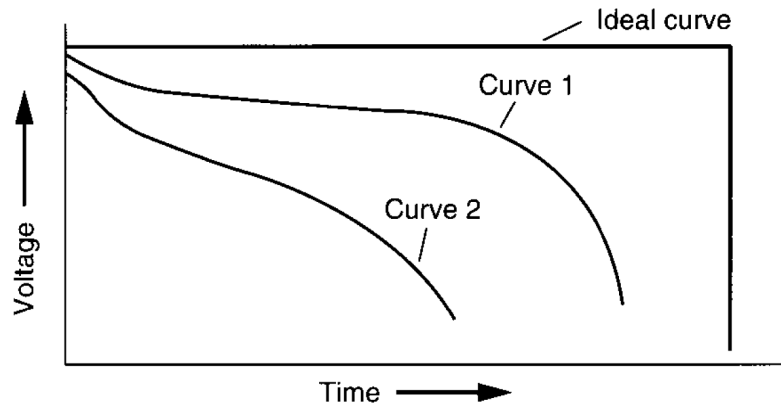
Figure 2.6: Characteristics of discharge curve Source.(Source: [2])

• The average voltage during the discharge is lower than the theoretical voltage.

• The battery is not discharged to zero volts and all of the available ampere-hour capacity is not utilized.

As specific energy equals watthours/gram = voltage × ampere hours/gram,the delivered specific energy is lower than the theoretical energy as both of the components of the equation are lower.

Mode of Discharge (Constant Current, Constant Load,Constant Power)

The mode of discharge of a battery, among other factors, can have a significant effect on the performance of the battery [51]. For this reason, it is advisable that the mode of discharge used in a test or evaluation program be the same as the one used in the application for which it is being tested. A battery, when discharged to a specific point (same closed-circuit voltage, at the same discharge current, at the same temperature) will have delivered the same ampere-hours to a load regardless of the mode of discharge. However, as during the discharge, the discharge current will be different depending on the mode of discharge, the service time or hours of discharge delivered to that point (which is the usual measure of battery performance) will,

likewise, be different [19]. Three of the basic modes under which the battery may be discharged are:

- Constant resistance: The resistance of the load remains constant throughout the discharge. (The current decreases during the discharge proportional to the decrease in the battery voltage)

- Constant current: The current remains constant during the discharge. C rate is a common method for indicating the discharge at constant current, as well as the charge current of a battery, is the C rate, expressed as $I = M \times C_n$, where $I=$ discharge current(A), $C =$ numerical value of rated capacity of the battery in ampere-hours (Ah), $n =$ time in hours, for which rated capacity is declared, $M =$ multiple or fraction of C.

- Constant power: The current increases during the discharge as the battery voltage decreases, thus discharging the battery at constant power level (power = current $\times$ voltage).

In the constant-current mode, the current is maintained at a level such that the power output at the cutoff voltage is equal to the level required for acceptable equipment performance. Thus both current and power throughout the discharge are lower than for the constant resistance mode [52]. The average current drain on the battery is lower and the discharge time or service life to the end of the battery life is longer. In the constant-power mode, the current is lowest at the beginning of the discharge and increases as the battery voltage drops in order to maintain a constant-power output at the level required by the equipment. The average current is lowest under this mode of discharge, and hence, the longest service time is obtained. It should be noted that the extent of the advantage of the constant-power discharge mode over the other modes of discharge is dependent on the discharge characteristics

of the battery [38]. The advantage is higher with battery systems that require a wide voltage range to deliver their full capacity.

Temperature of Battery During Discharge

The temperature at which the battery is discharged has a pronounced effect on its service life (capacity) and voltage characteristics. This is due to the reduction in chemical activity and the increase in the internal resistance of the battery at lower temperatures [53]. This is illustrated in Figure 2.7, which shows the test data for voltage variation with capacity at different temperatures for an A123 20 Ah cell (see Section 4.3.1 for test procedure details). It is evident that the cell capacity(Ah) varies with temperature. Lowering of the ambient temperature results in a reduction of capacity as well as an increase in the slope of the discharge curve. Both the specific characteristics and the discharge profile vary for each battery system, design, and discharge rate, but generally best performance is obtained between 20 and 40°C [44]. At higher temperatures, the internal resistance decreases, the discharge voltage increases and, as a result, the ampere-hour capacity and energy output usually increase as well. On the other hand, chemical activity also increases at the higher temperatures and may be rapid enough during the discharge (a phenomenon known as self-discharge) to cause a net loss of capacity [54]. Again, the extent is dependent on the battery system, design and temperature [55]. As the discharge rate is increased, the battery voltage (for example, the midpoint voltage) decreases; the rate of decrease is usually more rapid at the lower temperatures. Similarly, the batterys capacity falls off most rapidly with increasing discharge load and decreasing temperature. Again, as noted previously, the more stringent the discharge conditions, the greater the loss of capacity. However, discharging at high rates could cause apparent anomalous effects as the battery may heat up to temperatures much above ambient, showing the effects of the higher temperatures [2].

Temperature (°C)	Discharge Capacity (Ah)
-9	18.1
0	18.6
22	19.5
39	19.9
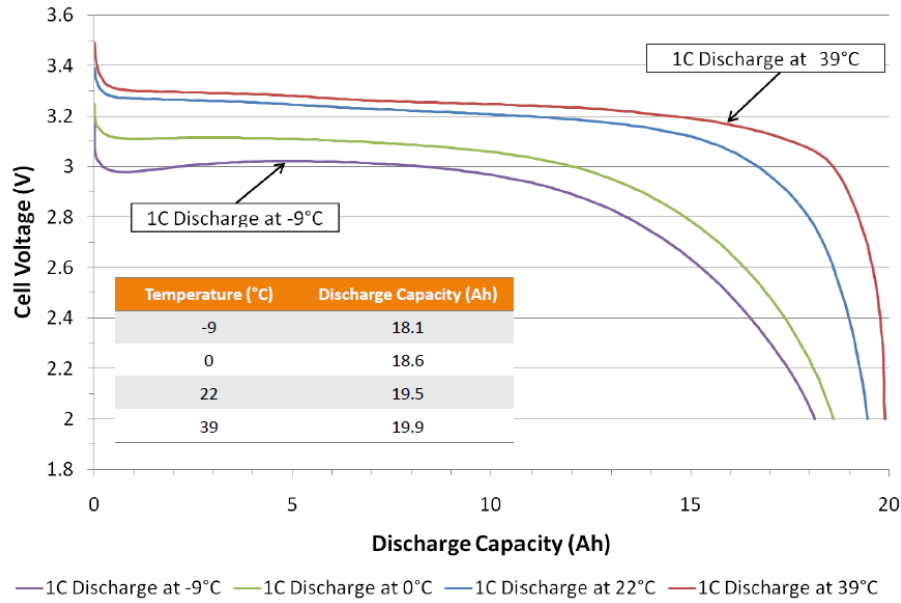
Figure 2.7: A123 20 Ah test data illustrating the effect of temperature.

2.3.1 Li-ion cell types based on chemistry

A variety of materials can be paired with carbon-based negatives in battery cells by using organic electrolytes [38]. Mixed with carbon for increased conductivity and with binders, these materials are deposited on thin aluminum sheets as conducting supports .

- $LiCoO_2$: Lithiated cobalt oxide is the main component of the positive electrodes in lithium-ion cells produced on a very large scale for consumer product applications. It has good storage capacity for lithium ions, adequate chemical stability, and good electrochemical reversibility [54]. However, it is relatively more expensive per kilowatt-hour of storage capacity than other oxides and is therefore not a good candidate for automotive applications of lithium-ion batteries that are under severe cost constraints.

- $Li(Ni_{0.85}Co_{0.1}Al_{0.05})O_2$: Commonly termed NCA, this lithiated mixed oxide of nickel, cobalt, and aluminum has become accepted for batteries in prototypical

HEV, full performance battery electric vehicle, and the PHEV. It approaches the favorable characteristics of $LiCoO_2$ at a lower per-kilowatt-hour cost [51].

- $Li(Ni_{1/3}Co_{1/3}Mn_{1/3})O_2$: Often termed NCM, this lithiated mixed oxide of nickel, cobalt, and manganese is potentially less expensive than NCA. It can be charged to two cell voltage levels. At the higher voltage (e.g., $4.1 - 4.2$ V), NCM yields excellent storage capacity and relatively low per-kilowatt-hour cost but tends to degrade through the dissolution of manganese; at lower voltage, its capacity is substantially less and the per-kilowatt-hour cost is higher, but stability appears adequate [40].

- $LiMnO_2$: Lithium manganese spinel, denoted LMS, is more stable than cobalt oxide and nickel oxide-based positives in lithium-ion cells because the spinel crystal structure is inherently more stable and has no or little excess lithium ions in the fully-charged state. Thus, it provides very little lithium for undesirable lithium metal deposition on the negative electrode in overcharge [38]. Also, the threshold of thermal decomposition of the charged (lithium-depleted) material is at a considerably higher temperature than that of other positive electrode materials. Despite its lower specific capacity, the expected substantially lower per-kilowatt-hour cost will make LMS attractive, if the efforts to stabilize the material against electrochemical dissolution of its manganese content are successful [54].

- $LiFePO_4$: Lithiated iron phosphate (olivine), denoted LFP, is now being used successfully as a potentially lower-cost positive electrode material. Because of its lower electrochemical potential, LFP is less likely to oxidize the electrolyte solvent and thus is more stable, especially at elevated temperatures [34]. Doping is used to increase the conductivity and stability of this promising material. The electrolyte used in lithium-ion battery cells is a solution of a fluorinated lithium salt (typically LiPF6) in an organic solvent, enabling current trans-

port by lithium ions. Separators are usually micro-porous membranes made of polyethylene or polypropylene. Because of the low conductivity of organic electrolytes, adequate cell and battery power can be realized only with electrodes and separators that are much thinner than those used in aqueous-electrolyte batteries. The need for thin electrodes has made spiral winding of positive electrode-separator negative electrode composites the preferred method for the fabrication of lithium-ion cells, but flat cell configurations packaged in soft plastic (often metallized) enclosures are now gaining acceptance [18].

2.3.2   Li-ion cell advantage and disadvantages

The major advantages and disadvantages of Li-ion batteries, relative to other types of batteries, are summarized in Table 2.1. The high specific energy (150 Wh/kg) and energy density (400 Wh/L) of commercial products makes them attractive for weight or volume sensitive applications. Li-ion batteries offer a low self-discharge rate (2% to 8% per month), long cycle life (greater than 1000 cycles) and a broad temperature range of operation (charge at 20°C to 60°C, discharge at 40°C to 65°C), enabling their use in a wide variety of applications [48]. A wide array of sizes and shapes is now available from a variety of manufacturers. Single cells typically operate in the range of 2.5 to 4.2 V, approximately three times that of NiCd or NiMH cells, and thus require fewer cells for a battery of a given voltage. Li-ion batteries can offer high rate capability. Discharge at 5C continuous, or 25C pulse, has been demonstrated. The combination of these qualities within a cost effective, hermetic package has enabled diverse application of the technology [38].

A disadvantage of Li-ion batteries is that they degrade when discharged below 2 V and may vent when overcharged as they do not have a chemical mechanism to manage overcharge, unlike aqueous cell chemistries. Li-ion batteries typically employ management circuitry and mechanical disconnect devices to provide protec-

Table 2.1: Advantage and disadvantage of Li-ion batteries.(Source: [2])

Advantage
Sealed no maintenance required temperature
Long cycle life
Broad temperature range of operation
Long shelf life
Low self discharge rate
Rapid charge capability
High rate and power discharge capability
High coulombic and energy efficiency
High specific energy and energy density
No memory effect
Disadvantage
Moderate initial cost
Degrades at high temperature
Need for protective circuitry
Capacity loss or thermal runaway when overcharged
Venting and possible thermal runaway when crushed
Cylindrical designs offer lower power density than NiMH

tion from over-discharge, overcharge or over temperature conditions [51]. Another disadvantage of Li-ion products is that they permanently lose capacity at elevated temperatures (65°C), albeit at a lower rate than most NiCd or NiMH products [30, 56, 57].

2.4   Cell format

The Li-ion cells are made up of coated metal electrodes, a separator and an electrolyte . Both the positive and negative electrodes store Li-ions, and the separator, which is non-electrically conductive, insulates them but allows for the transport of Li-ions between the electrodes. The electrolyte has the organic solvent, which promotes the transport of the Li-ions which generates an electric current [54]. Li-

ion cells come in different formats which are predominantly cylindrical, prismatic or pouch type. Figure 2.8 shows the commercially available Li-ion cell formats. Cylindrical cells have an anode, separator and cathode rolled up and inserted into
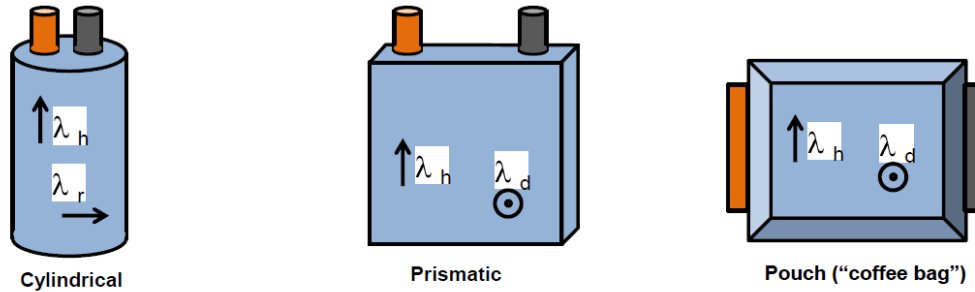
Figure 2.8: Different types of commercially available Li-ion cell formats.

a cylindrical housing usually made of aluminium, while prismatic cells can be rolled or layered but are flat packed in a housing. Due to their shape, cylindrical cells
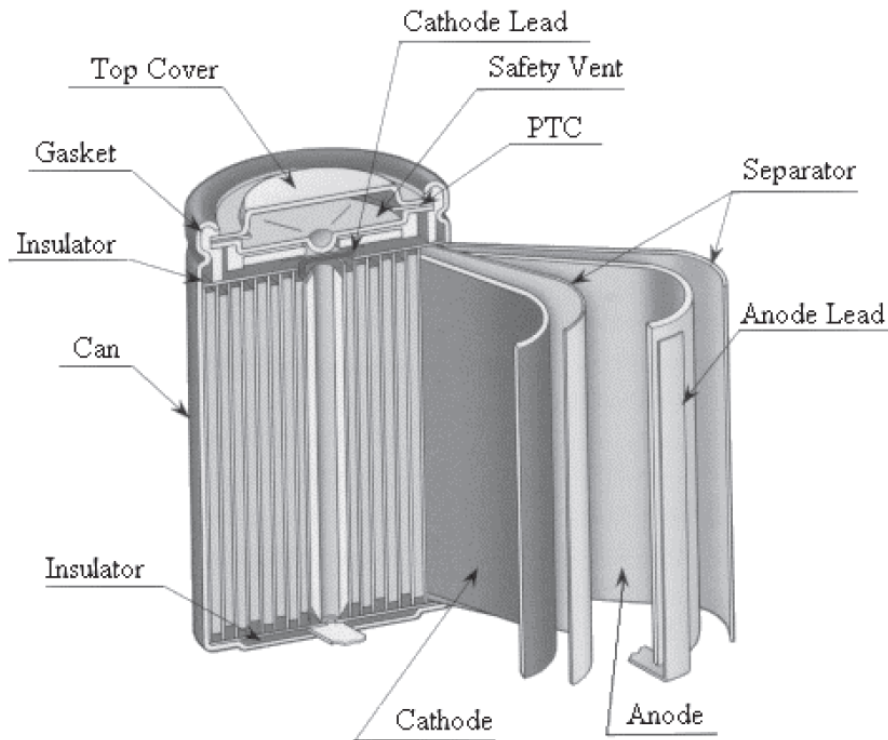
Figure 2.9: Schematic diagram of a wound cylindrical cell.(Source: [2])

are robust at the cell level, but as they get larger their external surface area to volume ratio decreases, thus reducing the heat transfer effectiveness and increasing

temperature gradient. The pouch or prismatic cell has a higher surface area to volume ratio which is better for heat transfer. The pouch cells have individual layers of active material, similar to the prismatic cell, but packed in a flexible composite aluminium film. The construction of a cylindrical wound Li-ion cell is illustrated in Figure 2.9. Prismatic or pouch cells can also be packaged with a better volume efficiency compared to cylindrical cells, and can be better integrated with the thermal management system for a reasonable cost [18]. The fabrication of wound prismatic cells is similar to cylindrical versions except that a flat mandrel is used instead of a cylindrical mandrel [51, 58]. A schematic diagram of a wound prismatic cell is shown in Figure 2.10. The construction consists of a positive and negative electrode
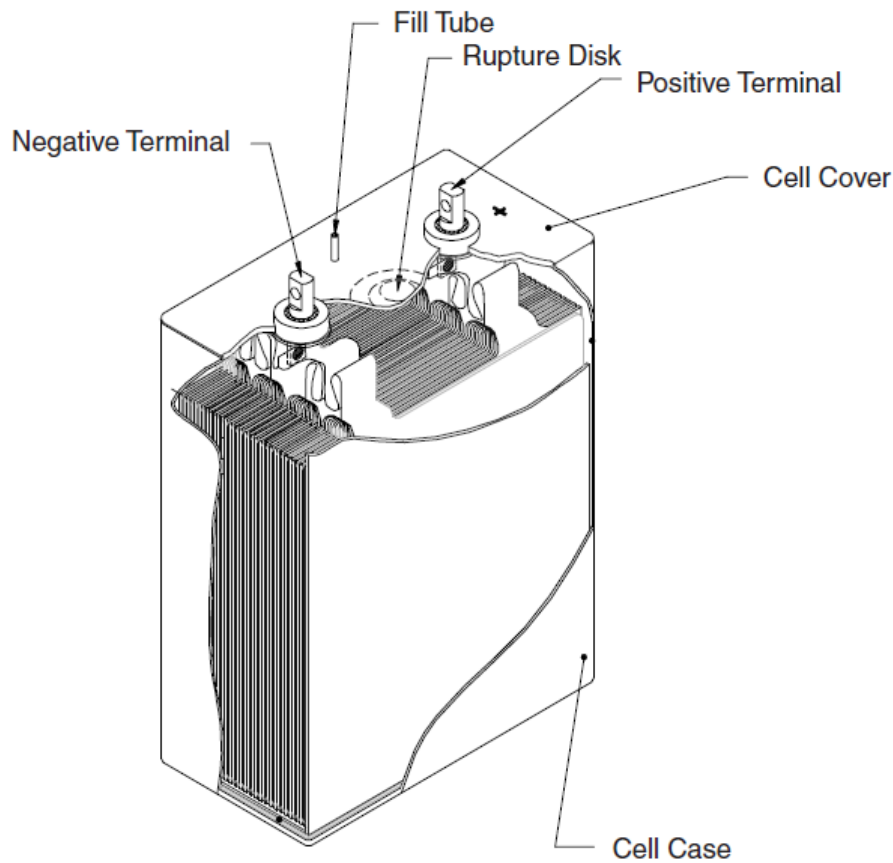
Figure 2.10: Schematic diagram of a wound prismatic cell.(Source: [2])

separated by a 16 μm to 25 μm thick micro porous polyethylene or polypropylene separator. Positive electrodes consists of 10 μm to 25 μm Al foil coated with the

active material to a total thickness typically 180 μm. Negative electrodes are typi-
cally 10 μm to 20 μm Cu foil coated with a carbonaceous active material to a total
thickness 200 μm. The thin coatings and separator are required because of the low
conductivity of non-aqueous electrolytes, 10 mS/cm, and slow Li diffusion in the
positive and negative electrode materials, about 10^{-10} m^2/s. Typically a single tab
at the end of the wind is used to connect the current collectors to their respective
terminals [41]. The case, commonly used as the negative terminal, is typically Ni
plated steel. When used as the positive terminal, the case is typically aluminum.
Most commercially available cells utilize a header that incorporates disconnect de-
vices, activated by pressure or temperature, such as a safety vent [59, 18]. One
design is illustrated in Figure 2.10. These devices can limit cell performance at
high rates, *i.e.*, in a typical 18650 cell, 12A discharge results in disconnect after 20
seconds once the temperature of the disconnect device reaches 70°C due to resistive
heating. The header-can seal is typically formed through a crimp.

We have performed a number of examinations on pouch and cylindrical cells
to compare internal structure. Figure 2.11 shows a cylindrical Li-ion cell stripped,
opened and unrolled. The cell must be fully discharged first if the cell is to be opened
in air and a suitable fume cabinet is needed to clear volatile organic solvents. The
basic structure is consistent across most designs, using electrodes of approximately
$100 - 150$ microns thickness coated on 20 μm foil of either copper for the negative
electrode or aluminium for the positive. There are usually $20 - 30$ of each elec-
trode polarity in a pouch cell. These are interleaved with micro-porous separator of
approx. 20 μm thickness.

2.4.1   Cell layout

Virtually every manufacturer has worked individually and with battery suppliers
to develop Li-ion chemistries that are much more abuse tolerant, as well as being
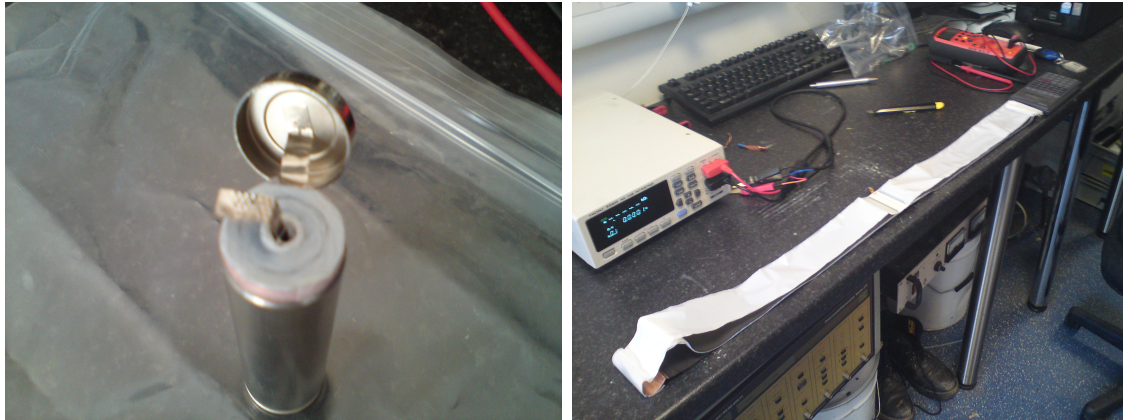
Figure 2.11: Cylindrical cells with a) mandrel header opened b) unrolled anode, separator and cathode.

more durable and reliable [28]. Still, there are substantial tradeoffs between these automotive-grade Li-ion chemistries. Table 2.2 provides a summary of the more prominent Li-ion cell designs that have developed [32]. In Tata Vista EV, (Figure

Type	Cathode (all include Li)	Anode	Cathode voltage (approx.)	Cell Structure	Battery Developer	OEM customers
NCA	Nickel cobalt aluminum oxide	Graphite	3.6v	Cylindrical	Johnson Controls/Saft	Mercedes, BMW HEV
				Prismatic – metal can	PEVE	Toyota
LMO	Manganese spinel	Graphite	3.7v	Pouch	LG Chem	GM, Ford
				Pouch	AESC (NEC & Nissan)	HEV & Nissan Leaf
				Cylindrical	HVE (Hitachi)	Future GM HEVs
LTO	Manganese spinel	Li Titanium Oxide	2.5v	Prismatic	EnerDel	Think City EV
LFP	Iron Phosphate	Graphite	3.3v	Pouch	A123	Fisker PHEV
				Cylindrical	A123	BMW, Mercedes HEV
NMC	Nickel manganese cobalt		3.6v	Prismatic – metal can	Sanyo	VW, Suzuki HEVs Future Toyota HEVs
				Prismatic – metal can	SB LiMotive (Samsung & Bosch)	BMW
	LMO-NMC blend	Graphite	3.7v	Prismatic	Lithium Energy Japan (GS-Yuasa & Mitsubishi)	Mitsubishi
				Pouch	SK Energy	

Table 2.2: Properties of Li-ion cells used by vehicle manufacturers.

2.12) Li-ion pouch cells are used. These Li-ion pouch cells are stacked together

Figure 2.12: Tata Indica Vista EV.

to make a module [9]. A set of these modules are then used to make the complete battery pack [60]. Figure 2.13 shows how two distinct battery boxes, each containing six modules, are housed in the Vista EV battery tray. The battery tray is used to house the packs and is securely mounted on to the Vista EV chassis as in Figure 2.14. Figure 2.15, 2.16 show the battery packs layout of commercially available EVs, Nissan Leaf and Mitsubishi iMiev, respectively. The battery pack is made of modules built from prismatic cells. These EVs have the battery packs mounted on to the vehicle chassis directly.

There are a number of challenges that are likely to impact lithium supply in the future. Availability of raw material and cost is one of the key challenges. Although there is sufficient amount of lithium resources available globally to meet the demand. This poses an inherent risk due to the accessibility of the raw material that is available only in a specific geography. Unrest or instability of the governments in these regions can greatly affect the supply and have impact on the battery price

---

[1]http://www.green.autoblog.com/
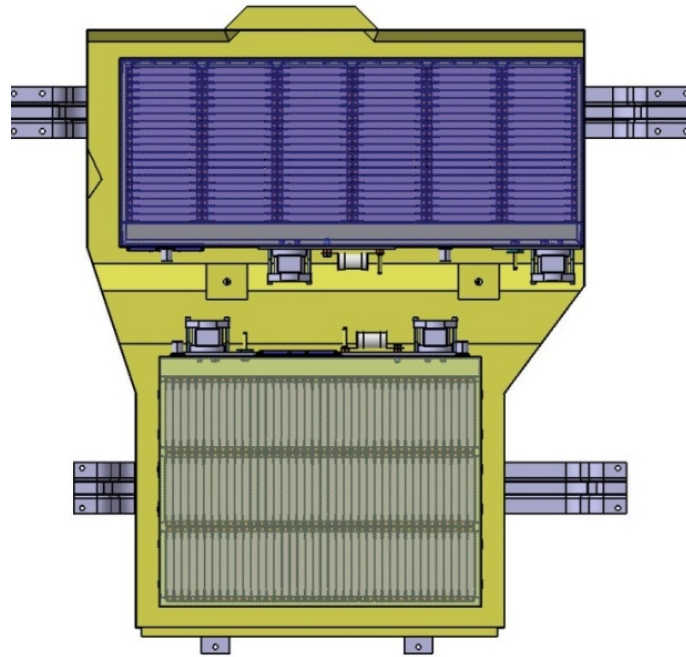
Figure 2.13: Vista EV battery tray (housing the li-ion pouch battery pack)layout.
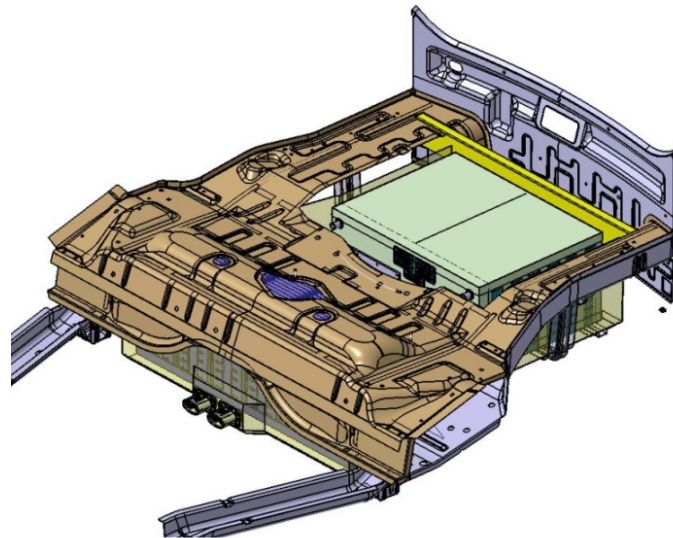
Figure 2.14: Vista EV battery tray chassis installation.

and in turn, the vehicle cost. OEMs are looking at overcoming the dependency on lithium through reuse of lithium batteries in other applications (second-life) and through recycling the batteries once they have completed their lifecycle. Specialised processes and dedicated small scale recycling plants closer to vehicle manufacturers are likely to be the trend in the future. The main challenge hindering the industry

Figure 2.15: Nissan leaf cell layout.[1]

Figure 2.16: Mitsubishi iMiev cell layout.[2]

is the long-term nature of financial investments required by market participants to develop specialised waste disposal services. As the market is still unexplored, the specific impacts and overall profitability of these investments are unknown and thereby create ambiguity and uncertainty about making such commitments.

The commercially available EVs have Li-ion cells of different chemistry/formats [32]. In the current research an overall Li-ion cell performance evaluation experiment is performed on various types of cell chemistry/formats for initial understanding of the cell electro-thermal behavior. Based on the initial understanding a detailed electro-thermal cell charaterisation experiments is derived and performed on a Li-ion pouch cell.

The thesis describes all the experimental work conducted towards Li-ion cell electro-thermal model development and validation in Chapter 4. Section 4.3.1 explains in detail the overall cell performance evaluation experiments. The overall cell performance evaluation is based on international standard IEC62660-1:2010 [61]

with an intent to gain insights into the overall cell electro-thermal behaviour for different chemistry/format. Section 4.3.2 describes the experimental setup/test cycle and results of the detailed electro-thermal charatersation experiments to support Li-ion cell model development and validation.

---

[2]http://www.green.autoblog.com/

3

Battery thermal management

3.1 Introduction

Now, thermal management concepts and its implementation for Li-ion batteries in EV/HEV applications is discussed and reviewed. The safety, efficiency, reliability and lifespan of the Li-ion battery is key to the success of low carbon vehicles like EV/HEV. It is well known that Li-ion cells are sensitive to their thermal environment in which they operate. It is important that their operating temperature is controlled in order to meet the vehicle performance targets.

Li-ion cells generate heat during both charge and discharge, and this should be removed effectively to prevent a severe temperature increase within the cell. It was found that every degree of cell temperature rise reduces the lifespan of the Li-ion battery by approximately two months in an operating temperature range of $30-40°C$ [43]. The cell temperature difference should be kept between $5-10°C$ [62, 63] to achieve a full lifespan, as large temperature non-uniformity in the battery pack affects adversely overall cell lifespan as well as available cell capacity [64, 52, 53, 34]. Therefore, a battery thermal management system enabling effective temperature control becomes essential for overall cell performance and life [55].

During battery charge/discharge, various chemical and electrochemical reactions take place. Selman *et al.* [65] have indicated that the temperature increase in the scaled-up cells is a major concern when the cells are operated at high discharge rates. The batteries generate much more heat during rapid charge and discharge cycles at high current levels, such as during quick acceleration of the vehicle [66]. The improvement of battery-powered vehicles needs large-scale battery; however, with the size increasing and large packages forming, serious thermal stability problems will be posed [67].

The performances of EVs, HEVs and PHEVs are very dependent on batteries. Hence it is very important to know the mechanism of the degradation of the batteries performance in high temperature and high discharge current. In Li-ion battery, heat may generate in the solid electrolyte interface (SEI) film, electrolyte and anode decomposition, the reaction of cathode and electrolyte, the reaction of cathode and adhesive [57]. Excessive local temperature rise may also cause reduction of cycle life and thermal runaway [68]. To achieve a good balance between performance and life, the best operating temperature for Li-ion batteries ranges between 25 and 40°C, and temperature distribution from module to module is below 5°C [69]. As temperature above 50°C will lower the charging efficiency or lower the longevity properties, heat

control is an important issue for Li-ion and other batteries [70].

In general, temperature affects the battery performance including:

- Electrochemical system,

- Round trip efficiency,

- Charge acceptance,

- Power and energy capability,

- Reliability, and

- Cycle life and cost [69]

Based on the above analysis, there are two main problems caused by temperature increase. The first is that the high temperature during charge and discharge can lead to the possibility that temperatures will exceed permissible levels and decrease the battery performance. Another is that the uneven temperature distribution in the battery pack will lead to a localized deterioration. Thereof, temperature uniformity, within a cell and from cell to cell, is important to achieve maximum cycle life of cell, module, and pack [71].

To optimize the performance of a battery and pack/module, the thermal energy management system should achieve the following objectives.

- Optimum operating temperature range for every cell and all battery modules, rejecting heat in hot climates/adding heat in cold climates.

- Small temperature variations within a cell and module.

- Small temperature variations among various modules.

- Compact and lightweight, easily packaged, reliable, low-cost and easy for service.

- A provision for ventilation if the battery generates potentially hazardous gases.

3.2   Literature review

The key to efficient thermal control is to maintain the battery within an ideal temperature zone where it would be self regulating. Below this temperature the battery would require heating, and above this temperature cooling [44, 7].

The batteries such as Li-ion batteries have high power density, but their power is severely limited at $-30°$C [72]. If the battery is operated at a very low temperature such as $-30°$C in cold winter, the battery must be heated rapidly after a cold startup. Nelson *et al.* [73] noted that for a 25 kW delivering power, only 5 kW could be supplied by the battery at $-30°$C. The battery could not heat itself that rapidly with I^2R heating. In such a case, external heating the battery must be considered, and they suggested two ways [44] to rapid heating:

- With electric heaters within the battery,

- By heating the battery coolant with heat transferred from the engine coolant.

The thermal management system may be passive [68] (*i.e.*, only the ambient environment is used) or active [7](*i.e.*, a built-in source provides heating and/or cooling), and can be also divided into four categories based on medium.

- Air based heat/cooling/ventilation (See Figure 3.1)

- Liquid based cooling/heating (See Figure 3.3)

- Phase change materials (PCM) (See Figure 3.7)

- Combination of above.

3.2.1   Air based thermal management

Considering the use of air for battery thermal management may be the simplest approach, and air cooling systems are used for EV/HEV because of cost and space limitations. Figure 3.1 shows an example for both passive and active means of air cooling. Figure 3.1a shows a passive means of cooling where the ambient air is directly blown over the batteries. Passive configuration shown in Figure 3.1b enables both heating and cooling where the ambient air is conditioned by passing through a heat exchanger. For heating of batteries the air would be heated by the heat exchanger before flowing over the batteries, while in cooling model the air would flow through the heat exchanger without heat up. Figure 3.1c shows an active configuration where the air out is fed back into the inlet were it is reconditioned before flowing over the batteries for cooling/heating. It is apparent that the air natural convection for battery dissipation is invalid; heat transfer with air is achieved by directing/blowing the air parallel or serial across the battery module/pack.

For pouch and prismatic shape of the cells there are two ways for the air to flow over the battery, which can be seen in Figure 3.2.

The Toyota Prius supplies conditioned air from the cabin as thermal management for cooling the batteries. Zolot *et al.* [23] used a parallel airflow scheme in a Toyota Prius hybrid electric vehicle, to cool the battery (also used for heating). The forced air system consists of two vents; one for cabin air to return and the other to supply outside air. Lou [74] designed a cinquefoil battery pack constituted by 5 long modules (total voltage of 36 V) to enhance the heat transfer for NiMH batteries. The experiment showed that the temperature drop was fixed to the expectant target,

(a) Passive air cooling

(b) Passive air cooling/heating

(c) Active air cooling/heating
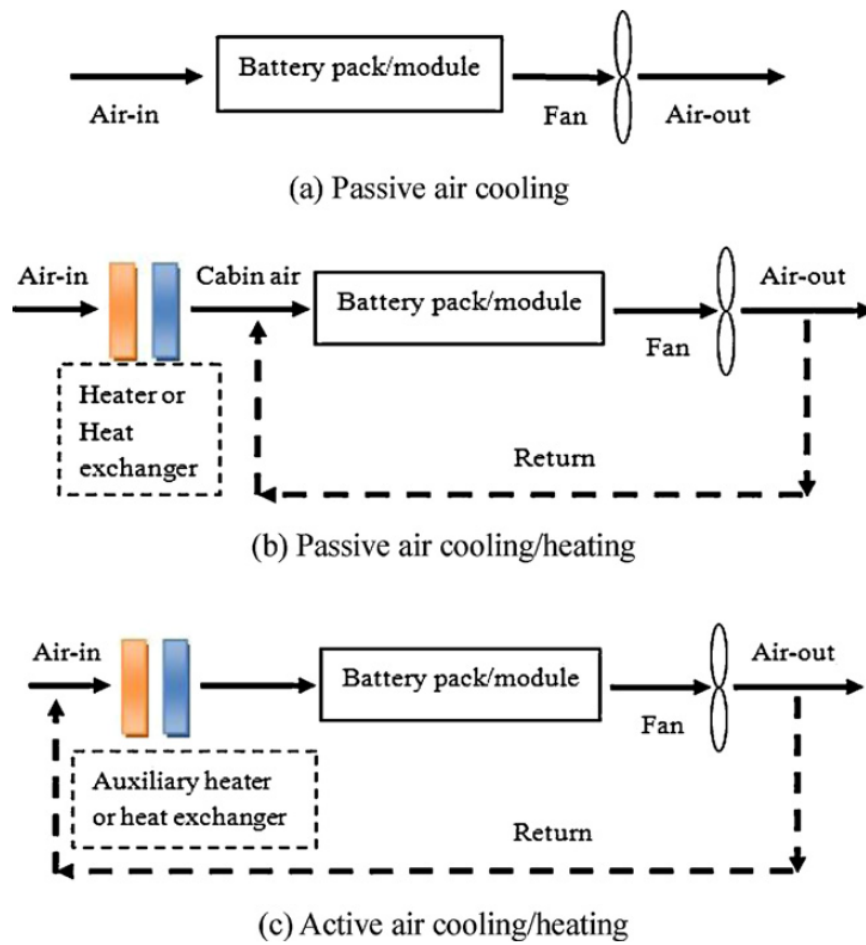
Figure 3.1: Battery thermal management using air.
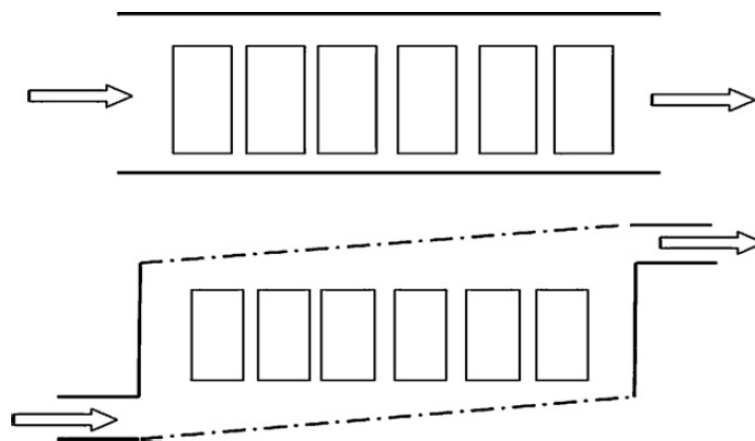
Figure 3.2: Schematic for air flow over a battery pack.

but the temperature difference was still higher by 5°C. In addition the temperature on the battery pack was unevenly distributed.

Air forced convection cooling could mitigate temperature rise in the battery. But the application is limited to moderate heat generation. If in case the battery temperature rises higher than 66°C, it would be difficult to cool it to below 52°C by air-cooling [73]. Furthermore, at stressful and abuse conditions, especially at high discharge rates and at high operating or ambient temperatures (> 40°C), air-cooling will not be proper, and the non-uniform distribution of temperature on the surface of the battery becomes inevitable [75]. Also use of air is difficult for low temperature heat up of battery, then we can consider liquid such as water, which has a higher conductivity than air, for battery thermal management.

3.2.2 Liquid based thermal management

Most of previous studies showed that the heat dissipation could not be significantly alleviated by air natural or forced convection, particularly in large-scale batteries [76]. Figure 3.3 shows some common passive and active configurations of liquid based battery thermal management. Figure 3.3a shows a passive liquid cooling circuit with a coolant pump circulating the coolant between the battery pack and heat exchanger. The battery pack heat is removed by the coolant and transferred to air by the heat exchanger (liquid to air heat exchanger). Figures 3.3b and 3.3c show active liquid cooling configuration respectively. In this configuration the liquid to air heat exchanger would be a part of the engine coolant loop for moderate temperature control and for higher heating and cooling there would be a additional heat exchanger/heater in the primary battery cooling loop.

The battery thermal management system using liquid could be achieved either through discrete tubing around each module; with a jacket around the modules; submerging modules in a dielectric fluid for direct contacts or placing the modules on a liquid heated/cooled plate (heat sink) [77]. The heat transfer medium could be water, glycol, oil, acetone or even refrigerants. The relative strengths of air
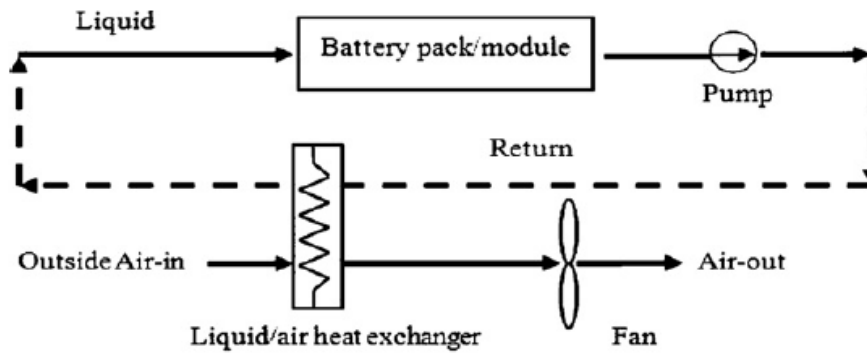
(a) Passive liquid cooling
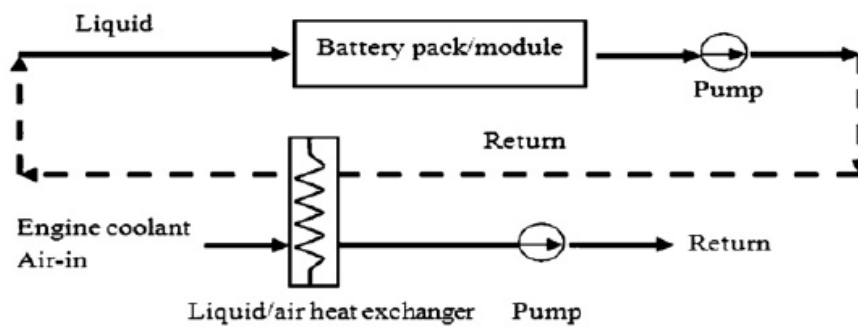
(b) Active moderate cooling/heating
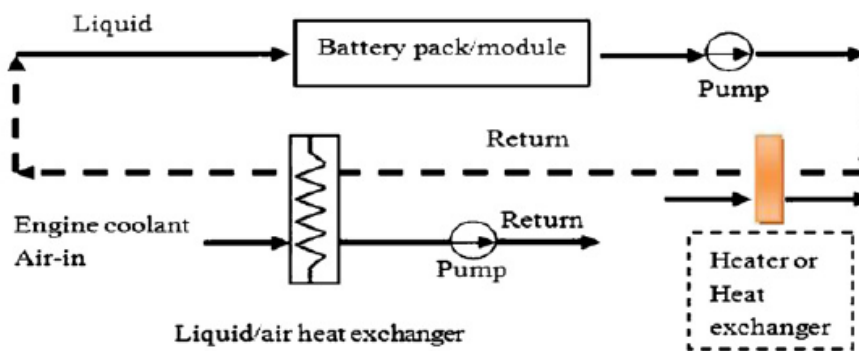
(c) Active cooling (high temperature)/heating (cold temperature)

Figure 3.3: Battery thermal management using water.

cooling and liquid cooling were discussed by Pesaran [78, 77]. With the experiment
results, he suggested that using air as the heat transfer medium is less complicated,
though less effective than a system using liquid cooling/heating. Air cooling could be
adequate for parallel HEVs taking advantage of simple configuration whereas more

effective liquid cooling might be required for EVs and series HEVs [74]. A liquid cooled thermal management system was applied for General Motors Volt plug-in hybrid vehicle [27, 79]. Figure 3.4 shows a liquid cooling thermal management system in a Mercedes hybrid car. Heat pipe, which makes use of change-of-phase
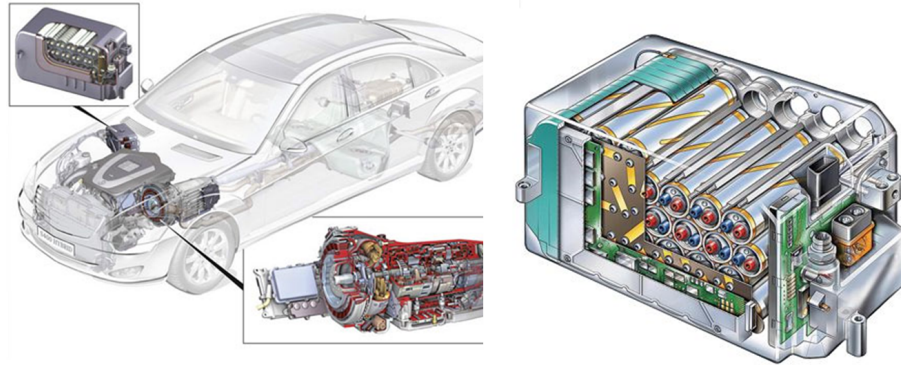
Figure 3.4: Schematic for a water cooling.[1]

heat transfer, first suggested by R.S. Gaugler [80] in 1942, has been taken more attention recent years. It consists of a sealed container whose inner surfaces have a capillary wicking material to provide driving force to return the condensate to the evaporator. Figure 3.5 shows the working of a heat pipe. As the liquid is used
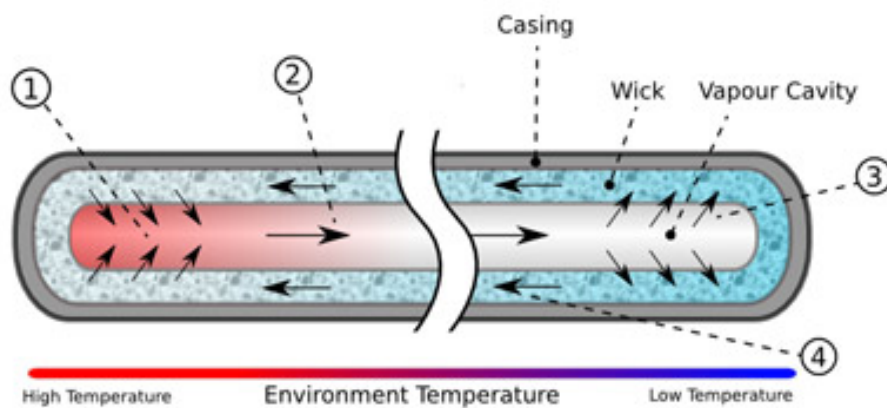
Figure 3.5: Working of a heat pipe.[2]

to complete the phase change process, heat pipe is thought to be liquid for battery

---

[1]http://www.green.autoblog.com/
[2]http://www.ocmodshop.com/heat-pipes-explained/

thermal management. 1) The working fluid in the schematic absorbs the thermal energy and evaporates to vapour. 2) This vapour migrates along cavity to lower temperature end. 3) Vapour condenses back to fluid and is absorbed by the wick, releasing thermal energy. 4) The working fluid flows back to the higher temperature end.

In Wu *et al.* [75], two heat pipes with metallic aluminum fin were attached to the battery (Li-ion, 12 Ah, cylindrical, 40 mm in diameter, 110 mm in length) surface to mitigate the temperature rise. Their experimental and simulation results showed that the heat pipe significantly reduced the temperature rise, especially with the help of metallic aluminum fin. Jang and Rhi [81] adopted a loop thermosyphon (similar to heat pipe) cooling method for high efficiency cooling. The system combined the heat pipe and air cooling; the heating section distributed on the surface of the battery and the fan blew the air flow over the condenser section. Their experiment showed that the operating temperature was under 50°C with pure water as medium and 45°C with acetone.

3.2.3   PCM based thermal management

An ideal thermal management system should be able to maintain the battery pack at an optimum temperature with low volume, weight and cost added. Thermal management systems such as forced air-cooling and liquid-cooling make the overall system too large, complex and expensive in terms of blower, fans, pumps, pipes and other accessories [82]. Therefore, for others thermal management solutions are required. Figure 3.3 shows an example for a cylindrical cell housed inside a PCM base enabling heat transfer to and from PCM directly. A novel solution using PCM for battery thermal energy management was proposed for electric and hybrid electric vehicle applications. PCM battery management system, first demonstrated by Al-Hallaj and Selman [83] and patented [84], performed better than the conventional

thermal management system. Mills and Al-Hallaj [85] designed a PCM thermal management system and simulated for laptop battery pack using the entropy coefficient method. Their results showed that PCM significantly improved the performance of the system and kept the operating temperature lower than 55°C even at the high discharge rate. Figure 3.6 shows the schematic of a generic PCM based thermal management system. Khateeb and Al-Hallaj [86] reported laboratory test results of
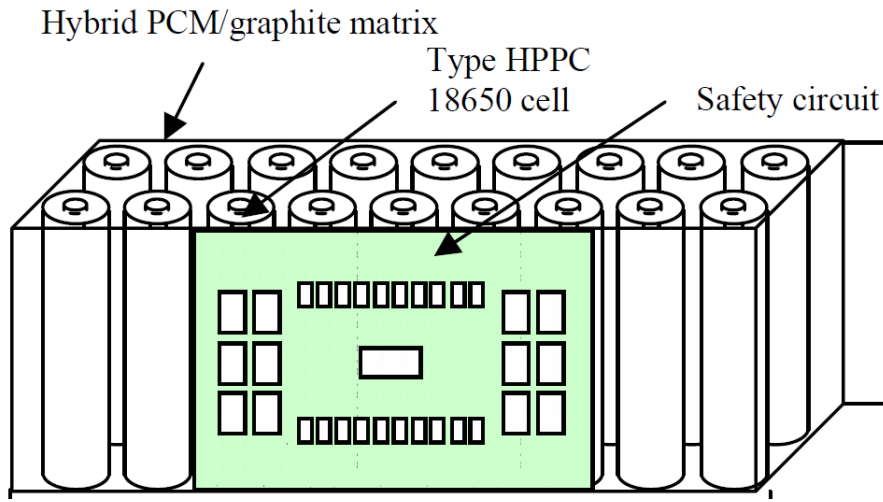
Figure 3.6: Schematic of an PCM based thermal management system.(Source: [3])

a Li-ion battery designed for electric scooter application with four different modes of heat dissipation:

- Natural convection cooling,

- Presence of aluminum foam heat transfer matrix,

- Use of phase change material,

- Combination of aluminum foam and PCM.

Their experiment showed that the method with PCM obtained the best effect. The PCM offers safety in stressed conditions considering the conduction and absorption of heat. Kizilel *et al.* [87] confirmed the validity of using PCM for high-energy

Li-ion packs thermal management system at normal and stressed operating conditions by experiment. Later a compact type 18650-cell module using the PCM thermal management system over active cooling was demonstrated [71]. They indicated the possibility to achieve uniform temperature under normal and stressed conditions if the passive thermal management system is used. Sabbah *et al.* [68] compared the effectiveness of PCM to air forced cooling by numerical simulation and experiment, showed that PCM cooling could keep temperature below 55°C at a constant discharge rate at 6.67C (10 A/cell). For low temperature operation, they
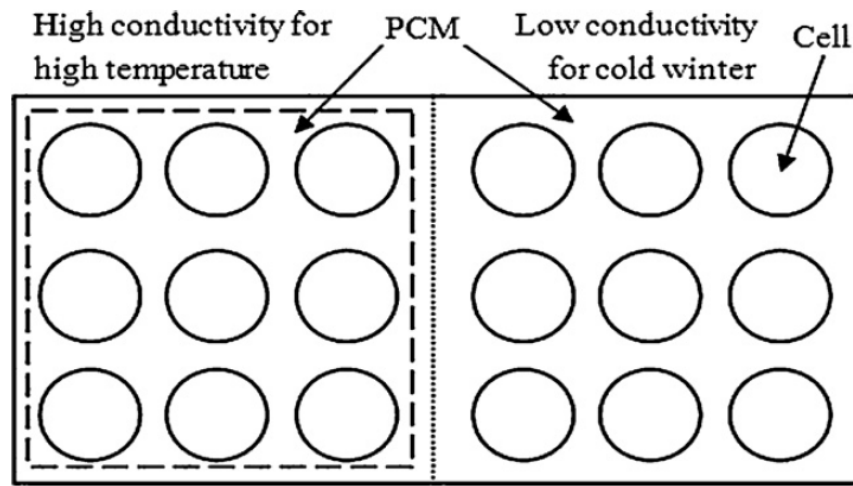
Figure 3.7: Battery thermal management using pcm.(Source: [3])

predicted that PCM is an important advantage for EVs operation under cold conditions or in space applications where the battery temperature drops significantly [83]. Figure 3.7 shows the schematic of PCM based thermal management system for hot as well as cold ambient condition. For cooling application the PCM matrix in which the cells are housed is made of high conductivity material to enable high heat transfer. For a cooler ambient where the priority is heating the matrix consists of low conductivity material. Because of the heat is stored as latent heat, just a smaller part of the heat is transferred to the surroundings. The stored heat will be rejected to the module when the battery temperature is dropping below the melting point of the PCM.

3.2.4   Selection of thermal management

The choice of a heat-transfer medium has a significant impact on the performance
and cost of the battery thermal-management system. The heat-transfer medium
could be air, liquid, a phase-change material, or any combination of these media.
Heat transfer with air is achieved by directing/blowing the air across the modules.
However, heat transfer with liquid could be achieved by using discrete tubing around
each module, using a jacket around the module, submerging modules in a dielectric
fluid for direct contact, or placing the modules on a liquid heated/cooled plate
(heat sink). If the liquid is not in direct contact with modules, such as in tubes
or jackets, the heat-transfer medium could be water/glycol or even refrigerants,
which are common automotive fluids. If modules are submerged in the heat-transfer
liquid, the liquid must be dielectric, such as silicon-based or mineral oils, to avoid
any electrical shorts. Using the air as the heat-transfer medium may be the simplest
approach, but it may not be as effective as heat transfer by liquid. The rate of heat
transfer between the walls of the module and the heat-transfer fluid depends on the
thermal conductivity, viscosity, density, and velocity of the fluid. For the same flow
rate, the heat-transfer rate for most practical direct-contact liquids (such as oil) is
much higher than that with air because of a thinner boundary layer and a higher
fluid thermal conductivity. However, because of oils higher viscosity and associated
higher pumping power, a lower flow rate is usually used, making the heat-transfer
coefficient of oil only three times higher than that of air. Indirect-contact heat-
transfer liquids (such as water or water/glycol solutions) generally have a lower
viscosity and a higher thermal conductivity than most oils, resulting in higher heat-
transfer coefficients. However, because the heat must be conducted through walls
of the jacket/container or fins, the effectiveness of indirect contact decreases.

Because of cost, mass, and space considerations and their use in mild climates,
battery packs in early vehicles particularly EVs did not use heating or cooling

units and depended on the blowing of ambient air for the rejection of heat from
the batteries. Early prototype HEVs also used passive ambient air-cooling. Current
production HEVs (Honda Insight and Toyota Prius) use cabin air for cooling/heating
of the pack. Although the ambient air is heated and cooled by the vehicles air-
conditioning or heating system, it is still considered to be a passive system. For
passive systems, the ambient air must have a mild temperature for the thermal
management to work; otherwise, the performance of the pack can suffer in very cold
or very hot conditions. Outside of these conditions, active components (such as
evaporators, heating cores, engine coolant, or even electric and fuel-fired heaters)
are needed.

3.3   Scope of current work

Management of heat effects associated with lithium-ion batteries remains a chal-
lenge as excessive local temperature rise in Li-ion cells causes reduction of cycle life
and may lead to thermal runaway of individual cells or of an entire battery pack.
Especially in battery packs where the cells are closely packed, in order to exploit
the advantage of Li-ion cells high energy and power density, thermal runaway of a
cell can propagate and cause an entire battery to fail violently. Air based forced
convection cooling is a simple way of mitigating temperature rise in the battery. It
would be difficult to cool and maintain the temperature uniformity within the cells
at higher discharge rates for achieving the safety, performance and cycle life targets.
Similarly, PCM reduce the overall installation costs for thermal management but
are not particularly suitable for all formats of Li-ion cells.

The current work focuses on two key aspects of thermal management by indirect
liquid cooling. The first aspect is being able to predict the heat generated by the
cell at various conditions. A electro-thermal model has been developed, validated

and this has been discussed in Chapter 4. The second aspect is how the heat generated is being removed from the cells. A serpentine channel based cooling plate is used to remove heat through the cells for thermal management. A numerical heat transfer simulation reflecting modest discharge rates (similar to EV application) for a laminar flow regime through serpentine channel is discussed in Chapter 5. For high discharge applications (similar to HEV application), a turbulent heat transfer would be essential. A numerical turbulent heat transfer problem hence is also studied for accessing various turbulence modelling methods, the same is reported in Appendix .

4

Li-ion battery electro-thermal model

4.1   Introduction

Now, the first key aspect of thermal management is discussed *i.e.*, predicting the heat generated by a Li-ion cell. Lithium-ion polymer batteries potentially have much higher energy density ($\sim$ 400 W/L) compared to other battery technologies, and they are already replacing nickel-metal hydride (NiMH) batteries for portable devices such as laptop computers and smart phones, and also for hand-held devices in the power tool industry [88]. The high energy/power density of Li-ion batteries has also made them an attractive power source in electric vehicles and hybrid electric

vehicle , as they can provide longer driving range and higher acceleration. A typical battery pack for the EV application is composed of a large number of cells to provide the required power, and the compactness of battery packs poses a challenge for effective thermal management [88, 44].

The major obstacles to designing a scaled-up of Li-ion batteries for EV applications have been safety, performance and overall cell life. The safety issue concerns the thermal runaway of battery cell, and the prediction and prevention of the propagation of thermal runaway have been studied by many researchers. A Li-ion cell generates heat during both charge and discharge, and the heat generation in the battery can increase sharply leading to overheating under stressful conditions such as high power draw and high ambient temperature while overheating can also be caused by defects in individual cells. If the cells are not thermally managed, the thermal runaway propagates into an entire battery pack [54]. Various battery thermal management systems have been developed for air- and liquid-cooling to prevent the thermal runaway propagation without over-designing the cooling system [71]. The different typres of battery thermal management has been discussed in Chapter 3.

The battery cell temperature also affects the performance, reliability and lifespan. High battery cell temperature can cause a shortening of the lifespan of the Li-ion battery due to increased degradation of the battery cell. It was found that every degree of cell temperature rise reduces the lifespan of the Li-ion battery by approximately two months in an operating temperature range of $30 - 40$ °C [43]. To achieve a full lifespan, the cell temperature difference should be kept below 5°C [62, 63] as large temperature non-uniformity in the battery pack affects adversely overall cell lifespan as well as available cell capacity [64, 52, 53, 34]. Therefore, a battery thermal management system enabling effective temperature control becomes essential for safety, performance, reliability and overall cell life [55, 7, 44]. For bet-

ter design of thermal management system, understanding the real time behaviour of Li-ion cells in vehicle operating conditions is critical, and modelling its thermal behaviour in various EV drive cycles can help to design such battery thermal management systems [88].

4.2   literature review

A larger amount of published work exists regarding single cell battery models. Various numerical models have been developed to predict the thermal behavior of cells, and they can be broadly categorised into three groups: electrochemical model, equivalent circuit model and electro-thermal model.

4.2.1   Electrochemical model

Electrochemical models are built upon the physical makeup of the battery and use diffusion principles and other elements from physics and chemistry [46]. The models characterize the fundamental mechanism of battery power generation. Electrochemical models often contain systems of coupled partial differential equations that can be difficult to simulate/solve and are typically not suitable for control design or models that require evaluation of multiple battery models. Because of the proprietary nature of most readily available batteries, the parameters needed to built the model are often difficult, if not impossible, to obtain.

Many electrochemical models have been proposed to describe battery charge and discharge characteristics with varying complexity [47, 48, 89, 90, 91, 56, 92]. An energy balance is used in conjunction with the electrochemical models to predict the temperature in the battery. The general energy balance for battery systems was proposed by Bernardi *et al.* [93]. Their model incorporates electrochemical reactions,

phase changes, mixing effects, Joule heating, and heat transfer in the global energy balance, assuming that the temperature of the battery is uniform throughout the cell but changes in time. The heat generation term in the energy balance is coupled with an electrochemical model to describe battery charge and discharge characteristics [47, 89, 90, 91, 56, 92]. A fully coupled model [94] uses the latest current and potential information to calculate the heat generation term whereas a partially coupled approach [95] uses heat generation rates from isothermal discharges to estimate heat generation rates during nonisothermal discharge. For simplicity, a decoupled model uses an empirical equations (such as Shepherd equation [50]) to describe the battery charge/discharge curves. While the decoupled model provides simplicity, the fully coupled model produces more accurate cell temperature results.

4.2.2 Equivalent circuit model

A simpler alternative approach to the electrochemical first principle models is the equivalent circuit based models. In such models, the electrochemical elements in the battery are replaced by an electrically equivalent process. For example, charge transfer across a boundary can be represented by parallel resistor and capacitor and ion diffusion can be represented by waves propagating on a transmission line. Therefore, the construction of the equivalent circuit can be obtained via electrochemical impedance spectroscopy (EIS) [96] because different elements in the battery show different behaviors depending on the frequency range. Equivalent circuit models obtained this way show good input to output response when magnitude and frequency range of the input excitation signal are limited [97].

Though simpler than electrochemical models, equivalent circuit models can still be difficult due to the inclusion of distributed elements such as the transmission line or pure frequency domain quantities such as the Warburg impedance [98]. By lumping elements and assuming homogeneity in certain dimensions, an equivalent

circuit model can be simplified. The model represents the cell as a combination of resistors, capacitors and a voltage source. The advantage to this type of model is that the dynamic model equations are all ordinary differential equations. The equivalent circuit can be easily parameterised based on the cell electrochemical impedance spectroscopy (EIS) [96] or the time domain response data from experiments.

4.2.3 Electro-thermal model

Coupled electro-thermal models rely on modelling the polarisation due to mass transport and charge transfer for accurate estimation of the thermal behaviour. A thermal analog of the electrical problem is created to estimate ohmic, polarisation voltage losses and estimate the heat for known electrical behaviour. There have been many previous efforts on the thermal modeling of lithium-polymer batteries for HEV and EV applications [99, 95, 84].

Gu [100] used experimentally determined polarisation expressions, and constructed his model as a network of resistors to predict various properties of a cell including cell voltage, current distribution, power capability, and energy of a Zn/NiOOH cell. A linear and nonlinear polarisations expression that defines the polarisation characteristics of the electrodes was proposed [101]. Bernardi *et al.* [93] proposed a thermal model based on general energy balance for battery systems. Subsequently, this method was used to predict heat generation in prismatic Li-ion cells. Chen and Evans [42, 102, 103] introduced several two-dimensional and three-dimensional thermal models. These models were developed based on the transient heat-transfer equation and the heat generation equation proposed by Bernardi *et al.* [93]. The convective and radiative heat transfers on the surface were considered to be the boundary conditions, and the container of the battery was incorporated into a part of the boundary conditions to facilitate the calculation. Pals and Newman

[99] presented a one-cell model and a cell-stack model [95] to examine the effect of temperature variation on the heat-generation rate and the cell discharge behaviour.

Song and Evans [104] also developed an electrochemical-thermal model,which was coupled with a two-dimensional thermal model and a one-dimensional electro-chemical model, to examine the relationship between thermal and electrochemical behaviour. The heat generation rate in their study was assumed to be from a uniform heat source based on a general energy balance. Further battery thermal modeling work included understanding effects of temperature variation on the heat-generation rate and the cell discharge behavior. Sato [70] summarised that the cell temperature was a result of the combination of heat generated by electrochemical reactions and electrical resistance. Recently, Kim *et al*. [4, 105] used a two-dimensional model to calculate the cell potential and current density distributions during charge and discharge separately using a procedure similar to that reported by Kwon *et al*. [92]. In their study, the thermal behaviour is modeled as a combination of the heat gen-eration due to the electrochemical reactions and electrical resistance within the cell as a function of the electric current and state of charge.

A one-dimensional thermal model assumes that temperature gradient is neg-ligible in the two directions parallel to the current collectors [99, 84]. Such an assumption may be valid for small-scale batteries. However, this may not be jus-tified for large-scale batteries since the temperature distribution becomes less uni-form as the electrode size of a battery increases. Then, a two or three-dimensional thermal model would be desirable for large-scale batteries [106]. Recently, Kim *et al*. [105] developed a two-dimensional model to calculate the potential and current density distribution on the electrodes of a lithium-polymer battery comprising a Li[NiCoMn]O_2 a positive electrode, a graphite negative electrode, and a plasticized electrolyte by following the same procedure of Kwon *et al*. [92]. They adopted a relatively simple modeling approach by considering only Ohms law and charge con-

servation on the electrodes based on the simplified polarization characteristics of the electrodes compared with the papers previously published by other researchers [95, 101, 100]. Two dimensional thermal modeling of the LIPB was carried out based on the modeling results of the potential and current-density distributions using the same procedure described by Kim *et al.* [4].

4.3 Li-ion cell experiments

Before performing detailed electro-thermal charaterisation for numerical model validation purposes, an overall cell performance evaluation were performed on various available cell of different formats and chemistry. Nine Li-ion cell types were used for overall performance evaluation. These comprised four different electrochemical couples in either of two packaging formats (pouch and cylindrical). Continuous power tests, lifecycle tests and temp characterisation tests were done to record the overall cell performance. Capacity, energy and power characteristics were measured and graphs were normalised so that all cells may be directly compared.

4.3.1 Li-ion cell performance evaluation

Table 4.1 shows the details of all the nine cells tested. The cells were measured in relation to their storage capability, to choose the best cells to be used in HEV and EV applications. The tests were based on international standard IEC62660-1:2010 [61]. Figure 4.1 shows a selection of Li-ion cells in different formats. The Cells A,B,C,D and H are cylindrical cells whereas E,F,G and I are pouch cells. Figure 4.2 shows Cell E/ Cell G/ Cell F pouch cells instrumented with T-type thermocouples.

Table 4.1: Description of all the nine cells tested.

Manufacturer	Capacity	Format	Chemistry
Cell A	15 Ah	Cylindrical	Li-ion phosphate
Cell B	8 Ah	Cylindrical	Li-ion phosphate
Cell C	3 Ah	Cylindrical	Li-ion phosphate
Cell D	2.3 Ah	Cylindrical	Li-ion phosphate
Cell E	19.5 Ah	Pouch	Li-ion phosphate
Cell F	40 Ah	Pouch	Li-ion NCM
Cell G	14 Ah	Pouch	Li-ion NCM
Cell H	22 Ah	Clindrical	Li-ion NCA
Cell I	60 Ah	Pouch	Li-ion titanate

Figure 4.1: Collection of cylindrical (Cell A/ Cell H/ Cell D) and pouch Li-ion (Cell G/ Cell I) cells.

Cell performance measurements

All electrical tests were carried out using Bitrode MCV test circuits. These were connected in parallel where tests involved currents greater than 100 A, which is the maximum for a single circuit. Thermal measurements were recorded on a 32 channel temperature data logger at four second intervals, which was the maximum rate for the system. The thermal chamber used for housing the cell has an operating range from −40°C to +80°C with setting accuracy within ±2°C. The thermocouple array accuracy was within ±0.15°C with standard error of 0.02°C. The voltage accuracy is calibrated with 0.1 of full scale reading (5 V) and current accuracy is calibrated within 0.1 of full scale (100 A).
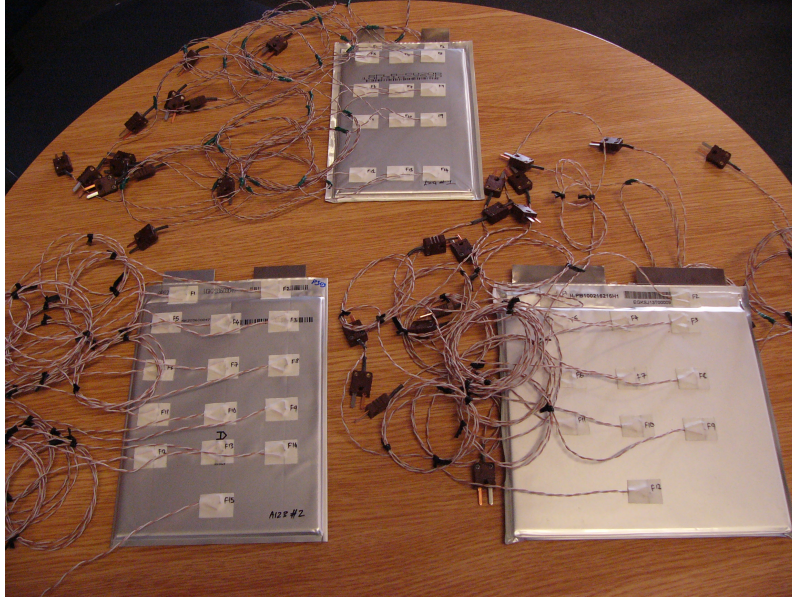
Figure 4.2: Thermocoupled Li-ion pouch cells (Cell E/ Cell G/ Cell F).

Figure 4.3 and 4.4 shows the battery environment chamber (Weiss Gallenkamp Votsch VC3 4060) and the high temperature storage equipment (Weiss Gallenkamp Votsch VT3050) used for the current tests respectively. The multi-channel temperature measurement system is shown in Figure 4.5.

Figure 4.3: Environment chamber: Weiss Gallenkamp Votsch.

Table 4.2 compares the nine cells selected based on the overall cell performance experiments. Three cells from same batch of each manufacturer were selected for the tests to reduce manufacturing variations. The cell format and chemistry are

Figure 4.4: High temperature battery storage chamber: Weiss Gallenkamp Votsch.
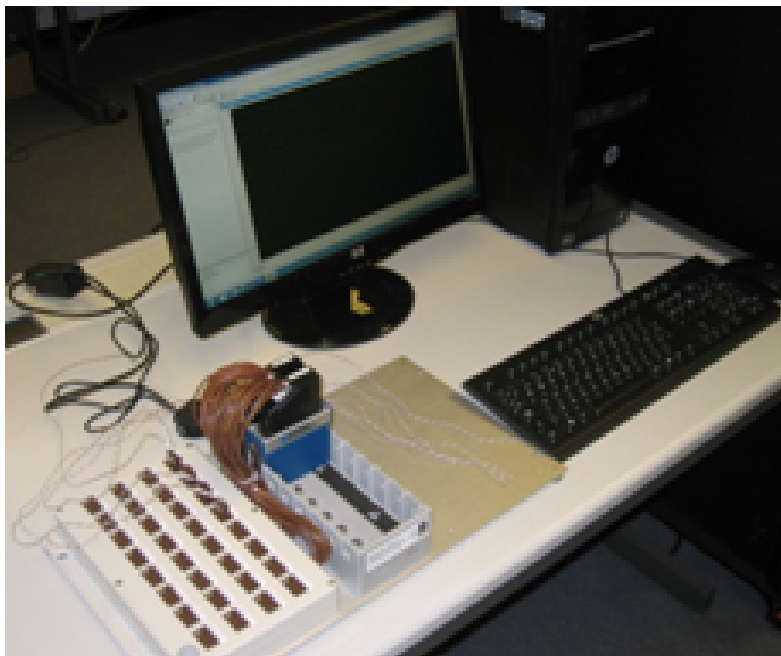
Figure 4.5: Thermal data logger.

highlighted in the table for each cell manufacturer. The electrical storage capacity of the nine cell types ranged from 2.3 Ah up to 60 Ah and so it was necessary to convert fundamental performance data to standardized units, for example Wh/kg, to enable ranking the cell types.

The cells were tested for parameters like electrical performance, reliability and assembly effects. Various key factors for each of the parameters were identified for evaluating them. These factors are listed in the Table 4.2 below each of the individual parameters. Within electrical performance, the power and energy density per unit weight or volume are the significant contributors to range and acceleration in vehicle applications. For example, power density has higher significance for HEV and energy density for EV systems. Capacity, nominal voltage and internal resistance are also critical factors forming a key part of the cell electrical performance.

The other key parameter is reliability. Reliability features are difficult to quantify given the small sample sizes and probability of selection in the tests. Very low range values for mass and internal resistance has been taken as indicators of good manufacturing control. The third key parameter is connectivity. The connectivity features have not been included in the overall evaluation as the advantage level depends on the level of manufacturing sophistication available. They have been listed in the Table 4.2 for reference only. The threaded terminal examples are easy to build into modules with minimal tooling. The bolts and additional connector bars, however, add weight and electrical resistance to the system. The construction of the Cell E pack is an example of a more complex seam welding technology, which adds no weight and provides a minimal conductance path with robust structure. For large scale production, the tab weld approach would seem to be advantageous. For each comparative parameter the three cell types with best performance have been highlighted. No attempt has been made to provide a formal weighting of importance to the different parameters. An overall ranking has been identified by summing the

Cell manufacture/supplier	Cell A	Cell B	Cell C	Cell D	Cell E	Cell F	Cell G	Cell H	Cell I
Chemistry	Graphite-FePO	Graphite-FePO	Graphite-FePO	Graphite-FePO	Graphite-FePO	Graphite-NCMO	Graphite-NCMO	Graphite-NO	TiO-NCMO
Construction	Cylindrical	Cylindrical	Cylindrical	Cylindrical	Pouch	Pouch	Pouch	Cylindrical	Pouch
Mass (g)	461	330	85	71	3557 (495)	988	430	668	1850
Volume(litre)	0.21	0.15	0.034	0.034	3.16 (0.263)	0.427	0.227	0.318	0.831
Electrical performance									
Specific Power (W/kg) 10sec pulse	1577	1684	763	2535	484 (3480)	3229	1983	2085	1788
Specific energy (Wh/kg) C_1rate	101	74	106	102	17.6 (126.5)	150	169	120.73	75.7
Energy density (Wh/l) C_1rate	222	160.6	266	215	19.71 (237)	352	315	253.69	168.5
Capacity (Ah) C_1rate 25°C	15.1	8.06	3.03	2.3	19.79	38.87	20.06	22.89	64.7
Capacity (Ah) C_3rate 25°C	16.3	8.3	3.09	2.3	20.68	40.47	21.84	24.02	66.5
Nominal voltage (V)	3.2	3.2	3.3	3.3	3.3	3.7	3.7	3.6	2.25
Internal resistance (mΩ) 1kHz AC	2.17	2.35	25.04	9.4	0.9	0.5	1.3	0.98	0.32
Internal resistance (mΩ) 10 sec DC	3.6	4.6	41.1	14	1.6	1	3.3	2.2	0.4
relative conductance (S/Ah) 1kHz AC	28	51	13	46	54	49	35	42	47
relative conductance (S/Ah) 10 sec DC	17	26	8	31	30	25	14	19	38
Temperature effect on capacity (% @C1)	10	23	28	2	8	19	22	14	23
Reliability									
mass range %	1.30	1.82	3.52	1.40	0.84	0.20	0.00	1.05	0.32
IR range %	8.15	2.12	12.18	9.54	3.56	5.39	1.07	8.16	14.49
capacity range %	2.58	1.99	3.30	0.44	1.01	0.31	0.20	2.23	0.74
Assembly effects									
Cell connection type	Threaded	Threaded	none	none	Tab	Tab	Tab	Threaded	Tab
Cell connector surface area	200	200	113	113	352	1200	600	95	2240
Connection current density (A/mm²) @ peak power	1.82	1.39	0.29	0.80	3.06	0.99	0.47	8.78	0.98
Verdict (Points Based)	1	2	1	4	6	6	5	0	2

Table 4.2: Comparison between nine Li-ion cells.

number of performance leaders for each cell type.

Figures 4.6 and 4.7 show the energy density, specific energy for all the nine cells
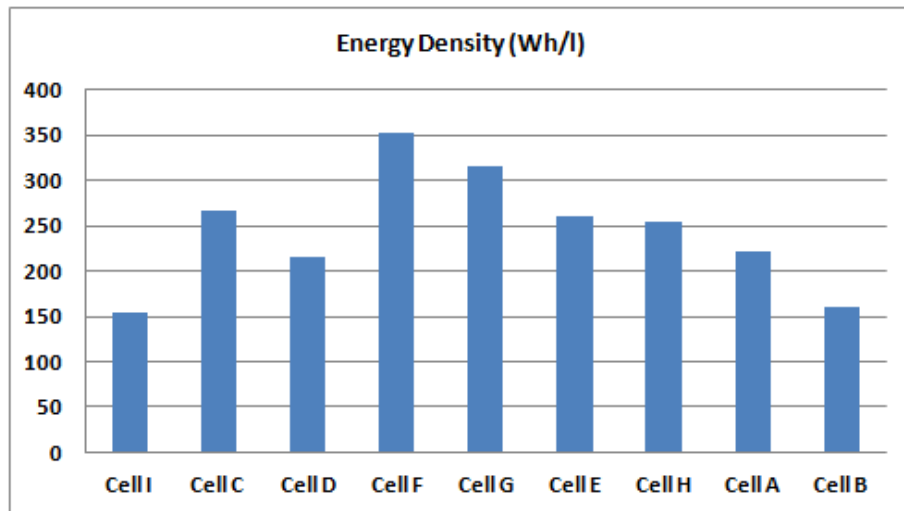
Figure 4.6: Energy density comparision
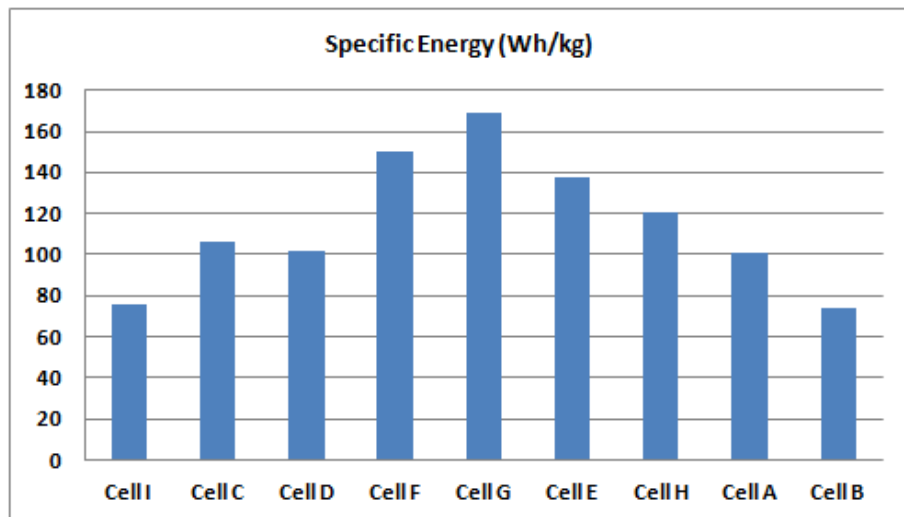
Figure 4.7: Specific energy comparision.

tested. Similarly the Figures 4.8 shows specific power. The data for energy density, specific energy and specific power has been normalised in Figure 4.8. The normalised data enables direct comparison between all the nine cells. The Cell E and Cell F cells perform well in all of the measured parameters. This can be seen clearly on the normalized graph.

Figures 4.10, 4.11, and 4.12 compare the published capacity (Ah) with the actual tested capacity at various temperatures. It can be seen that there is variation
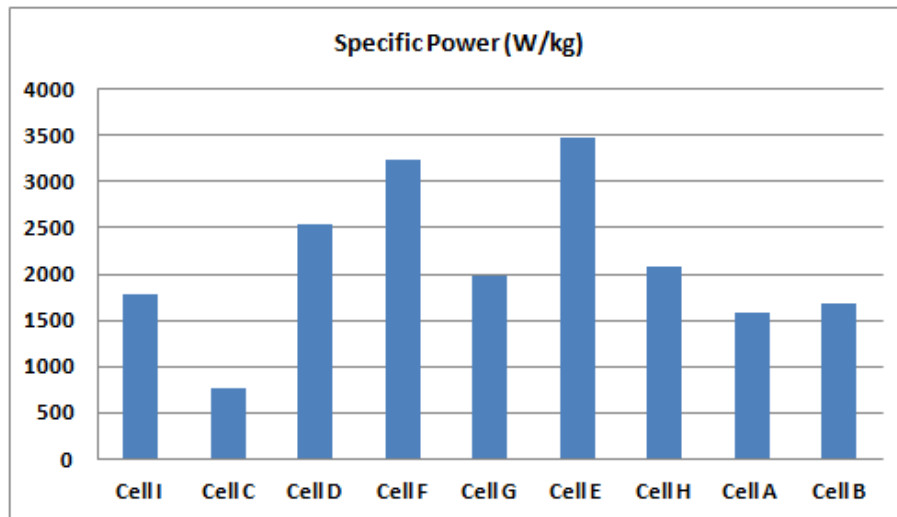
Figure 4.8: Specific power comparision.
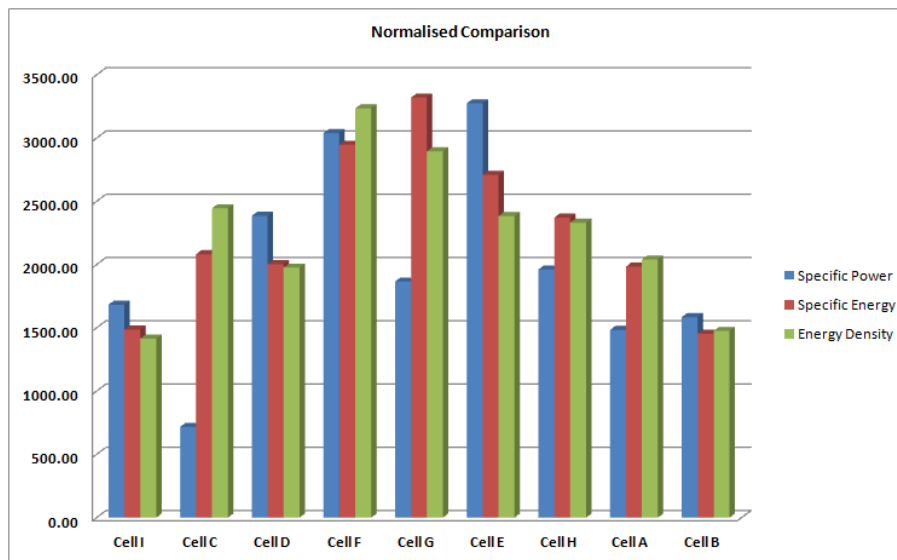
Figure 4.9: Normalized data.

between the claimed capacity by the manufacturers and the actual tested capacity. The capacities are taken as an average of all the cells tested at a known C rate and temperature. This data shows the degree of variability in production for a given sample.

The tests were conducted at different ambient temperatures. At 0°C, Cell D, E and H demonstrate less de-rating. The worst performing cells are the Cell C samples,
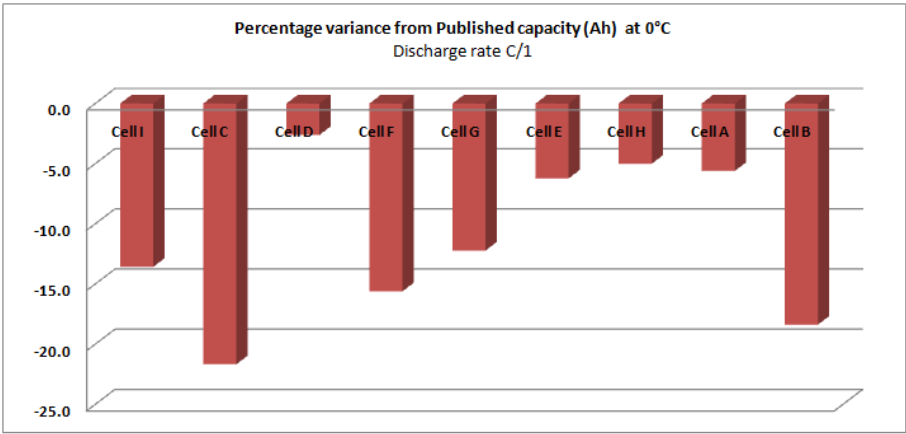
Figure 4.10: Capacity variation at 0°C.
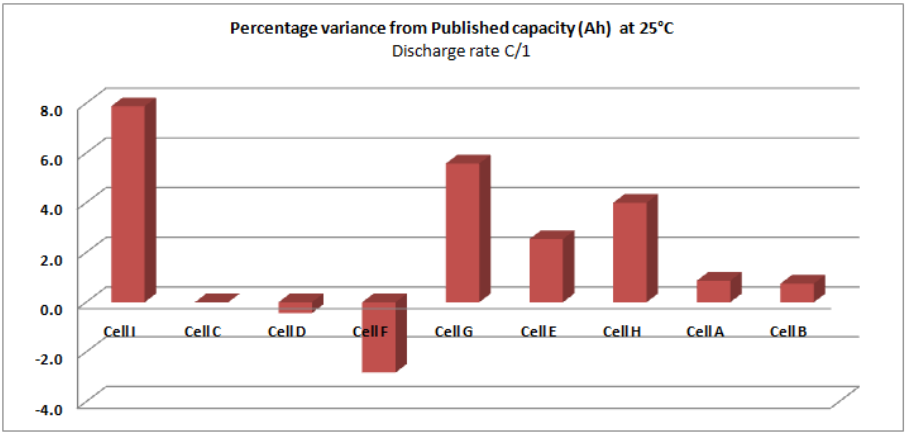
Figure 4.11: Capacity variation at 25°C.
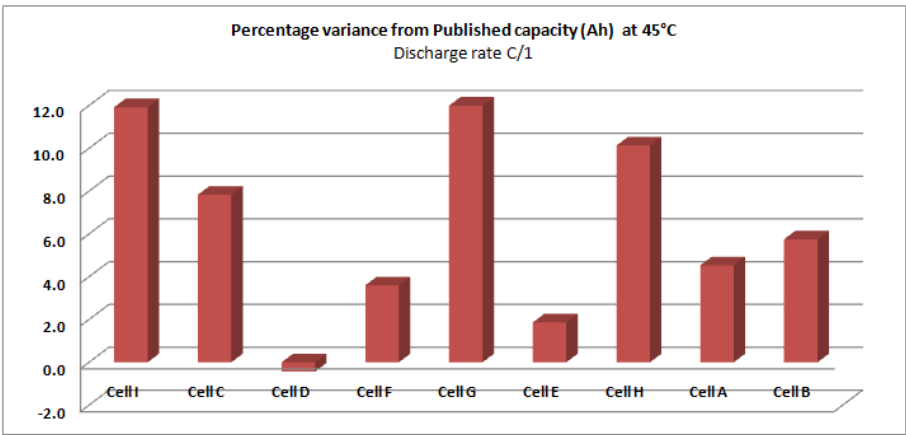
Figure 4.12: Capacity variation at 45°C.

although the Cell B samples are also poor in this area. In terms of variation between samples at 0°C, Cell I, Cell E and Cell H perform very well. The worst overall performance here is from the Cell C cells. At 25°C, the tested capacity exceeds the published capacity in majority of the cases with Cell F being an exception. The Cell C and Cell D demonstrate an actual capacity which is very close to the capacity as published in data sheets. The Cell I and Cell F also give good results when comparing variance in capacity between cells in the test batch, with the Cell F cells showing the closest match. At 45°C, the variance in capacity shows the maximum deviation from the test average for all the cells tested. Cell E demonstrate less de-rating at 45°C. The worst performing cells are the Cell I, Cell G, and Cell H samples. Looking at variation between samples at 45°C, Cell C, Cell D and Cell F cells perform very well. The worst overall performance here is again from the Cell B.

Cell performance based overall ranking

Based on the analysis in Table 4.2, there is a clear dominance for the pouch cell designs. This is unlikely to be over-turned by further weight addition, required for pack assembly, compared to cylindrical cells. Further differentiation can be seen for HEV and EV applications based on power density and energy density properties. The Cell E cell has the advantage for power, making it most suitable HEV, while the Cell F product would be preferable for EV applications. Other properties of the different chemistries of these two products reenforce the choice along this line. Iron phosphate cells such as the Cell E have better thermal and electrical stability. The HEV application will have greater temperature variation given the higher power operation. The flat voltage profile around the central section of the state of charge range will give more predictable relationship between power and current output during operation. Metal oxide cells have higher energy density for increased range.

The Cell F and Cell G products have similar performances but the larger capacity of the former makes it more favourable for EV requirements. For numerical electro-thermal modeling and detailed cell charaterisation testing Cell G cell is selected.

4.3.2 Li-ion cell characterization

In this study, a high energy density Li-ion polymer pouch cell was tested to assess the electro-thermal cell model. The Li-ion cell has a graphite anode and a Li[NiMnCo]O_2 cathode with a nominal capacity of 20 Ah. The schematic of the experimental setup is shown in Figure 4.13. A climatic chamber was used to provide controlled thermal conditions during the test (Figure 4.13a). A box was installed around the cells to ensure well-defined free convective cooling and to protect the cells from forced convection, which would adversely affect the results. Figure 4.13b shows the Li-ion cells inside the box. The cell was prepared with 10 thermocouples to measure the temperature evolution on the cell surface during the test run. The locations of the thermocouples are shown in Figure 4.13c.

Electro-thermal test cycle

A Li-ion cell was tested using one of the Tata Motors European Technical Centre (TMETC) cell testing program within operating limits of the cell. The test cycle consisted of several constant current charge and discharge. Temperature was kept constant during the measurement at a reference temperature (T_{ref}). The electrical and thermal measurements at different reference temperatures and discharge rates were recorded. The cell was discharged at a constant discharge rate until the lower cut-off limit of 3 V was reached. Each discharge rate measurement required initialisation steps to precondition the cell before the measurement. These steps were to ensure that the prescribed electrical and thermal initial condition for each
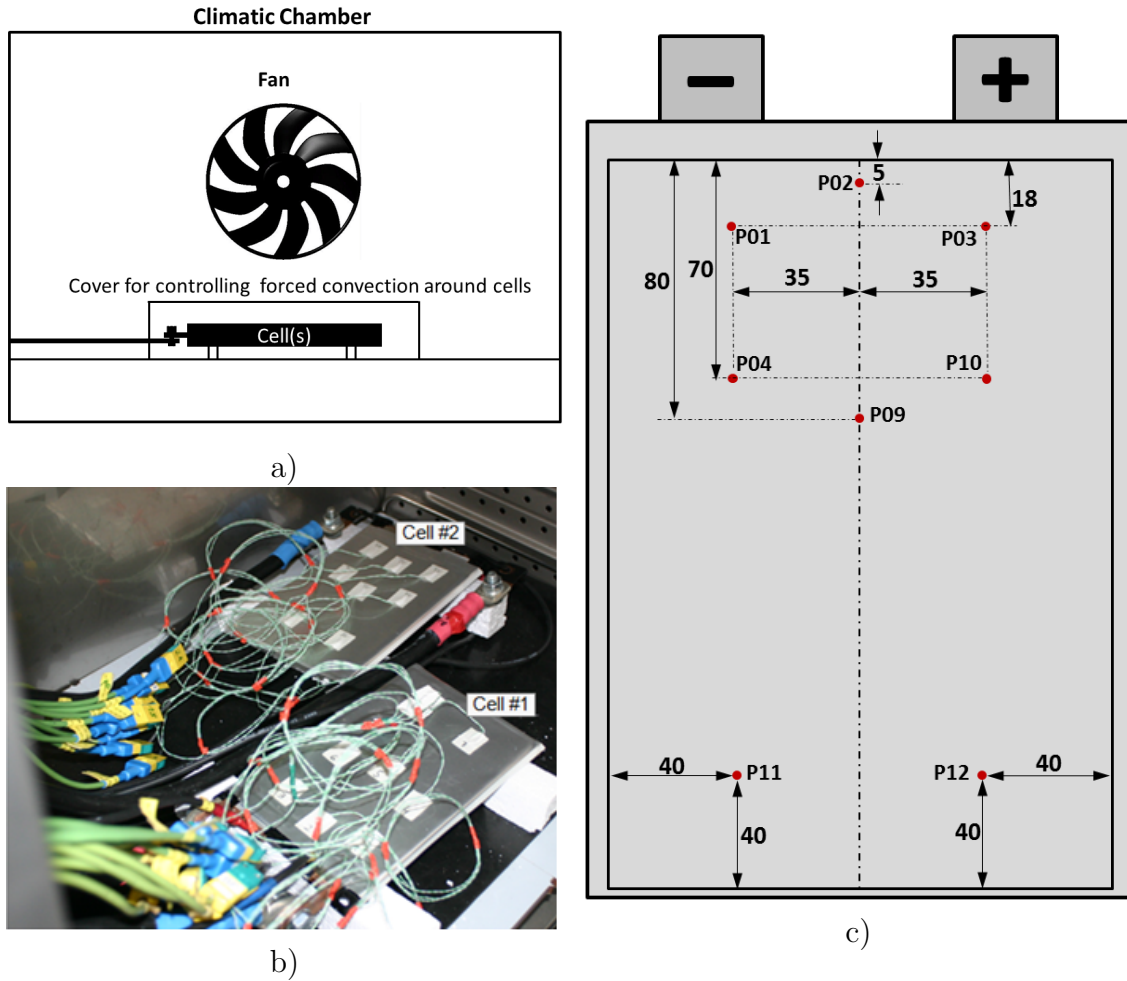
Figure 4.13: a) Schematic of Li-ion cell test setup, b) instrumented cell in climatic chamber, and c) location of thermocouples in mm.

measurement was achieved. Table 4.3 shows the procedure for initialisation and measurement requirements in detail.

Figure 4.14 shows the electric loading cycle used in this study. The section AB corresponds to a discharge current of 5C. The constant current discharge was followed by a 10 minutes break with no electric load. The remaining initialisation step before the next constant discharge consists of a 1C constant current charge (section EF) and a constant voltage section (section FG) where the current gradually reduces below 1 A. A 40 minutes break is then given for the relaxation processes in the cell chemistry before the next discharge rate measurement. This process of initialisation was performed between the discharge measurements: sections HI, MN

Table 4.3: Cell test procedure. T_{test} is the test temperature.

Initialization step

Temperature (°C)	Procedure	Value	Limit criteria
25	discharge	1C	$U_{min} \leq 3.0V$
25	break		10 minutes
25	charge	1C	$U_{max} \geq 4.1V$
			$I_{min} \leq 1A$

Measurement step

T_{test}	break		≥ 40 minutes
			$T_{cell} = T_{test}$
T_{test}	discharge	various C rates	$U_{min} \leq 3.0V$
25	break		30 minutes
25	charge	1C	$U_{max} \geq 4.1V$
			$I_{min} \leq 1A$

and RS correspond to 0.5C, 1C, and 3C constant current discharge measurements, respectively. This whole process is repeated for different reference temperatures (T_{ref}), ranging from -10°C to 45°C. The cell temperature and voltage during charge and discharge in the entire test cycle were recorded and compared with the electro-thermal model prediction in Section 4.4.1.
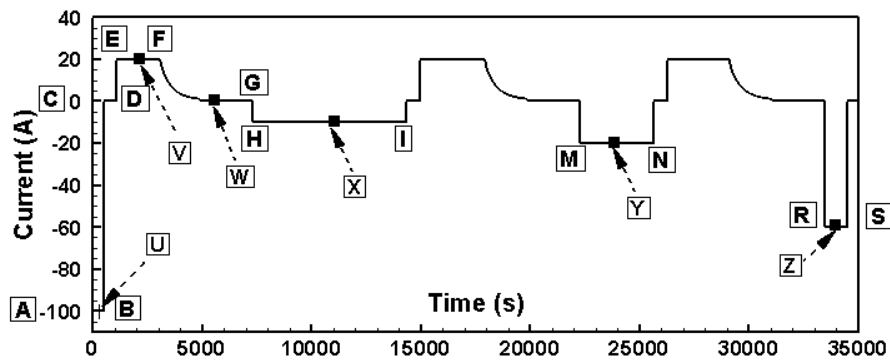
Figure 4.14: Charge/discharge test cycle.

4.4   Coupled three dimensional electro-thermal model

Most of the previous studies have modelled the Li-ion cell thermal behaviour sep-
arately for charge or discharge, and have not considered the combined effect of
them, typically present in vehicle load conditions [105]. Accurate modelling of the
electro-thermal behaviour of Li-ion cells for dynamic electric loading conditions is
a key requirement to improve battery thermal management system. In this study,
a three-dimensional, fully-coupled electro-thermal cell model, which is capable of
modelling vehicle load conditions, is developed. A high energy density Li-ion poly-
mer pouch cell was tested at various charge and discharge rates in Section 4.3.2 to
provide model characterisation data and also other relevant electrical and thermal
data for validation. The current work focuses on electro-thermal modelling and its
use in battery thermal management studies for EV applications. This model al-
lows for scalability with accuracy and reasonable simulation time which is of prime
importance while modelling full vehicle battery models.

Electro-thermal modeling is an effective way to understand how the design and
operating variables affect the thermal behavior of the lithium-ion battery during
charging and discharging. This method requires the cells to be characterised. Once
characterized, this model is capable of predicting the electro-thermal behavior for a
range of charge and discharge cycles. The current work focuses on electro-thermal
modeling and its use in battery thermal management studies for EV applications.
This is based on the fact that such models allows for scalability with reasonable
accuracy and simulation time which is of prime importance while modeling full
vehicle battery models.

In order to obtain a precise simulation of the thermal behavior of a battery the
internal geometry details and its properties should be estimated as accurately as
possible in the model. It may be impractical to describe completely the compli-

cated behavior of a lithium battery with existing theoretical expressions. Besides, an unacceptable amount of calculation time could be required if the model is too complicated. Thus, it is common to adopt some simplified strategies such as neglecting the radiative heat transfer on the boundaries, taking the layered-structure of the cells as the homogeneous materials, transferring the container to be a part of the boundary equations, and degrading a three-dimensional system to a two-dimensional model. It should be recognized that proper assumptions greatly enhance the value of the thermal model, whereas any improper assumption can lead to inaccurate or incorrect simulation results. It is important to ascertain the critical factors which significantly affect the thermal behavior and also the minor elements which can be neglected in the thermal model. Hence, in the present work, a detailed thermal model has been developed to verify the assumptions and also to determine the optimal approach to simplify the thermal model.

4.4.1   Coupled electro-thermal model

The Li-ion cell used in this study is comprised of a pouch case, electrode plates, electrolyte, and separators. To model the thermal behavior of a battery cell accurately, the configuration, geometry, physical, chemical and electrochemical properties need to be known. In our electro-thermal model, the cell is characterised by a structure formed with a homogeneous layer, representing the anode, cathode and separator. The local heat generation in the battery cell due to the electrochemical reactions and the mass transfer of ions in the electrolyte are characterised by local internal resistance and the current densities. The performance of a cell is influenced by the charge/discharge rate, the ohmic resistance, the activation polarisation or charge transfer at the electrodes, the concentration polarisation in the electrolyte near the electrodes, and the cell temperature.

In this study, a simple three-dimensional mathematical model is used to predict

the electrical and thermal performance of the Li-ion cell. The potential and current density distribution on the electrodes are calculated using a PDE method proposed by Kwon *et al.* [92]. The charge conservation on the electrodes are modelled using a simplified polarisation characteristics of the electrodes, and Poisson equations for the potentials of the positive and negative electrodes are derived in conjunction with Ohm's law. A modified form of the polarisation expression proposed by Newman and Tiedemann [107] is used in this study. An additional temperature dependency term is included in the polarisation expression to account for the Seebeck effect. The cell terminal voltage (V_{cell}) can be written as a function of depth of discharge (DOD), electric current and temperature [92]:

$$V_{cell}|_{T_i,J,\text{DOD}} = \frac{J}{Y} + U + b(T_i - T_{ref}), \tag{4.1}$$

where Y is the conductance, and U is the equilibrium voltage (open circuit voltage). The first term on the right hand side is the Ohm's law term, and the current density is defined as $J = I/A$, where I is the current normal to the active material, and A is the active material area. The last term accounts for the Seebeck effect, where T_i is the cell temperature, and T_{ref} is the ambient temperature. The Seebeck coefficient b is to be determined from the test data.

A schematic diagram of the current flow in the cell during discharge is illustrated in Figure 4.15. The distance between the electrodes is assumed to be so small that the current flow between the electrodes is perpendicular to the electrodes. The modeling procedure to calculate the potential and current density distribution on the electrodes is the same used by Kwon *et al.* [92].

From the continuity of current on the electrodes,

$$\nabla \overrightarrow{i_p} - J = 0 \text{ in } \Omega_p, \tag{4.2}$$
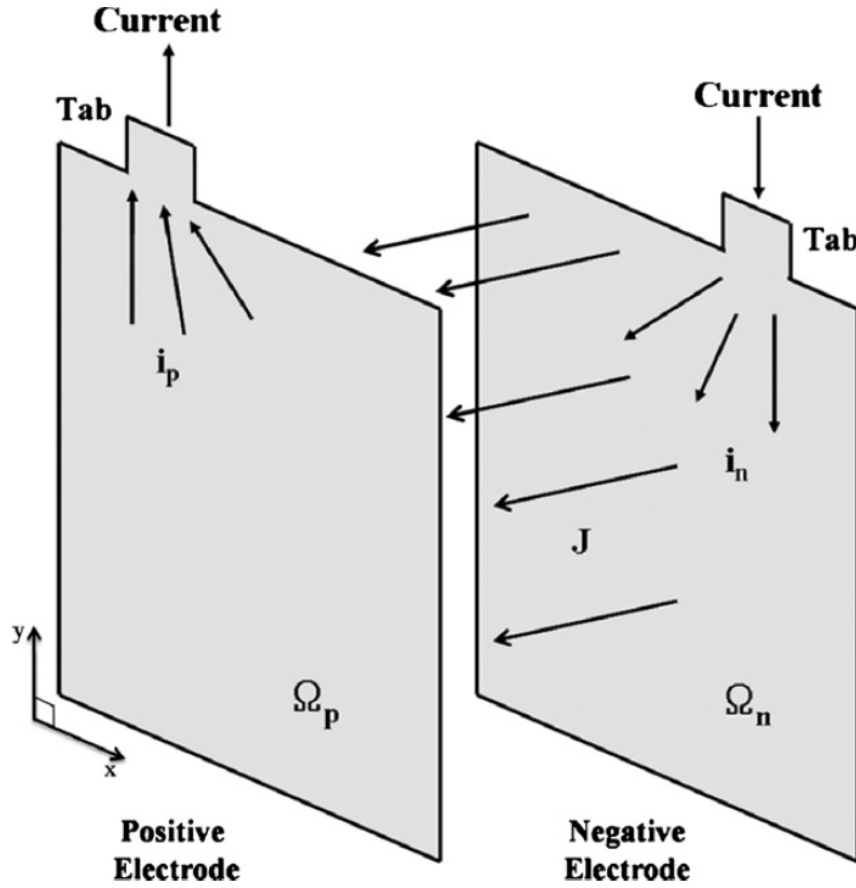
Figure 4.15: Schematic diagram of the current flow in the parallel plate electrodes of a li-ion cell.(Source: [4])

$$\nabla \overrightarrow{i_n} + J = 0 \text{ in } \Omega_n, \tag{4.3}$$

the where $\overrightarrow{i_p}$ and $\overrightarrow{i_n}$ are the linear current density vectors (current per unit length Am^{-1}) in the positive and negative electrodes, respectively, and J is the current density (current per unit area (Am^{-2}) transferred through the separator from the negative electrode to the positive electrode. Ω_p and Ω_n denote the domains of the positive and negative electrodes, respectively.

By Ohms law, eqn $\overrightarrow{i_p}$ and $\overrightarrow{i_n}$ can be written as

$$\overrightarrow{i_p} = -\frac{1}{r_p} \nabla V_p \text{ in } \Omega_p, \tag{4.4}$$

Table 4.4: Parameters used for the calculation of electrode resistances.

Parameter	Li_xC_6	$Li[NiCoMn]O_2$
$s_e(Sm^{-1})$	1.0	0.139
$h_e(\mu)$	145	150
$s_c(Sm^{-1})$	6.33×10^5	3.83×10^5
$h_c(\mu)$	10	20

$$\overrightarrow{i_n} = -\frac{1}{r_n}\nabla V_n \text{ in } \Omega_n, \tag{4.5}$$

where r_p and r_n are the resistances (Ω) of the positive and negative electrodes, respectively, and V_p and V_n are the voltage at positive and negative electrodes, respectively. By substituting Equations 4.2 and 4.3 into Equations 4.4 and 4.5 the following Poisson equations for V_p and V_n are obtained

$$\nabla^2 V_p = -r_p J \text{ in } \Omega_p \tag{4.6}$$

$$\nabla^2 V_n = -r_n J \text{ in } \Omega_n \tag{4.7}$$

The relevant boundary conditions for V_p and V_n are given in Kim *et al.* [92]. The resistance, r (r_p or r_n), are calculated as follows:

$$r = \frac{1}{h_c S_c + h_e S_e} \tag{4.8}$$

where h_c and h_e are the thicknesses (m) of the current collector and the electrode material, respectively, and S_c and S_e are the electrical conductivities (Sm^{-1}) of the current collector and the electrode material, respectively.

The parameters used in the calculations of resistances for the electrodes are listed in Table 4.4 [92].

The local heat generation rate of the Li-ion cell is then estimated during charge/discharge cycle based on the various losses in the cell [108]. The heat generation equation developed by Bernardi *et al.* [93] is used in this study:

$$Q = I \left(U - V_{cell} - T_i \frac{dU}{dT} \right),$$ (4.9)

where $I(U - V_{cell})$ estimates irreversible heat component due to deviation of cell voltage from the equilibrium voltage, and $I(T_i \frac{dU}{dT})$ accounts for the reversible heat generation due to entropy change. $\frac{dU}{dT}$ expresses the temperature dependence of the equilibrium voltage. The heat generation due to the ohmic resistance in the cell is also considered in the study [109].

In order to model the thermal behaviour of the Li-ion cell, the electrical model is combined with an energy balance. The unsteady three-dimensional heat conduction equation can be written as [110, 94, 106]:

$$\rho c_p \frac{\partial T}{\partial t} = \frac{\partial}{\partial x} \left(k_x \frac{\partial T}{\partial x} \right) + \frac{\partial}{\partial y} \left(k_y \frac{\partial T}{\partial y} \right) + \frac{\partial}{\partial z} \left(k_z \frac{\partial T}{\partial z} \right) + Q - Q_c,$$ (4.10)

where Q the heat generation in the Li-ion cell (Equation 4.9).

At the boundary, a convection thermal boundary condition is applied [93] to estimate Q_c, the heat transfer rate with the environment through the battery surface.

$$Q_c = h_t(T - T_{ref}),$$ (4.11)

where $h_t = 25$ W/(m²K) is the convective heat transfer coefficient. The reference temperature is set to be $T_{ref} = 25°C$ to reflect the climatic chamber test temperature.

Equations 4.9 and 4.10 can predict the electro-thermal behaviour at every point in the Li-ion cell. The heat release from the cell, and subsequent the cell temperature

Table 4.5: Material properties used in the model. k_e is electrical conductivity.

	ρ [kg/m^3]	k [W/mk]	k_e [S/mm]	c_p [J/kgK]
Pouch	1.15	0.16	0.1	1900
Positive Terminal	2.7	238	38300	900
Negative Terminal	8.36	398	63300	385

are solved in both space and time. A three-dimensional finite-volume method is used to solve the electro-thermal model, and the cell volume is discretised as a cartesian mesh in all three directions. In the finite volume model, the electrodes, separators and electrolyte are modelled at a macro level, and the volume-averaged material properties of all the cell components are used [106]. The enveloping pouch is also considered to model a realistic heat transfer to the environment. The material properties of the pouch and the tab used in the simulation are listed in Table 4.5. The density, thermal conductivity and heat capacity of the cell components are assumed to be uniform throughout the battery and to remain constant within a known range of temperature.

Y and U in Equations 4.1 and 4.9 are dependent on the depth-of-discharge of the cell. Y and U values are estimated at various DOD using measurement data of cell voltage versus current density, where Y is the inverse of the slope, and U is the intercept. Then, their DOD dependency is modelled following Gu [100]. The conductance is given by:

$$Y(\text{DOD}) = \sum_k j_k(\text{DOD})^k \exp\left[\frac{E_{act}}{R}\left(\frac{1}{T_{ref}} - \frac{1}{T_i}\right)\right], \tag{4.12}$$

where R is the universal gas constant (8.314 J/(mol·K)). Arrhenius expression [111] is used to consider the temperature dependence of the electrochemical model property. The activation energy, E_{act}, is to be estimated from the test data. Similarly,

the equilibrium voltage is given by

$$U(\text{DOD}) = \sum_l b_l(\text{DOD})^l, \tag{4.13}$$

where j_k and m_l are the fitting coefficients for Y and U, respectively. In this study, all fitting coefficients could represent up to 8th-order polynomials, and these coefficients are determined from discharge test data for various temperatures and C rates. Similarly, $\frac{dU}{dT}$ in Equation 4.9 is also characterised with 8th-order polynomials.

Now, the values for b and E_{act} can be determined using discharge test data. From Equations 4.1, 4.12 and 4.13 we have

$$Y(\text{DOD}, T_i) = \sum_k J_{k,i}(\text{DOD})^k = \sum_k a_k(\text{DOD})^k \exp\left[\frac{E_{act}}{R}\left(\frac{1}{T_{ref}} - \frac{1}{T_i}\right)\right] \tag{4.14}$$

$$U(\text{DOD}) + m(T_i - T_{ref}) = \sum_l M_{l,i}(\text{DOD})^l = \sum_l m_l(\text{DOD})^l + m(T_i - T_{ref}), \tag{4.15}$$

where $J_{k,i}$ and $M_{l,i}$ are fitting coefficients for a given temperature T_i. From Equations 4.14 and 4.15, E_{act} and m can be deduced

$$\ln\left(\frac{\sum_k J_{k,i}(\text{DOD})^k}{\sum_k j_k(\text{DOD})^k}\right) = E_{act}\left[\frac{1}{R}\left(\frac{1}{T_{ref}} - \frac{1}{T_i}\right)\right], \tag{4.16}$$

where E_a is the slope of the linear fitting of $\ln\left(\frac{\sum_k J_{k,i}(\text{DOD})^k}{\sum_k j_k(\text{DOD})^k}\right)$ with respect to $\frac{1}{R}\left(\frac{1}{T_{ref}} - \frac{1}{T_i}\right)$, and b is the slope of the linear fitting of $(M_0 - m_0)$ to $(T_i - T_{ref})$. Test data at various temperatures, charge and discharge rates are used for cell parameter characterisation.

4.5   Results and discussion

In this Section electro-thermal model validation and cell characterisation results are discussed. Before describing the details of the electro-thermal model validation and

prediction, the cell experimental data is discussed.

4.5.1   Experimental data

Before performing detailed characterisation tests on the Li-ion cell, initial tests with two configurations are performed to evaluate the forced convection effects on the cell inside the climate chamber. Two different configuration were tested, first, without box around the cell and second, with box around the cell (as discussed in Section 4.3.2) to reduce the forced convection effects. For each configuration two Li-ion cells are tested and the voltage, temperature monitored. Figure 4.16 shows the measured cell voltage for various C rates between 0.2C to 5C at reference temperature (T_{ref} = 25°C) for both configurations. The initial test runs for configuration without box show a noticeable deviation in electrical and thermal results of the two tested cells. The results show significant variation between the two cells, in particular, for high C rates. The deviation in the results was down to the influence of the different cooling conditions due to forced convection inside the climatic chamber. Figure 4.16 also shows results of the configuration with box around the cell to reduce the variations due to a variation in forced convection in the climatic chamber. The results variation between the two cells inside the configuration with box was minimal and hence this configuration is used for all future cell characterisation for electro-thermal modeling.

Figure 4.17a shows voltage measurements at a C rate of 0.5 C for various temperatures ranging between −10°C and 45°C. The voltage measurements show a good correlation between the two tested cells during constant discharge. Figure 4.17 shows the capacity variations with temperature. The voltage and temperature variations between the two cells with cover are minimal. The temperature increase at different ambient temperatures shows different temperature increase. At low ambient the temperature increase is higher compared to the measurement at a higher ambient
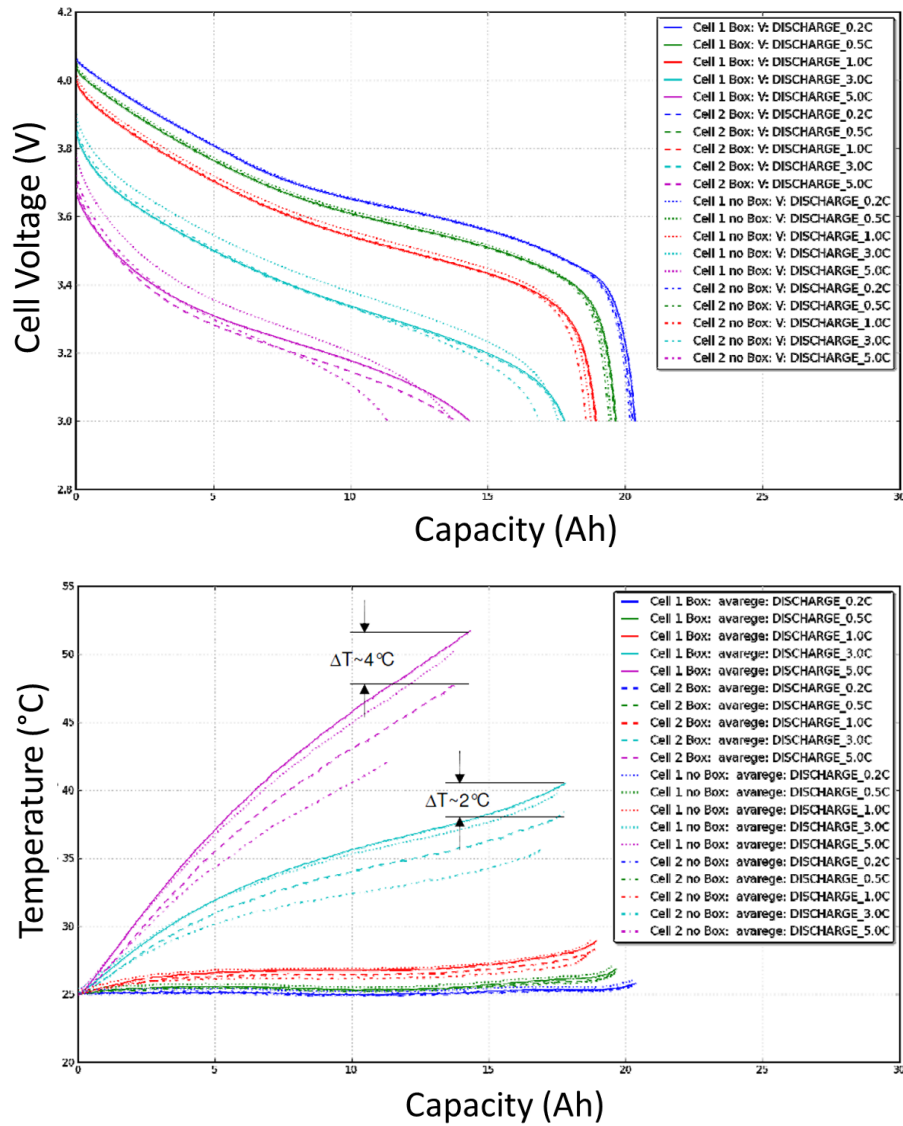
Figure 4.16: a) Measured cell voltage - with and without cell cover configurations, and b) Measured cell temperatures - with and without cell cover configurations

temperature. That is explained due to the change in internal resistance of li-ion cells at lower temperature. Greater the resistance, higher the heat generated across it.

The change in cell capacity and resistance during discharge with a C rate of 0.5C was measured at five different ambient temperatures (T_{ref}). Figure 4.18 shows that the usable cell capacity increases significantly with T_{ref} while the internal resistance of the Li-ion cell decreases. The cell has the maximum usable capacity in a range
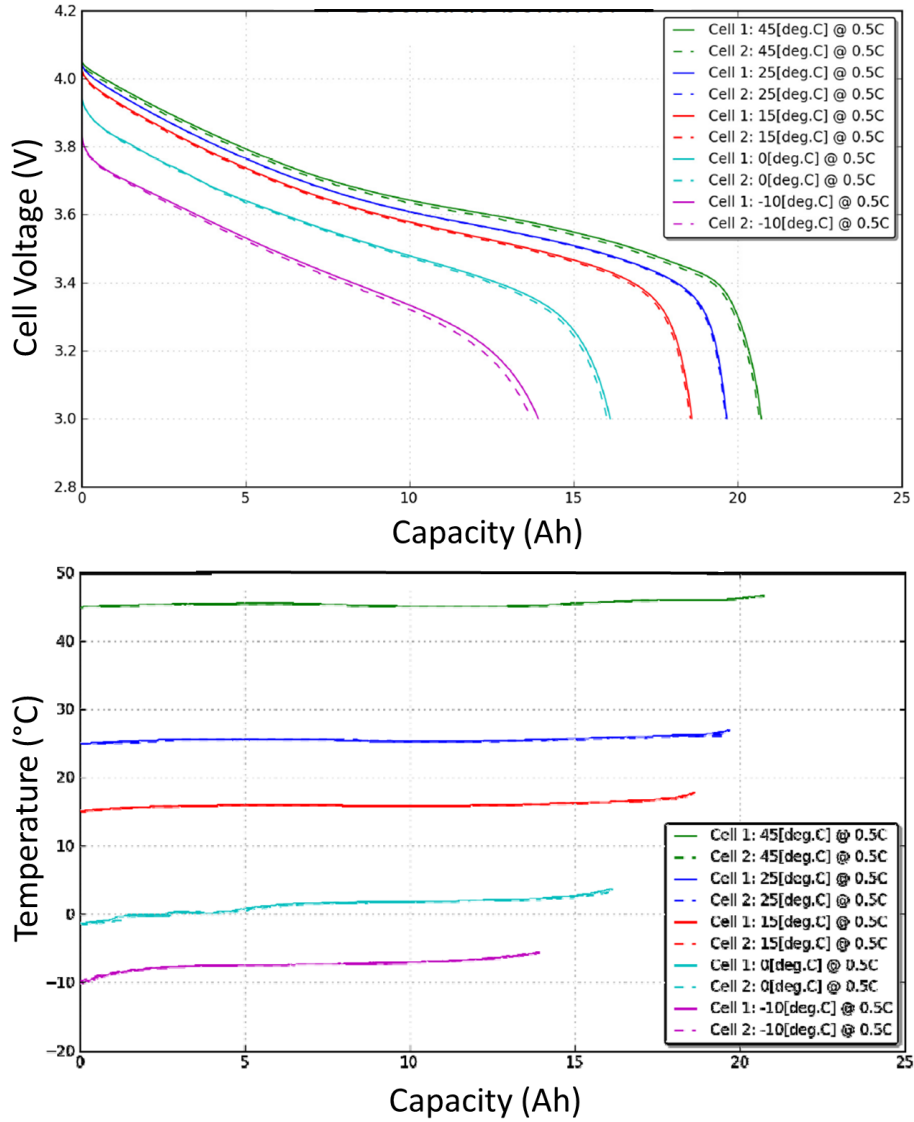
Figure 4.17: a) Measured cell voltages (with cell cover) at constant current discharge of 0.5C, and b) Measured cell temperatures (with cell cover) configuration at constant current discharge of 0.5C

of $25 \leq T_{ref} \leq 45°$C, where the internal resistance remains small. Figure 4.18a shows the usable capacity variations with temperature. As expected the usable cell capacity increases with increase in temperature. At a temperature of -10°C the cell is capable to deliver about 13.8Ah at a discharge rate of 0.5C and at a temperature of 45°C the cell is capable to deliver about 20.5Ah at a discharge rate of 0.5C. he cell has the maximum usable capacity in a range of $25°C \leq T_{ref} \leq 45°$C, where the internal resistance remains small(as seen from Figure 4.18b).
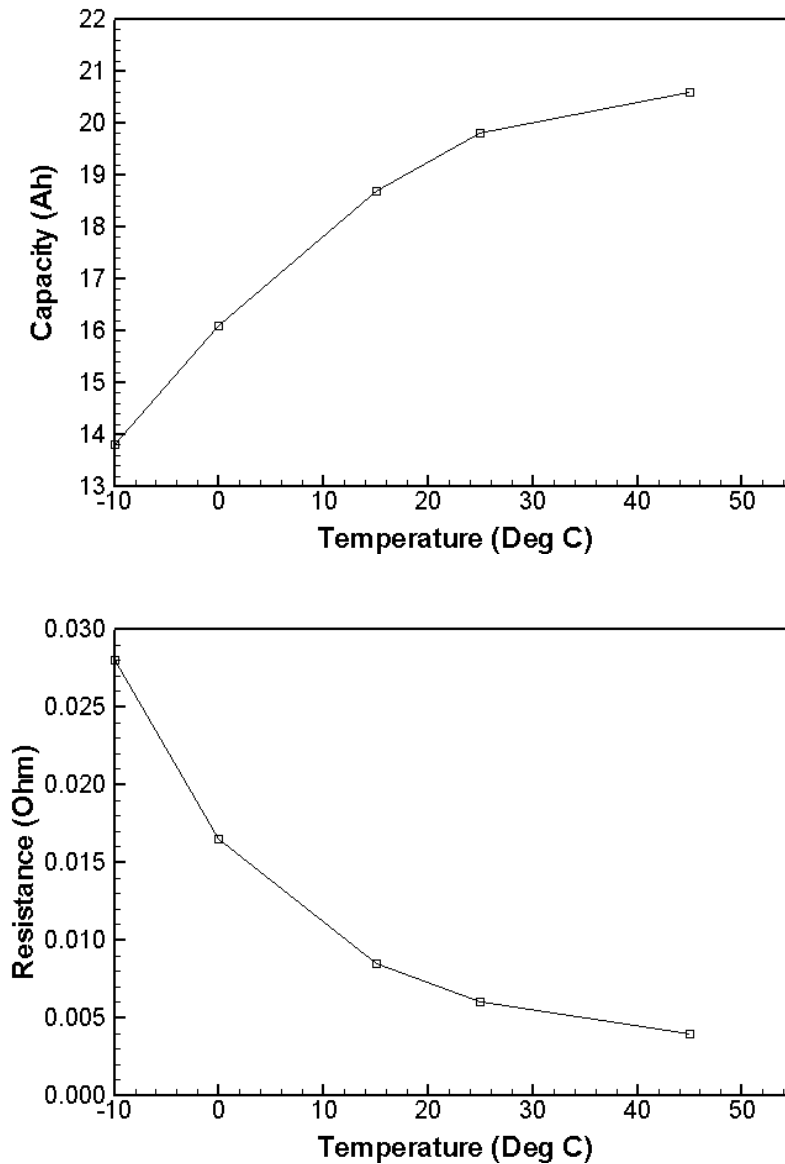
Figure 4.18: Li-ion cell characteristics at several ambient temperatures. a) Capacity, and b) resistance variation with T_{ref}.

The internal resistance of the cell is also strongly influenced by the cell temperature as shown in Figure 4.18b. It is very high at sub-zero temperatures, thus causing a natural block within Li-ion cells preventing them from freely discharging until the temperatures cross the above zero limit. At a temperature of $-10°C$ the internal resistance is about 27 mΩ and at a temperature of $45°C$ the internal resistance is about 4 mΩ.

4.5.2   Model validation

Now the electro-thermal model results will be discussed. A three-dimensional tran-
sient electro-thermal model is used to predict unsteady temperature distribution on
the Li-ion cell for a given electric load cycle and thermal boundary condition. The
proposed electro-thermal model is correlated with test data for various discharge
rates, and the DOD dependency of the electrical properties in Equations 4.12 and
4.13 are determined.

The electro-thermal model predictions are compared with experimental test re-
sults for several discharge rates. The input drive cycle is as described in Figure 4.14.
The input current and the corresponding SOC measurements are as shown in Figure
4.19. As expected, SOC decreases linearly in time during constant current charge
and decreases during discharge.
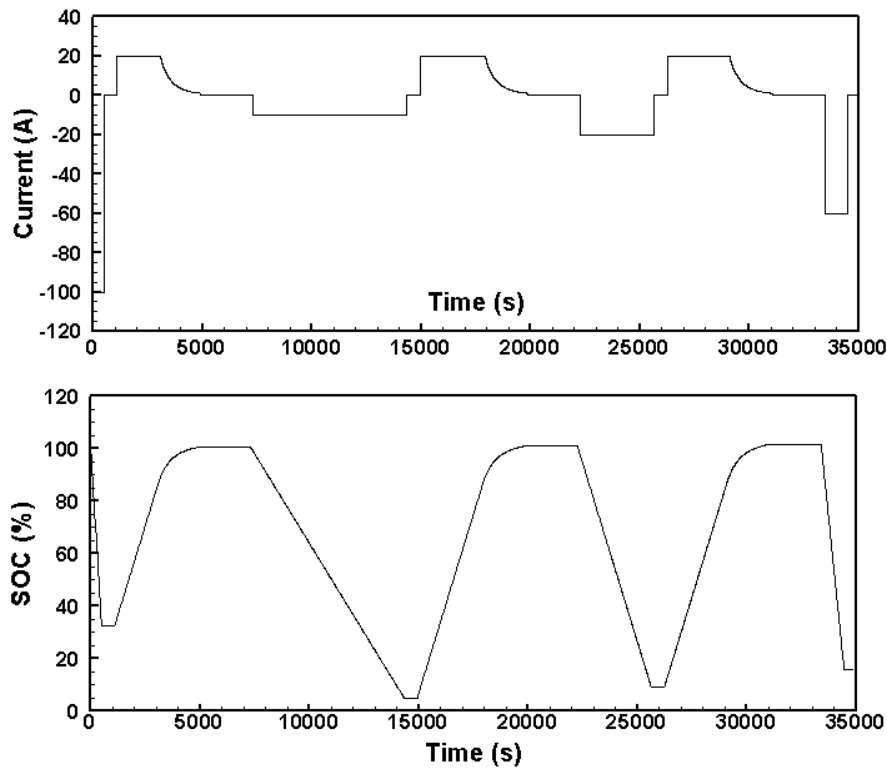
Figure 4.19: Experimental input drive cycle showing. a) Current, and b) SOC

Figure 4.20 shows the average cell voltage and temperature variation during discharge at $T_{ref} = 25°C$. Both average cell voltage and temperature are volume averaged quantities. The electrical behavior prediction compares very well with the experimental test results over a wide range of DOD. The sudden voltage drop observed at the end of discharge (at high DOD) is corrected predicted in the model. The average cell temperature is also in good agreement with the test results. It can be seen that there is a steady increase in temperature during the constant current discharge. As the electrical load increases, the heat generation (given in Equation 4.9) and hence the cell temperature increase. As expected, the largest temperature rise occurs for the highest discharge rate (higher electrical load) due to the increased heat generation from the cell.

A Li-ion cell test cycle with a combination of various charge and discharge rates is then used for validation of charge and discharge behaviour modelling. Figure 4.21 shows a comparison between the experimental test data and the electro-thermal model prediction. Various cell properties are gathered during the test, and the time variation of current, SOC, average cell voltage, and temperature are shown in the figure. A measuring point (P01) is located near the negative tab (see Figure 4.13c). The overall electrical and thermal results from both test and electro-thermal model are in good agreement. The initial cell temperature is the same as the ambient temperature of $T_{ref} = 25°C$. At the beginning of the cycle, the maximum applied discharge current of 5C causes a sharp increase in the cell temperature by more than 25°C within approximately 7 minutes, and the amount of this temperature increase is correctly predicted in the model. The immediate voltage drop during the 5C discharge is also correctly captured. The voltage drop is followed by a relaxation phase with a sudden voltage rise. This is because the internal resistance decreases with the temperature rise due to faster kinetics, hence resulting in an increased cell voltage. Following the residual temperature build up from the 5C discharge and relaxation phase, the temperature remains below 30°C during the charge.
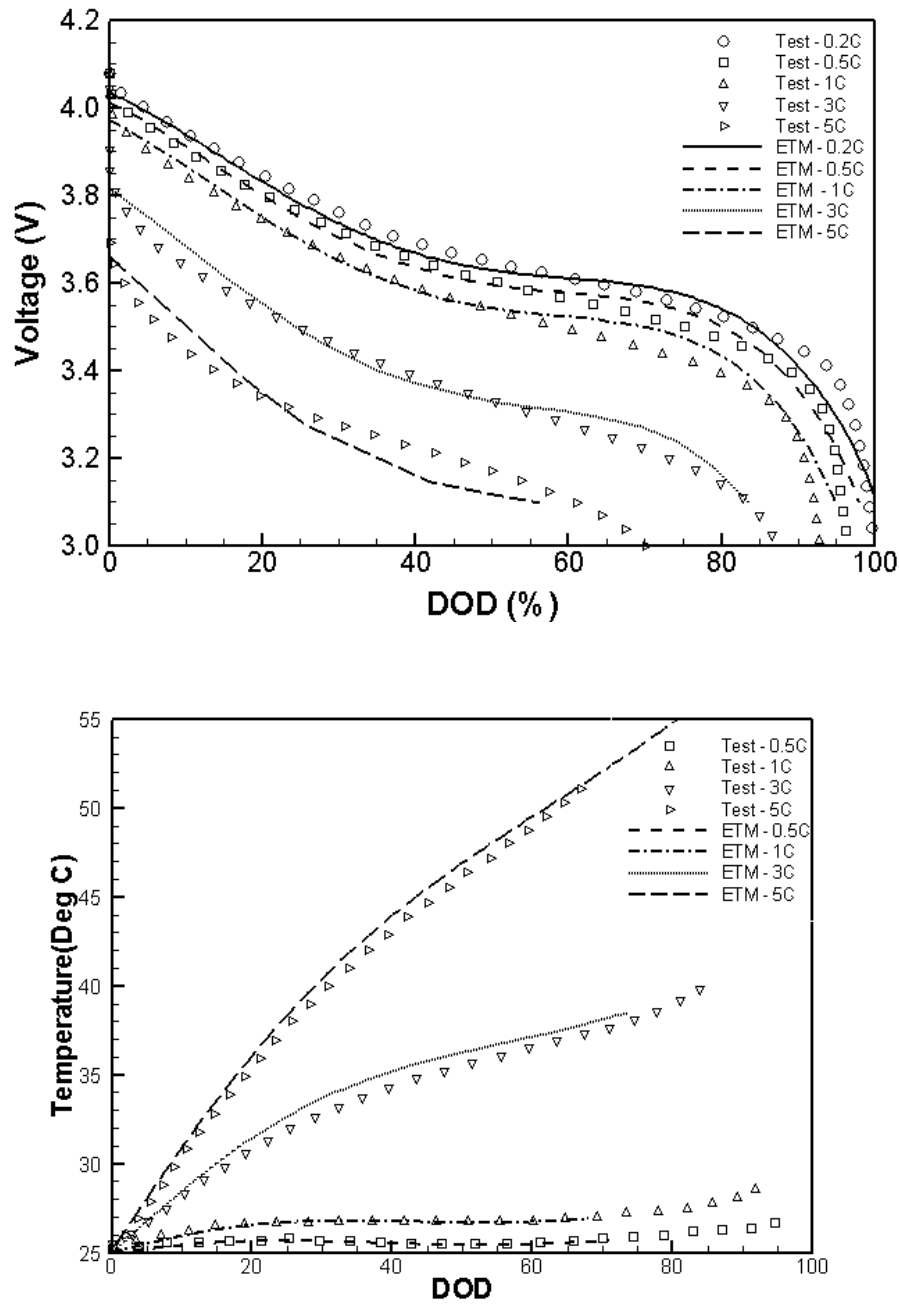
Figure 4.20: Comparison of electro-thermal model prediction with experimental test results at $T_{ref} = 25°C$. a) Average cell voltage, and b) average cell temperature versus DOD at various discharge rates.

A similar trend of voltage and temperature response is also seen for an applied discharge current of 3C at the end of the cycle, and the instantaneous increase in temperature is about 15°C. A modest temperature increase during 1C and 0.5C
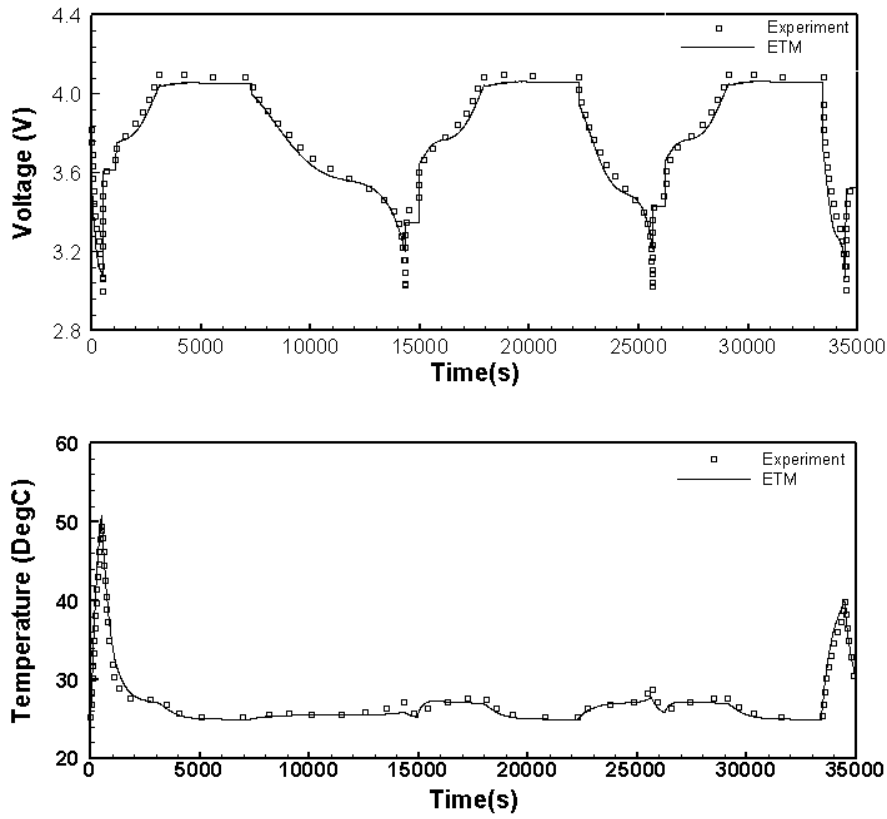
Figure 4.21: Comparison of electro-thermal model prediction with experimental test results. a) Average cell voltage, and b) Temperature at thermocouple location P01.

discharge is also well predicted in the model, displaying a much lower slope of the temperature history.

Figure 4.22 shows the model prediction of temperature contours on the cell surface during the test cycle. Several phases in the test cycle are chosen to display the battery thermal characteristics during both charge and discharge. U, V, W, X, Y, and Z points during the test cycle are depicted in Figure 4.14. Temperature on the positive terminal is higher than the negative terminal due to the lower electrical conductivity of the positive electrode as shown in Table 4.5.

For higher discharge rates of 3C and 5C, the current flow is significantly high in the tab area due to an increased current density (in Equation 4.1), hence high temperature, particularly near the positive tab. The temperature variation on the
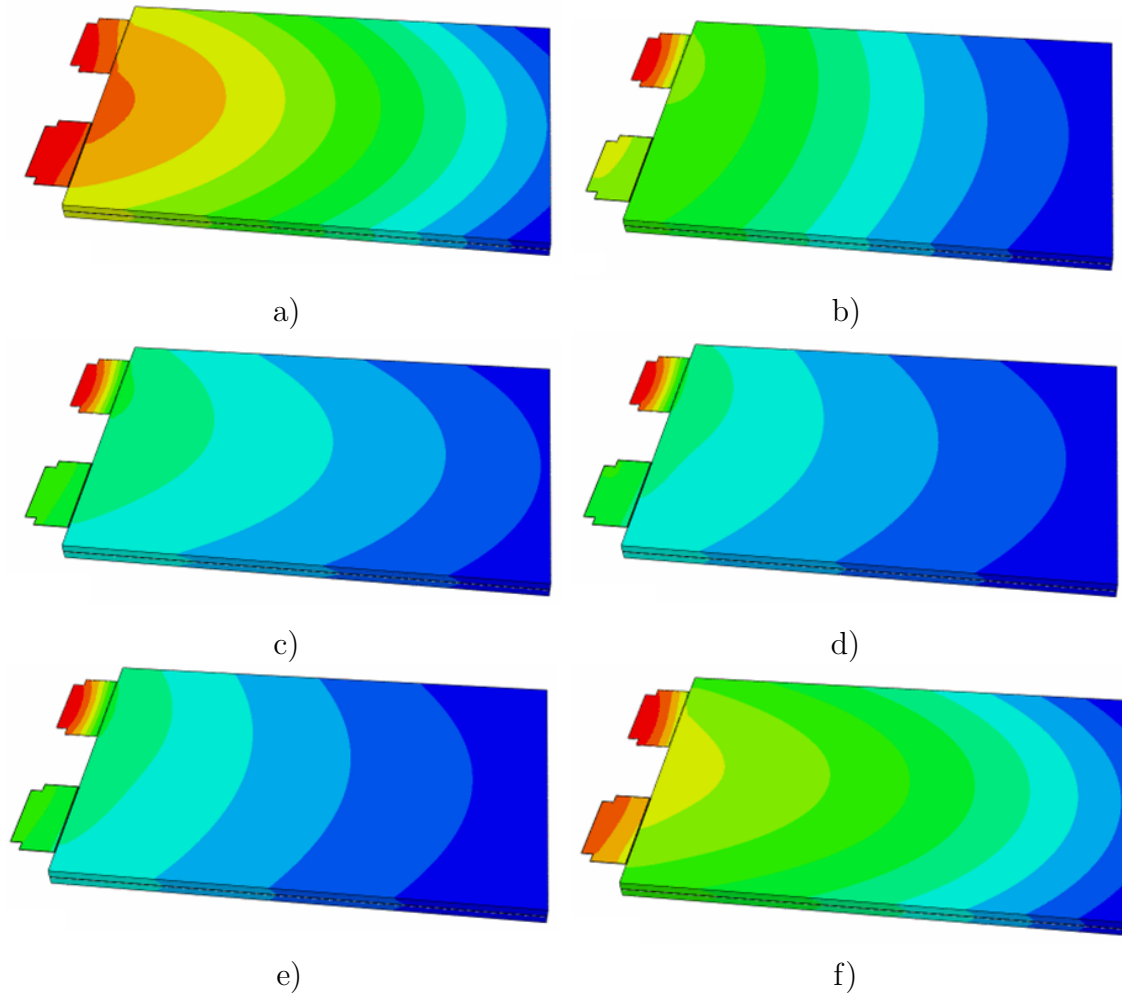
Figure 4.22: Electro-thermal model temperature contour on cell face. a) Point U: 5C discharge, b) Point V: 1C charge, c) Point W: constant voltage step, d) Point X: 0.5C discharge, e) Point Y: 1C discharge, and f) Point Z: 3C discharge. Contour plot legend: High temp(Red), Low temperature(Blue)

cell progressively reduces for lower discharge rate as shown in the contour plot. The three-dimensional model is able to predict the temperature variation on the cell surface. A similar temperature variation on the tabs and cell were observed in the recent cell test thermal images of Kim *et al.* [109]. The results reported in this section has provided a good validation for the current electro-thermal model. An excellent agreement is found between the Li-ion cell model prediction and the test data for charge and discharge, which clearly demonstrates the capability of the current Li-ion cell model to predict electro-thermal behaviour of the cell for different

loading cycles.

4.5.3   Drive cycle simulation

The electro-thermal model is now applied to predict the Li-ion cell behaviour for vehicle operating conditions. Two vehicle operating conditions for the electro-thermal simulation are considered in this section. The first one (Cycle A) is the drive cycles during a hot environment test of an actual electric vehicle. From the TATA Indica Vista EV (prototype configuration without any active cooling) hot environment tests at an proving ground during the summer, a gradual temperature increase was reported for 12% grade climb at 40 km/h [112]. It was also observed that at the end of the battery capacity there was a significant increase in battery temperature, indicating changes in internal resistance. The second one (Cycle B) is for a more severe test, where the vehicle was repeatedly accelerated from 20 km/h to 70 km/h and then braked back to 20 km/h. In this case, the battery temperature traces exhibited a small saw-tooth effect of around $0.2 \sim 0.5°$C due to the transient peaks in the battery charge and discharge [112].

Figure 4.23 shows the cell-level electro-thermal prediction for Cycle A. The simulation is performed for a constant discharge cycle of 1.2C (24 A), representing an electrical loading for a 40 km/h, 12% (ascending slope) climb vehicle operating condition. Figure 4.23 shows the time variation of current, SOC, average cell voltage, and temperature on the cell surface for Cycle A. Three measuring points (P01, P03, and P10, see Figure 4.13c) are located near the negative tab (P01), positive tab (P03), approximately halfway towards the positive tab side (P10). The SOC prediction shows that the cell would completely discharge in about 3000 seconds as would be expected for a cell of 20 Ah nominal capacity. The temperature increases at different locations are gradual, and similar to the one observed in the vehicle level hot environment tests. The temperature rise time constant is approximately 300

seconds. There is an additional increase in the temperature at the end of discharge, which corresponds to an increased resistance.
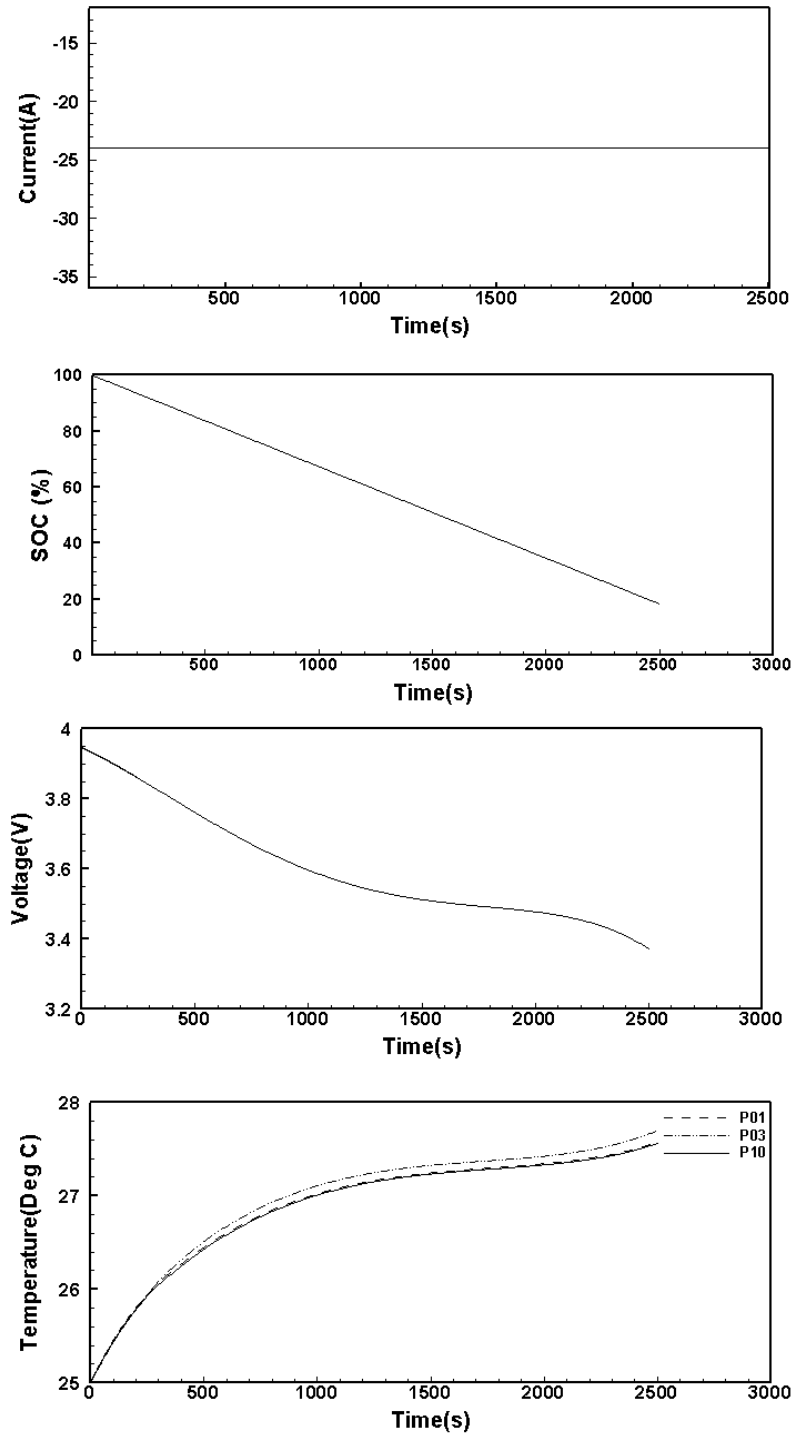
Figure 4.23: Electro-thermal model prediction for a mild electric vehicle operating condition (Cycle A). a) Current, b) SOC, c) average voltage, and d) temperature at P01, P03 and P10.

The cell-level electro-thermal model is then applied to a more severe vehicle operating condition (Cycle B), where a vehicle is repeatedly accelerated and decelerated between 20 km/h and 70 km/h. Each cycle of 30 seconds is repeated for a total of 150 seconds to understand the accumulated thermal behaviour. The discharge step that represents acceleration was simulated for 1.7C (-34 A), and the charge step that represents braking was simulated for 0.83C (17 A). Figure 4.24 shows the time variation of current, SOC, average cell voltage, and temperature at three measuring points (P01, P03, and P10) on the cell surface for Cycle B. A small saw-tooth effect is clearly seen in the cell temperature response at the charge/discharge transients, and a similar feature was observed in the vehicle level hot environment tests [112].

It is found that the temperature increases by more than 1°C during an aggressive cycle of 150 seconds at a modest ambient temperature. This would mean a substantial temperature increase for a standard one hour aggressive hot environment test. Considering the fact that optimum Li-ion cell performance is found at around 25°C cell operating point (see Figure 4.18), this would mean that for such aggressive drive cycles the cells would potentially need an active temperature control [44].

4.6 Conclusions

A three-dimensional electro-thermal cell model is developed for predicting the electrical and thermal behaviour of a Li-ion polymer cell. The fully coupled model has been implemented based on a finite volume method. The DOD dependency of the cell is characterised using the experimental test data. The Li-ion cell test data are utilised to validate the electro-thermal model. The electro-thermal model predicts the cell temperature and voltage magnitudes accurately for the test load cycle. The electro-thermal model is then used to predict the cell level performance for two dif-
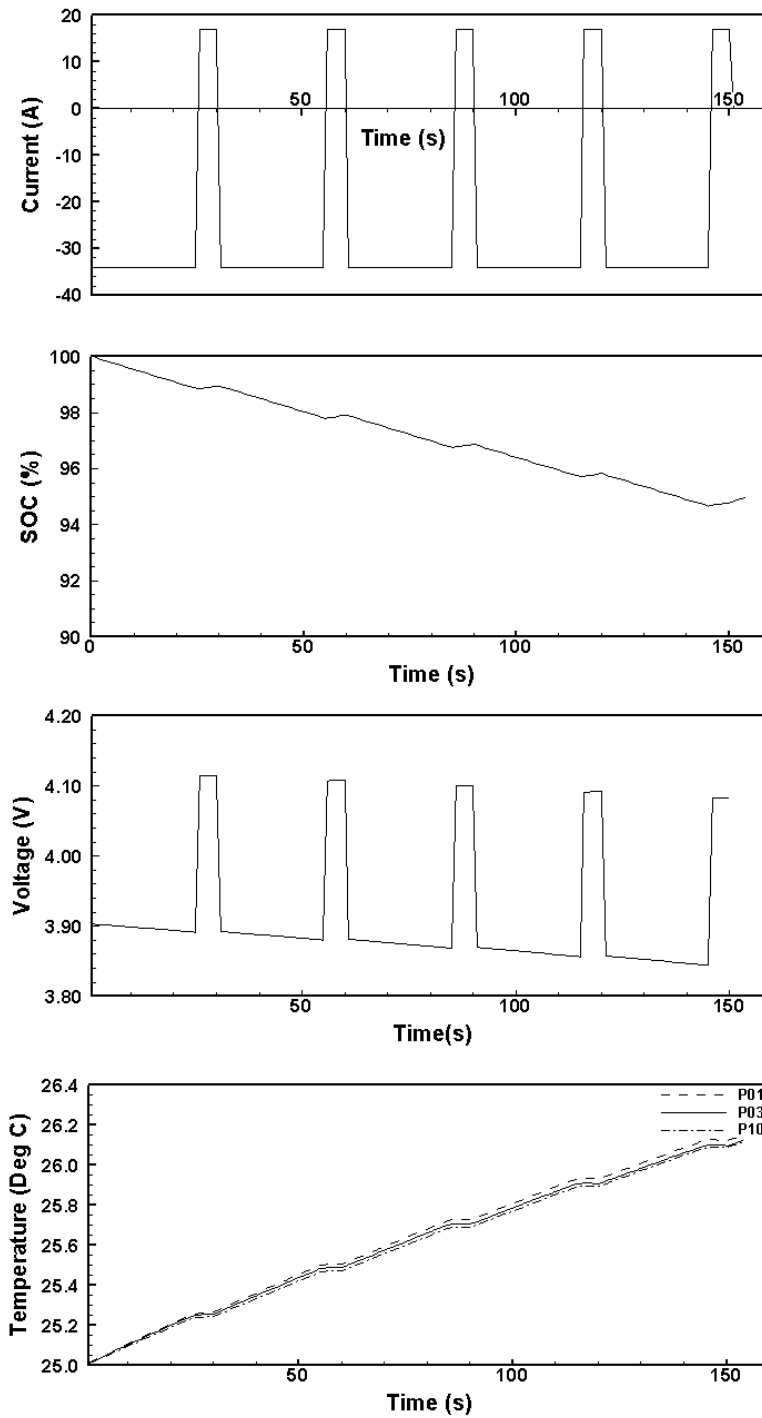
Figure 4.24: Electro-thermal model prediction for a severe electric vehicle operating condition (Cycle B). a) Current, b) SOC, c) average voltage, and d) temperatures at P01, P03 and P10.

ferent vehicle drive cycles: one for a mild EV operating condition, and the other for a more severe operating condition. It is found that a significant temperature rise

occurs during the severe drive cycle, and an effective temperature control is required to maintain the optimal cell performance. The model has shown the potential to be used in battery thermal management studies for EV/HEV applications. The electro-thermal data and insights on cell surface temperature variation would aid better design of battery thermal management systems.

5

Indirect liquid cooling using serpentine

channels

5.1 Introduction

The second key aspect of thermal management is discussed *i.e.*, predicting how the heat generated is being removed from the cells. One of the more recent developments in battery thermal management strategies is in the use of indirect liquid cooling using cooling plates [79]. Recently, active indirect liquid cooling using serpentine channels

is used for battery thermal management for EV applications [9]. The coolant passes through the serpentine channels housed in a battery cooling plate removing the heat generated by Li-ion cells. The heat in the coolant is then finally dissipated to air through the radiator [60]. The use of a cooling plate with serpentine channels provides greater flexibility for cell thermal control by being able to precondition the coolant when required at the battery inlet to manage the required operating temperatures within the cells. Thermal management by indirect liquid cooling using cooling channels has been also used in applications like fuel cells [113] and electronic cooling [114].

Several fundamental studies for flow through channels were reported in the literature [115, 116]. Chen *et al.* [117] compared six different cooling plate designs for fuel cells, comparing serpentine type designs with parallel types. They found that the cooling effect of serpentine designs is better than that of parallel designs. Kou *et al.* [118] performed three-dimensional numerical simulation of micro channels of various heights and widths to find the optimum thermal performance. Yuan *et al.* [119] performed numerical simulations of fully developed laminar flow and heat transfer for ducts with rectangular and trapezoidal cross sections. It has also been verified that mass transfer rate and aspect ratio affect the friction factor and Nusselt number. Lee and Garimella [120] conducted numerical simulations to predict steady laminar heat transfer of fluid through rectangular cross sections. Recently, Xie *et al.* [121] analysed the heat transfer and pressure drop characteristics for laminar channel flow. They found that a narrow and deep channel has better heat transfer than a wide and shallow channel, in spite of the high pressure drop penalty.

Majority of the previous work incorporating coolant channels was related to micro and mini channels for fuel cells. These type of channels are not only capable of relatively higher levels of heat transfer but also inherit higher levels of pressure drop. For an EV application high levels of pressure drop would be counterproductive

reducing the vehicle range considerably due to increased pumping power. Reduced pumping power leads to small size pump which leads to reduced energy drain from the cells and thereby enabling optimum vehicle range for EV. Both micro and mini channels have relatively high pumping power required for the coolant circulation and for an EV application the coolant channel pressure drop has to be minimised in order to ensure high overall EV efficiency. Battery thermal management strategy for an electric vehicle requires keeping the cell temperature uniform, reduce the cell peak temperatures and minimise pressure drop for indirect liquid cooling. A normal serpentine channel with ability to soak in modest level of heat flux with a low pressure drop is the most appropriate for electric vehicle thermal management. The key to optimum scenario would be to minimise the pressure drop while maximising the heat transfer capability at the same time. In the previous numerical studies on channels conjugate heat transfer was not considered. For design of a thermal management systems detailed understanding of the heat transfer path, temperature distribution/ uniformity on the cell as well as the cooling plate with coolant channel is very critical. In this study, three-dimensional conjugate heat transfer of laminar serpentine channel flows with a rectangular cross section is considered. The effect of various design parameters such as channel aspect ratio, radius of curvature, coolant flow rate on the thermo-hydraulic performance of the coolant channel. The main objective is to maximise the heat transfer, and minimise the pressure drop.

5.2   Problem definition

5.2.1   EV battery pack configuration

A liquid cooling plate forms an important part of a battery thermal management system. Figure 5.1 shows a thermally managed battery pack [9]. The battery pack consists of several battery modules (a stack of Li-ion cells) and liquid cooling plates,

each battery module is sandwiched between two cooling plates. The heating/cooling of the battery module is achieved by pumping warmed/cooled/subcooled coolant through the cooling plate. Coolant temperature is precisely controlled to enable battery pack temperature to be maintained within the ideal operating range [44] for maximum battery pack performance, life, reliability and safety.

The heat transfer occurs via conduction from the battery modules to the cooling plates, then by convection through the coolant from where the heat is removed into the environment (via a radiator plumbed in the vehicle cooling network). The liquid cooling plate which consists of serpentine channels needs to maximize the heat transfer with minimum pressure drop which would enable a smaller size pump and hence reducing parasitic losses. Minimizing parasitic losses within the thermal management system is a key requirement for maximizing vehicle range. The cooling plate which consists of serpentine channels hence needs to be optimized for maximum heat transfer while minimizing pumping power. By optimizing the design, the BTM system draws minimum power from the EV system thus maximizing vehicle range. The current work hence is a study to understand the effect of aspect ratio of the channel cross section, gap between the serpentine channels.

Battery module

This coolant channel study is for a EV Li-ion pouch battery pack, and the cooling plate housing the serpentine channels is mounted on the side of the battery module. The battery modules are stacked one after another to make a battery pack. Each battery module consists of Li-ion pouch cells as shown in Figure 5.1. These are arranged with cooling plates placed on two sides as shown in Figure 5.1. Each cell within the module is housed in a plastic cassette frame. A heat transfer plate made of a thin aluminum sheet wrapped around the cell provides an efficient heat transfer path from the cell core to the cooling plate. The heat transfer plate is a planar
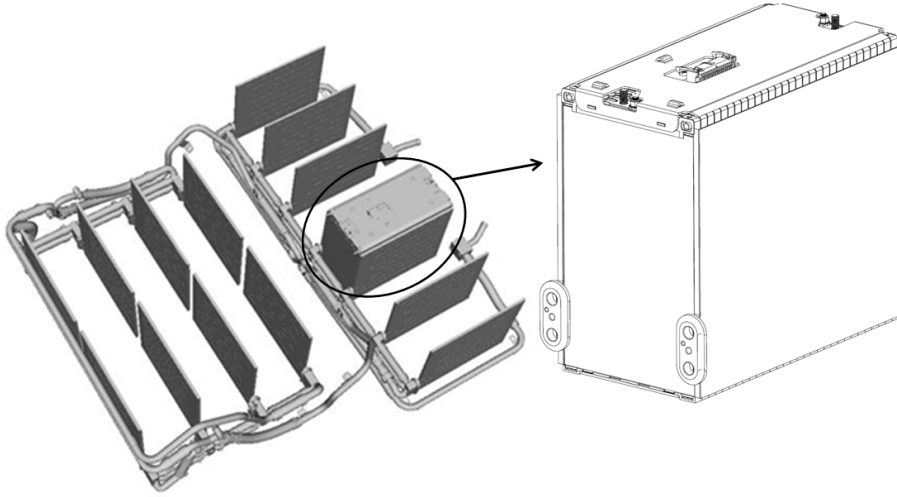
Figure 5.1: A EV battery pack representation with battery module, cooling plates, and interconnecting coolant lines.

member covering one longitudinal side of the cell and extending along the transverse side of the cell. The side face of heat transfer plate along with the thickness of the cell connects to the coolant jacket plate, this facilitates a conduction path between cell and cooling plate.

5.2.2   Cooling plate channel geometry details

A schematic diagram of the battery cooling plate is shown in Figure 5.2. The size of the rectangular aluminium cooling plate was $L_1 \times L_2$ for all simulations; the thickness of the plate was H. The serpentine coolant channel was housed inside the cooling plate. The channel had a rectangular cross section of $A = a \times b$, where a is the width and b is the height (or thickness) of the channel. The cooling plate thickness, H, varies accordingly with the channel height, b. Since the channel side wall was very thin (1 mm), $b \approx H$ in this study. The gap between the channels was determined by the radius of curvature (r_c) of the U-bend; $g = 2r_c$. Table 5.6 lists the various dimensions the cooling plate and the rectangular channel for the baseline case. Various geometries of serpentine channels were considered with
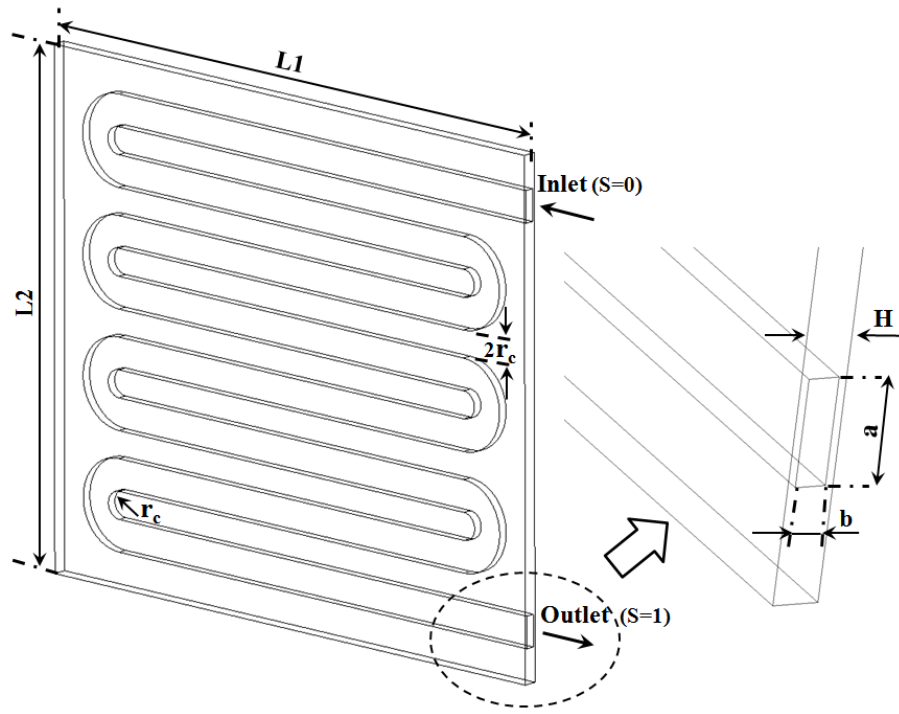
Figure 5.2: Schematic diagram of coolant channel housed in the cooling plate.

different aspect ratios ($A_R = a/b$) and radii of curvature (r_c). Please note that the cross-sectional area ($A = ab$) of the channel was kept constant for all the cases considered, while the hydraulic diameter ($D_h = 2ab/(a + b)$) varied for each case. For the baseline case, the aspect ratio is $A_R = 3.5$; the gap between the channels was $g = 6b$ with $r_c = 3b$. The Reynolds number of the channel was $Re = 435$. Details are summarised in Table 5.1.   As for boundary conditions, a uniform velocity was

Table 5.1: Baseline case.

A_R	r_c/D_h	Re
3.5	2	435

Table 5.2: Grid independence cases.

Cases	G1	G2	G3	G4	G5
Grid size	1.0×10^6	1.3×10^6	1.6×10^6	2.1×10^6	2.8×10^6

Table 5.3: Aspect ratio cases.

Cases	A1	A2	A3	A4	A5	A6
A_R	6	3.5	2.2	1.5	1.14	0.875

Table 5.4: Radius of curvature cases. D_h is the hydraulic diameter of the baseline case.

Cases	C1	C2	C3	C4
r_c/D_h	0.5	1	2	3

Table 5.5: Mass flow rate.

Cases	F1	F2	F3	F4	F5
Re	290	435	580	725	870

applied at the inlet, and the inlet temperature of the coolant was 25°C. The pressure boundary condition was prescribed at the outlet of the coolant channel while no-slip boundary conditions were applied on the channel walls. A uniform heat flux was applied on the cooling plate surface in contact with the battery module, and the adiabatic boundary condition was employed on the remaining four side walls of the cooling plate.

5.2.3 Serpentine Channel

Figure 5.2 shows the serpentine channel geometry, the projection area of the serpentine channel can be calculated

$$A_p = (n + 1)al_c + 2ac + \frac{n}{2}\pi \left((r_c + a)^2 - r_c^2 \right),$$
(5.1)

where l_c is the length of the straight section of the channel, n is the number of bends, and $L_1 = l_c + 2c$. Since

$$h = na + 2nr_c. \tag{5.2}$$

where h is the distance between the centres of the inlet and outlet, Equation 5.1 becomes

$$A_p = (n+1)al_c + a(L_1 - l_c) + \frac{\pi}{2}ah, \tag{5.3}$$

$$= a\left(nl_c + L_1 + \frac{\pi}{2}h\right). \tag{5.4}$$

This shows that the project area A_p increases linearly with the number of U-bend. The contact area of a U-bend is

$$A_s = 2(n+1)bl_c + 4bc + nb\pi\left(2r_c + a\right), \tag{5.5}$$

$$A_s = 2nbl_c + 2bL_1 + b\pi h, \tag{5.6}$$

$$= 2b\left(nl_c + L_1 + \frac{\pi}{2}h\right), \tag{5.7}$$

$$= 2b\frac{A_p}{a} = 2\frac{A_p}{A_R}. \tag{5.8}$$

Table 5.6: Design parameters for coolant channel in mm.

L_1	L_2	l_c	h	c	a	b	r_c
263	227	189	182	37	14	4	6

Table 5.7: Case Description.

Grid independence cases	Grid size	
G1	2.8×10^6	
G2	2.1×10^6	
G3	1.6×10^6	
G4	1.3×10^6	
G5	1.0×10^6	
Aspect ratio cases	$a \times b$ (mm $\times$ mm)	D_h
A1 (AR=6)	18×3	0.0052
A2 (AR=3.5)	14×4	0.0062
A3 (AR=2.2)	11×5	0.0069
A4 (AR=1.5)	9×6	0.0073
A5 (AR=1.14)	8×7	0.0075
A6 (AR=0.875)	7×8	0.0075
Radius of curvature cases	Radius (gap)	
C1	$3D$ (18 mm)	
C2	$2D$ (12 mm)	
C3	$1D$ (6 mm)	
C4	$0.5D$ (3 mm)	
Mass flow rate cases	Flow rate [kg/s]	
F1	0.01	
F2	0.015	
F3	0.02	
F4	0.025	
F5	0.03	

5.3   Computational details

A conjugate heat transfer was considered in this study. For the coolant flow, the governing equations are the three-dimensional, incompressible Navier-Stokes and energy equations. The continuity and momentum equations can be written as,

$$\frac{\partial u_i}{\partial x_i} = 0, \tag{5.9}$$

$$\frac{\partial u_i}{\partial t} + \frac{\partial}{\partial x_j} u_i u_j = -\frac{1}{\rho}\frac{\partial p}{\partial x_i} + \frac{\partial}{\partial x_j}\left(\nu \frac{\partial u_i}{\partial x_j}\right), \tag{5.10}$$

and the energy equation with the viscous dissipation term is given by

$$\frac{\partial T}{\partial t} + \frac{\partial}{\partial x_j} u_j T = \frac{\partial}{\partial x_j} \left(\frac{k}{\rho c_p} \frac{\partial T}{\partial x_j} \right) + \frac{\nu}{c_p} \left(\frac{\partial u_i}{\partial x_j} + \frac{\partial u_j}{\partial x_i} \right) \frac{\partial u_i}{\partial x_j},$$
(5.11)

where u_i is the velocity component, p the pressure, T the temperature, ρ the density, ν the kinematic viscosity, k the thermal conductivity, and c_p the heat capacity of the fluid. A standard conduction heat transfer equation was solved for the solid part.

The governing equations were solved using a second-order finite volume method and the SIMPLE algorithm for pressure-velocity coupling. For discretisation, a second-order accurate upwind scheme was used. Simulations were carried out using the finite-volume CFD code, FLUENT [122]. The three-dimensional computer model of the cooling plate was constructed using ICEM [123] software, and hexahedral computational grids were generated for the geometry shown in Figure 5.2. For solid, the unsteady three-dimensional heat conduction equation was solved:

$$\rho c_p \frac{\partial T}{\partial t} = \frac{\partial}{\partial x} \left(k_x \frac{\partial T}{\partial x} \right) + \frac{\partial}{\partial y} \left(k_y \frac{\partial T}{\partial y} \right) + \frac{\partial}{\partial z} \left(k_z \frac{\partial T}{\partial z} \right),$$
(5.12)

where k the effective thermal conductivity of the solid.

An additional coordinate, s, is introduced in this study to describe changes along the channel centreline; s represents the non-dimensional centreline location, such that $s = 0$ at the inlet and $s = 1$ at the outlet of the coolant channel (see Figure 5.2). Three average temperatures are defined along the channel centreline to aid thermal characteristics analysis: T_w is the local channel wall temperature averaged along the perimeter, T_m is the local bulk mean fluid temperature averaged over the cross-sectional area, T_m is the mass weighted fluid temperature averaged

over the cross-sectional area:

$$T_w(s) = \frac{1}{\Gamma} \int_\Gamma T d\Gamma, \tag{5.13}$$

$$T_m(s) = \frac{1}{A} \int_A T dA, \tag{5.14}$$

$$T_m(s) = \frac{1}{U_m A} \int_A u T dA, \tag{5.15}$$

where Γ is the wetted perimeter, A is the cross-sectional area, and U_m is the bulk mean velocity. In this study, the Reynolds number is defined as:

$$Re = \frac{U_m D_h}{\nu}, \tag{5.16}$$

and the Nusselt number is defined as:

$$Nu = \frac{h_l D_h}{k}. \tag{5.17}$$

The local heat transfer coefficient h_l is given as [124]

$$h_l = \frac{q''}{T_w - T_m}, \tag{5.18}$$

where q'' is the heat flux.

5.4 Results and discussion

5.4.1 Validation

Prior to the main simulations of the cooling plate with the serpentine channel, a three-dimensional U-bend flow simulation was conducted to ascertain the reliability and accuracy of the present numerical methods [125]. The flow configuration was

chosen to match the experiment of Hille et $al.$ [126]. The cross-sectional area of the duct was a square ($i.e.$, $A_R = 1$) with a curvature ratio of $r_c/D_h = 6.5$. Simulations were performed for a Reynolds number of $Re = 574$, and the corresponding Dean number ($K = Re(D_h/r_c)^{0.5}$) was $K = 226$.
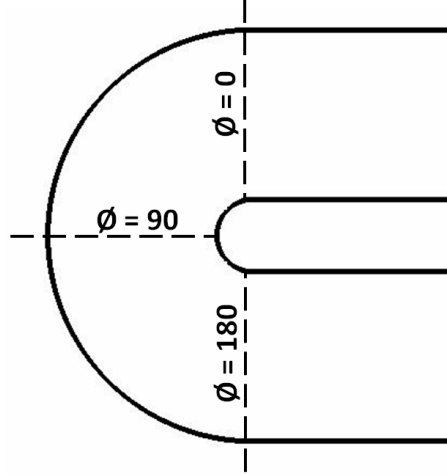
Figure 5.3: Location of the bend defined in terms of ϕ.
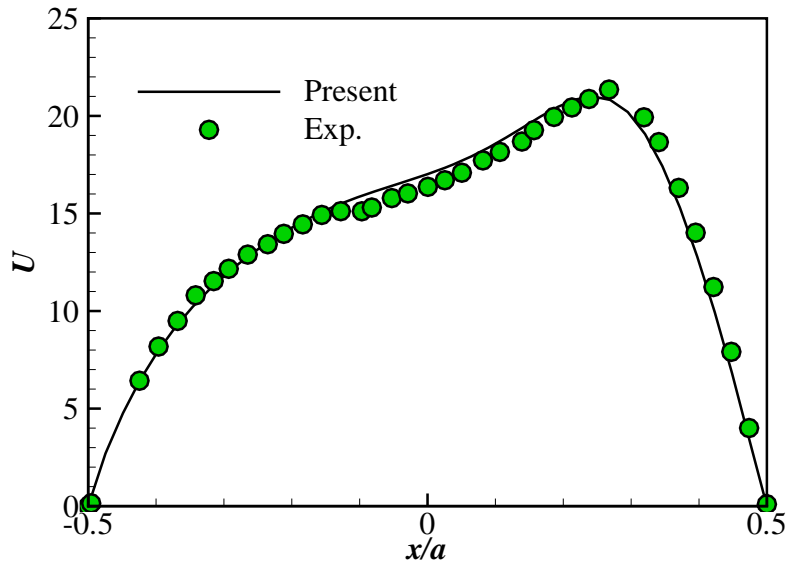
Figure 5.4: Normalised azimuthal velocity as a function of radial location x at channel mid-height.

The radial variations of azimuthal velocity were compared with the measure-

ments of Hille *et al.* [126] at various locations along the mid-span of the duct. The bend location is defined in terms of ϕ as shown in Figure 5.3. Please note that $\phi = 0$ indicates the beginning, and $\phi = 180$ the end of the bend section. Figure 5.4 shows the normalised azimuthal velocity at $\phi = 90$. Acceleration of the flow along the outer wall is clearly captured in the simulation. Counter-rotating streamwise vortices and an additional pair of counter-rotating vortices near the outer wall are predicted, and these are in good agreement with flow visualisation evidence. These findings are also consistent with those of Ghia and Sokhey [127] and Chung *et al.* [125]. The present U-bend results are in excellent agreement with the experimental data of Hille *et al.* [126], demonstrating that the numerical methods employed in this study are adequate for the serpentine coolant channel flow simulation.
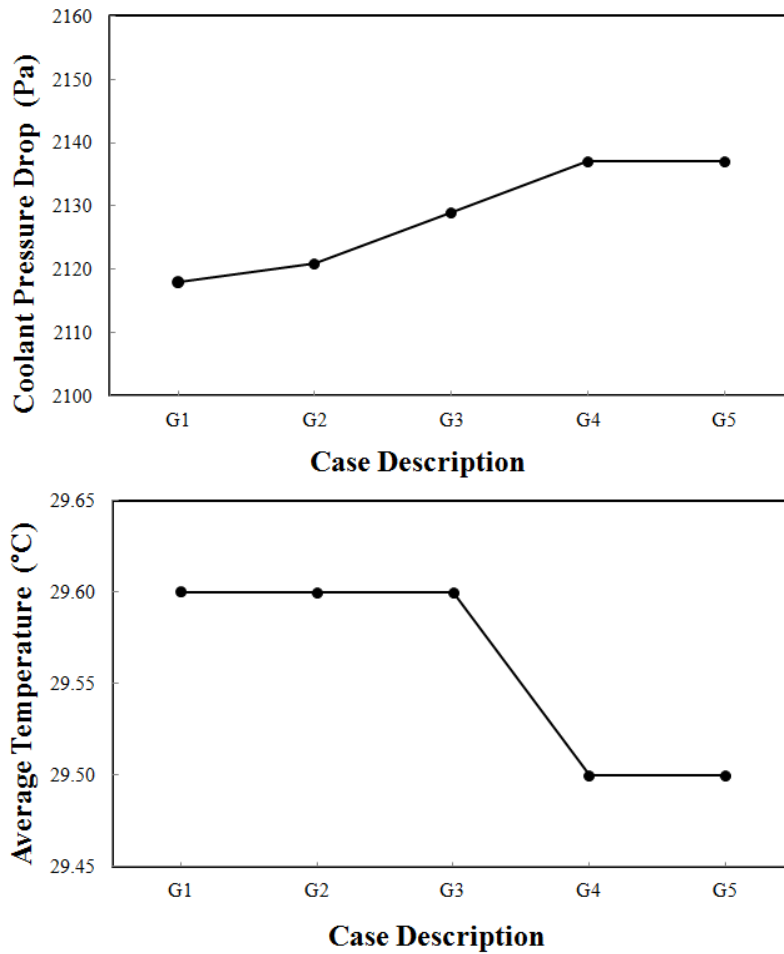
Figure 5.5: Mesh Sensitivity cases. a) Δp, and b) T_{avg}.

In addition to the U-bend validation, a grid independence test was performed for the cooling plate simulation. The baseline case was chosen based on preliminary simulations. Details are given in Section 5.2.2 and also in Table 5.1. Five hexahedral grids were used with grid points ranging between 1×10^6 to 2.8×10^6, and details are summarised in Table 5.2. Figure 5.5 shows the coolant pressure drop (Δp) and the average cooling plate surface temperature (T_{avg}) from the grid independence test. Coolant pressure drop is calculated as $\Delta p = $ outlet pressure - inlet pressure, inlet and outlet pressures are calculated at the entry, exit of the rectangular serpentine channel respectively. The variations in Δp and T_{avg} for the grids used were about 20 Pa and 0.1°C, respectively, and little changes were observed between 2.1×10^6 and 2.8×10^6 grids. Based on these results, the 2.1×10^6 grid was used in the main simulations. Table 5.7 summarises the various simulations carried out to examine the effects of aspect ratio, radius of curvature and mass flow rates.

5.4.2   Aspect ratios

First, the effect of the aspect ratio of the channel cross section was examined. The aspect ratio is defined as $A_R = a/b$, where a is the width, and b is the height of the coolant channel. Please note that the cross-sectional area of the coolant channel ($A = a \times b$) was kept constant, so the channel height decreased as the channel width increased (see Figure 5.2). Six A_R cases including the baseline case were considered. (Case A2 is identical to the baseline case). Details are summarised in Table 5.3. Apart from A_R (and D_h), all other simulation parameters were the same in all cases, so that only the effect of A_R could be scrutinised. The channel Re number in the baseline case was $Re = 435$.

Figure 5.6 show the flow behaviour close to the bends. The coolant flow is anticlockwise and ϕ varies from 0 at the beginning of the bend to the 180 at the end as shown in Figure 5.6. The flow structures in the bend for various aspect ratio
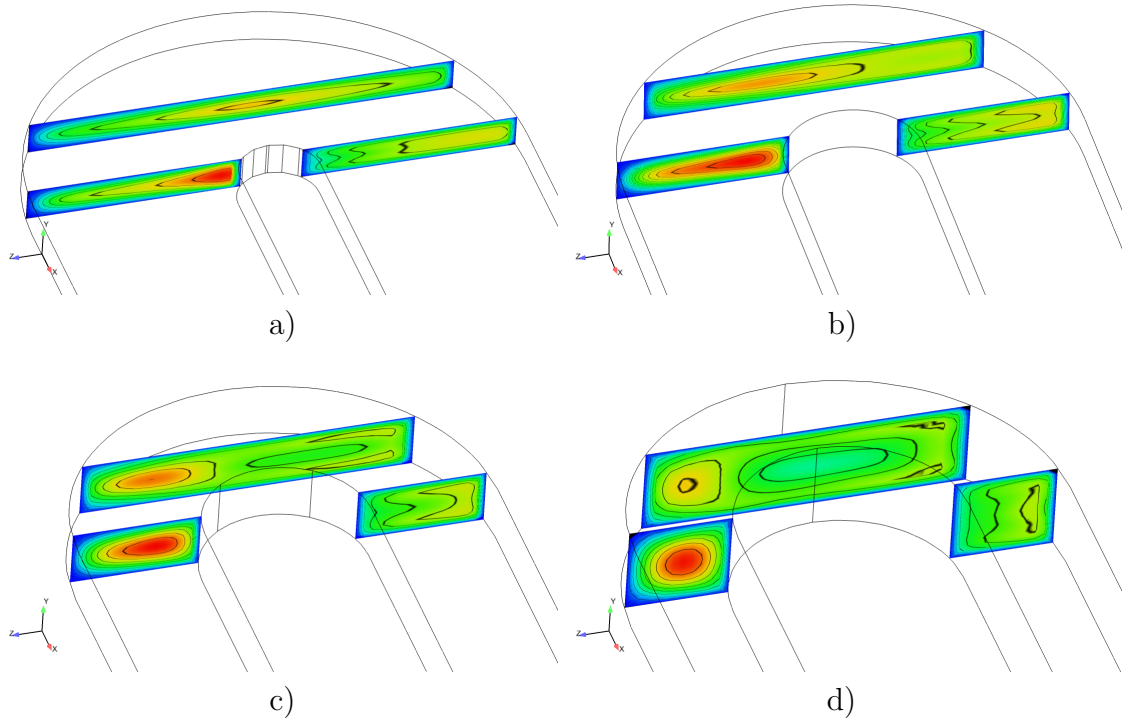
Figure 5.6: Velocity contours near the third bend for various aspect ratio cases. a) A1, b) A2, c) A3, and d) A4.

cases are shown. From the velocity contours, the change in the flow structure cased by the bend is clearly seen. The existence of the counter-rotating Dean vortices is evident. At the beginning of the bend ($\phi = 0$), the outer shear layer becomes thicker due to high pressure, and the high velocity region moves towards inner wall of the U-bend; this is more evident for high aspect ratio cases.

Figure 5.7 shows the planar velocity profile for various aspect ratios. The figure shows the change in the high velocity region as it moves from $\phi = 0$ to $\phi = 180$ along the bend. Figures 5.8a, and 5.8b shows the velocity magnitude in the mid plane and close to the channel wall respectively for case A2. The velocity magnitude at the two planes confirms the movement of the high velocity region towards the inner wall of the U-bend. Figure 5.8c, and 5.8d shows the temperature contour plots on the coolant channel walls. Thicker shear layer due to higher pressure at the beginning of the bend reflects higher temperature on the channel side walls.
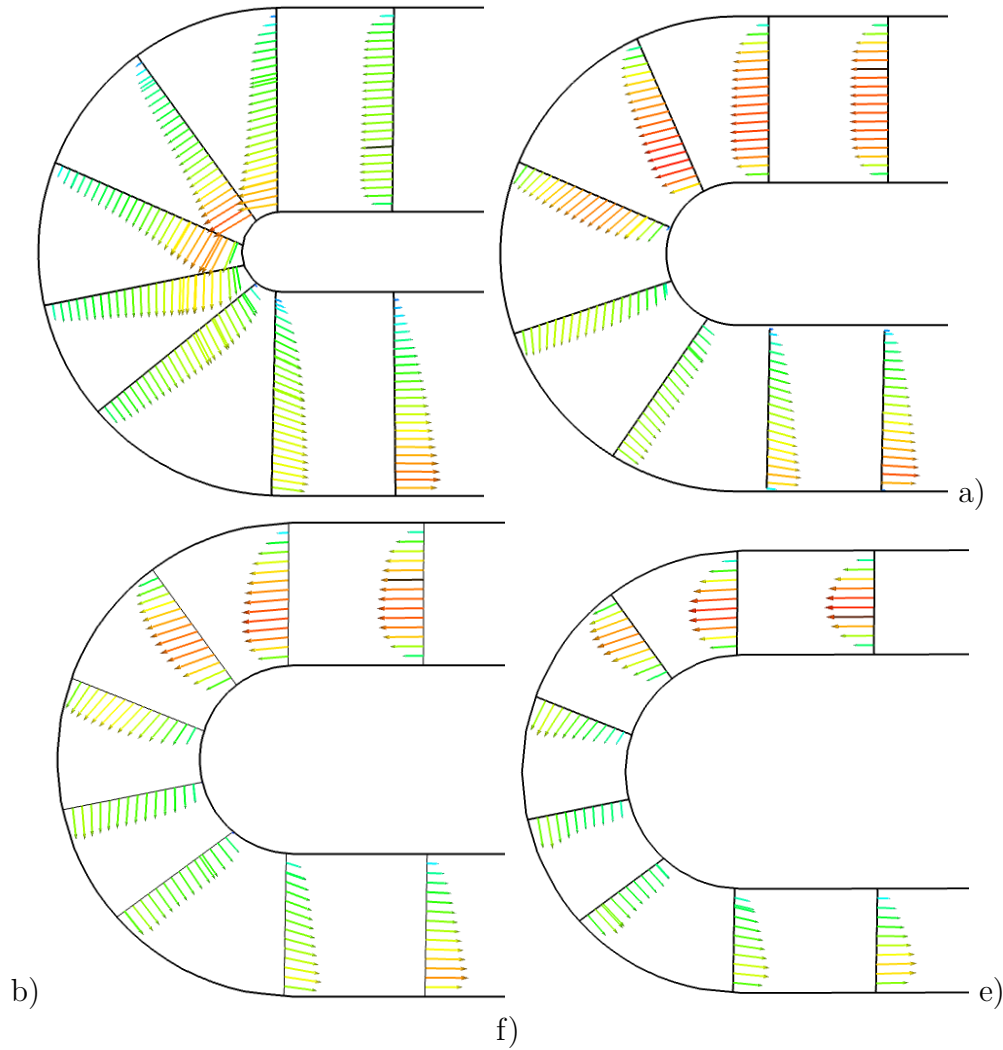
Figure 5.7: Velocity profile close to the bend for various aspect ratio cases. a) A1, b) A2, c) A3, d) A4.

Figure 5.9 shows temperature contours on the surface of the cooling plate. There were seven bends in the coolant channel between the inlet and the outlet, and the outline of the serpentine channel is shown in the figure. Temperature distributions on the plate surface displays a significant level of non-uniformity. Temperature hot spots are clearly seen around the outlet of the coolant channel, and the size of high temperature areas increases as the aspect ratio decreases due to a smaller contact area. Figures 5.9a and 5.9b show good temperature uniformity on the cooling plate surface with low maximum temperatures whilst a large area of hot temperature is observed for small A_R values (Figures 5.9d, 5.9e and 5.9f).
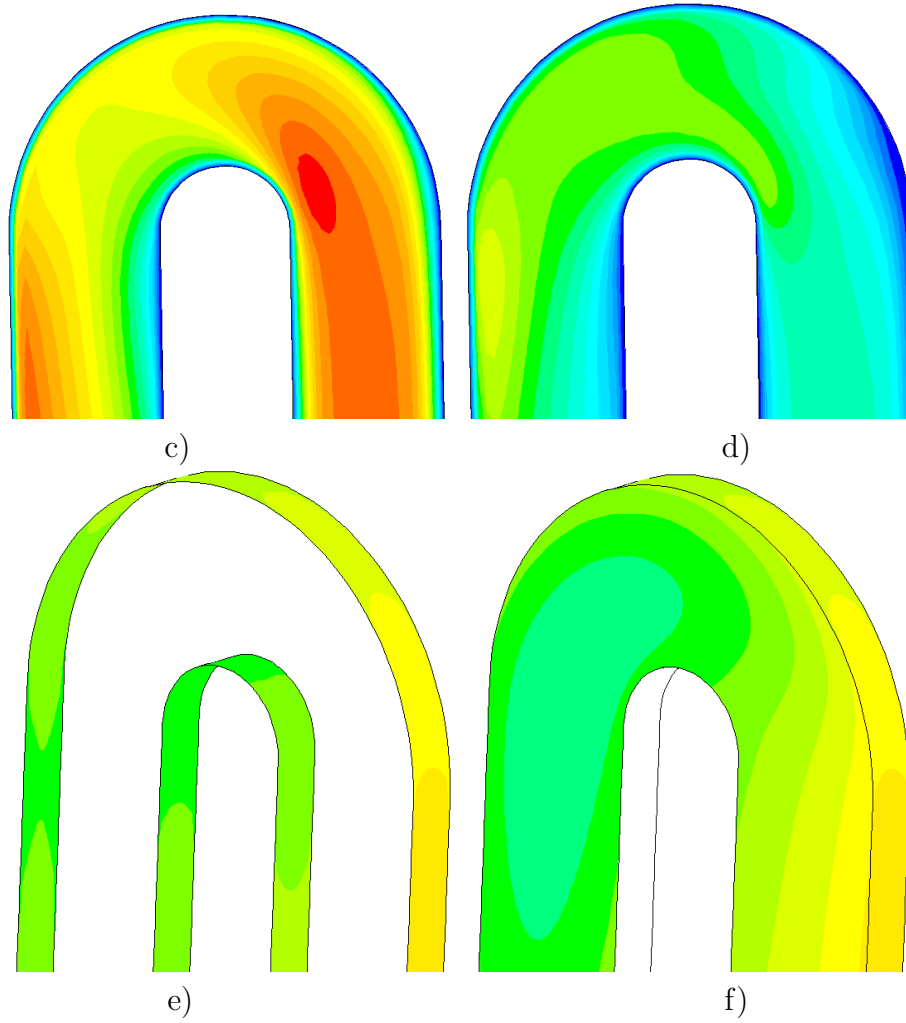
Figure 5.8: Coolant channel flow patterns for case C2. The flow direction is anti-clockwise. a) velocity on the channel mid-plane, b) velocity near the channel wall, and c) and d) temperature contour plots on coolant channel walls. Contour plot legend: High (Red), Low (Blue)

Figure 5.10 shows the velocity and temperature fields in the coolant channel for the baseline (A2) case. Nusselt number distribution shows that heat transfer is significantly increased around the bend, and this is attributed to the enhanced mixing in the bend evident from helicity contours. From Figure 5.10, it is clearly seen that the serpentine coolant channel flow is fully developed from the second bend. The velocity field around the third bend is displayed in Figure 5.11 together with the skin friction (C_f) and heat transfer coefficient (h_l) distributions on the channel wall. From the velocity contour plot in Figure 5.11, the local acceleration
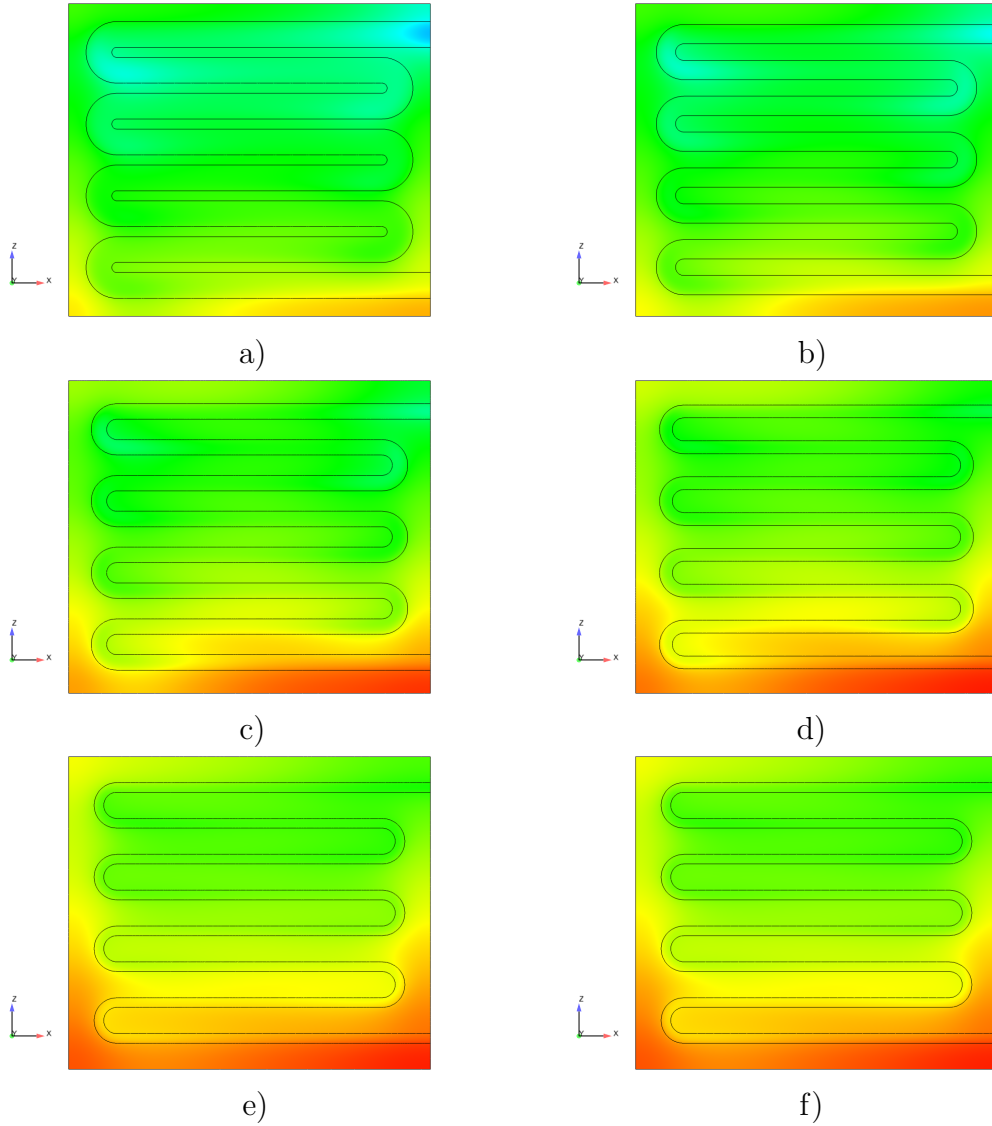
Figure 5.9: Wall temperature contours for different aspect ratios. a) A1, b) A2, c) A3, d) A4, e) A5, and f) A6. Contour plot legend: High (Red), Low (Blue)

and deceleration cased by the U-bend are clearly seen on the channel mid-plane. As the coolant flow passes the bend, the flow in the mid-plane is decelerated in the bend while the velocity near the channel wall is significantly increased, resulting in a high C_f shown in Figure 5.11c. The highest C_f is observed just downstream the end of the bend ($\phi = 180$) on the side wall as well as on the outer wall. The high C_f region also has high heat transfer coefficients (Figure 5.11d), and there is a good correlation between C_f and h_l in the bend.
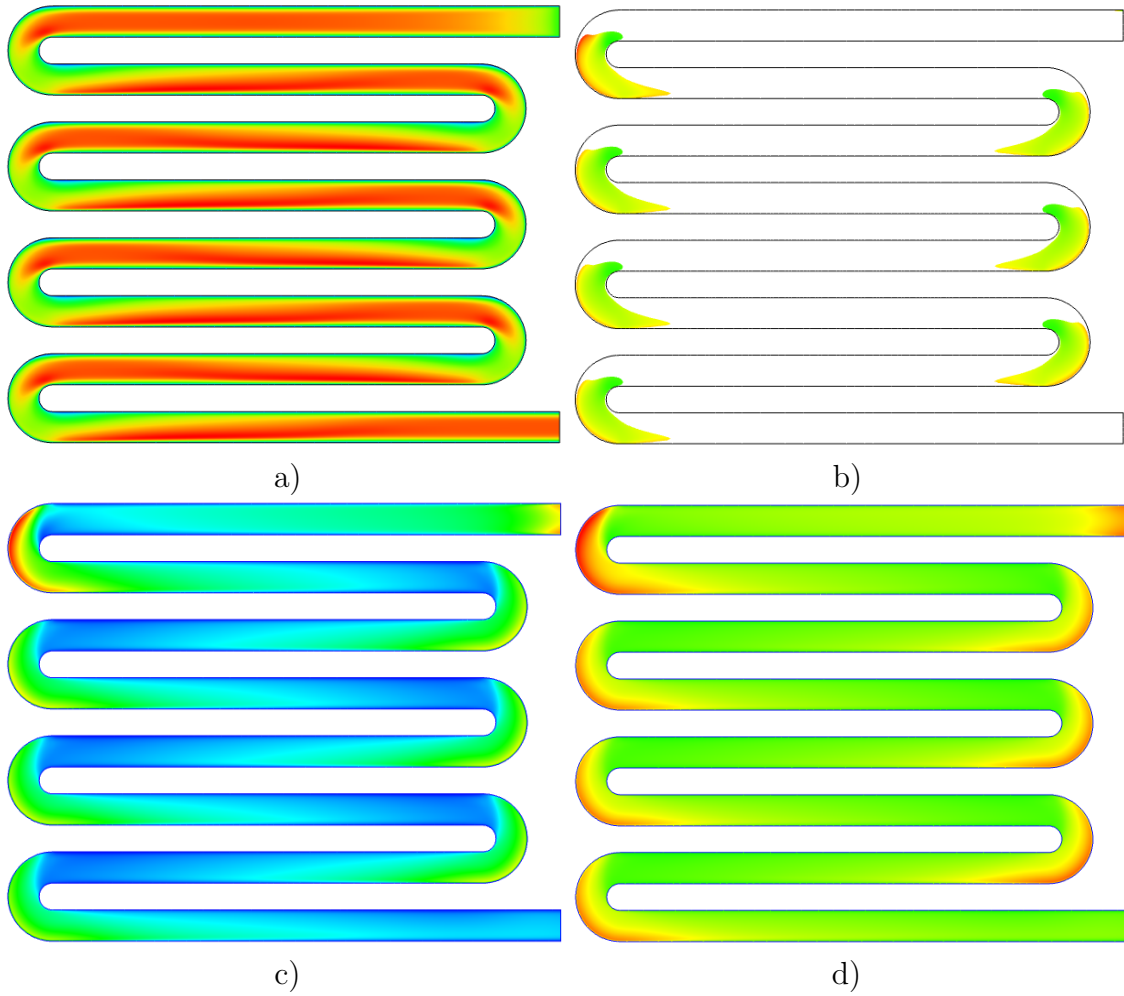
Figure 5.10: Case A2. a) Velocity contours at coolant channel midplane, b) Iso surface contours with Max skin friction, c) Channel Nusselt number contour plot, and d) Channel wall heat flux contour. Contour plot legend: High (Red), Low (Blue)

The results along the channel centreline (s) are shown in Figure 5.12, starting from the channel inlet ($s = 0$) to the outlet ($s = 1$). In Figure 5.12a, the coolant temperature increases gradually as the flow moves downstream. The temperature increase between two consecutive bends is about 0.4 °C. It is interesting to note that there is a sudden decrease in the bulk mean fluid temperature T_m as the flow passes bends; the amount of temperature decrease remains the same apart from the first bend, suggesting that the serpentine coolant channel flow is fully developed and therefore can be considered as a periodic flow from the second bend. For the large

a)   b)

c)   d)
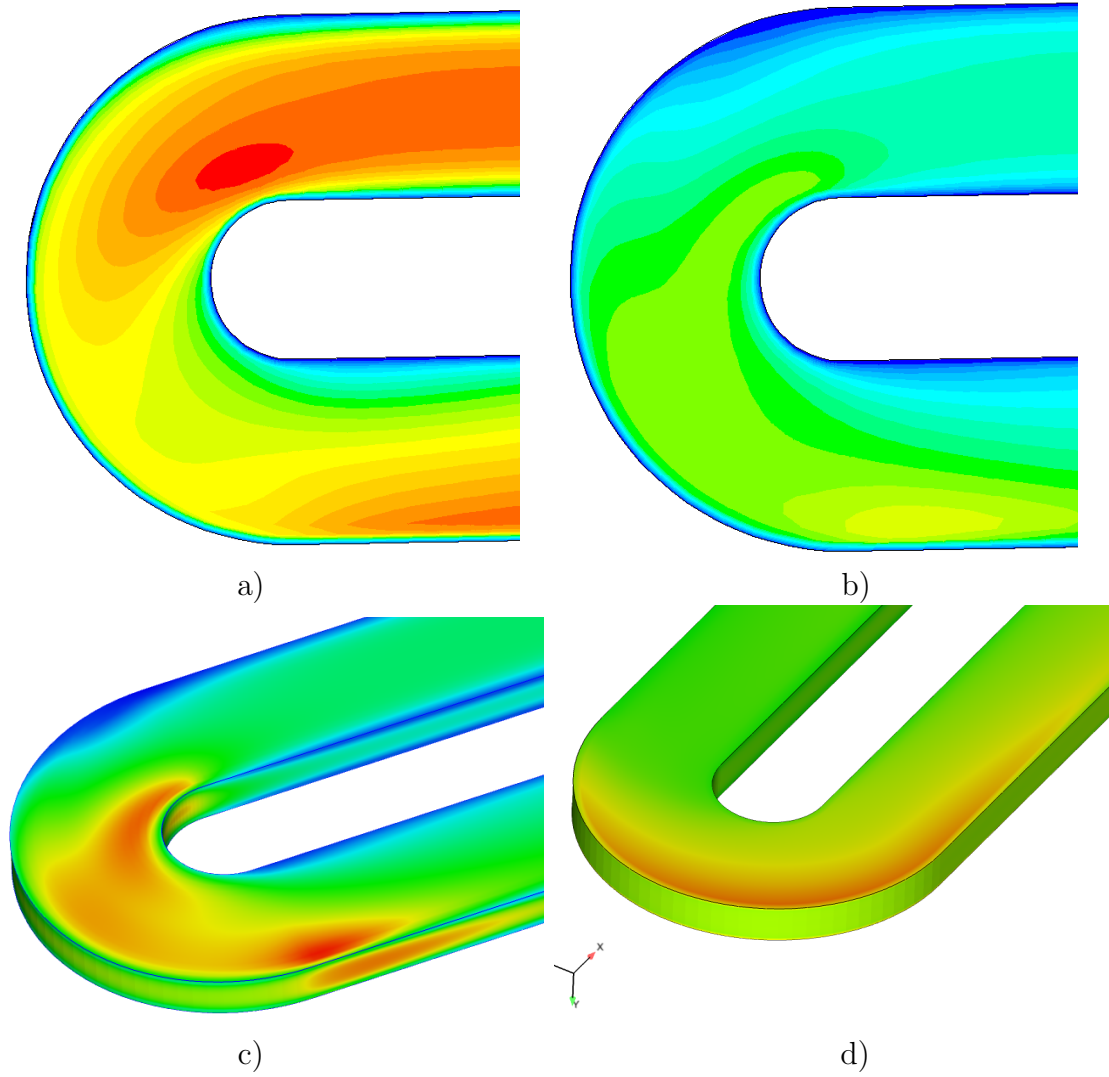
Figure 5.11: Around the third bend for the baseline (A2) case. The flow direction is anticlockwise. a) Velocity on the channel mid-plane, b) velocity near the channel wall, c) skin friction, and d) heat transfer contours on the channel wall. Contour plot legend: High (Red), Low (Blue)

A_R case (A1), the effect of the bend is quite small, and T_m increases almost linearly. The channel wall temperature T_w has a local maximum between the bends, and decreases significantly around the bend due to the enhanced heat transfer, having a local minimum just after the bend. The locations for the start and end of the third bend are indicated in Figure 5.12d. Enhanced heat transfer around the bends is also clearly seen from the heat transfer coefficient (h_l) and the Nusselt number. Nu begins to increases just before the bend ($\phi = 0$), and has a local maximum at the
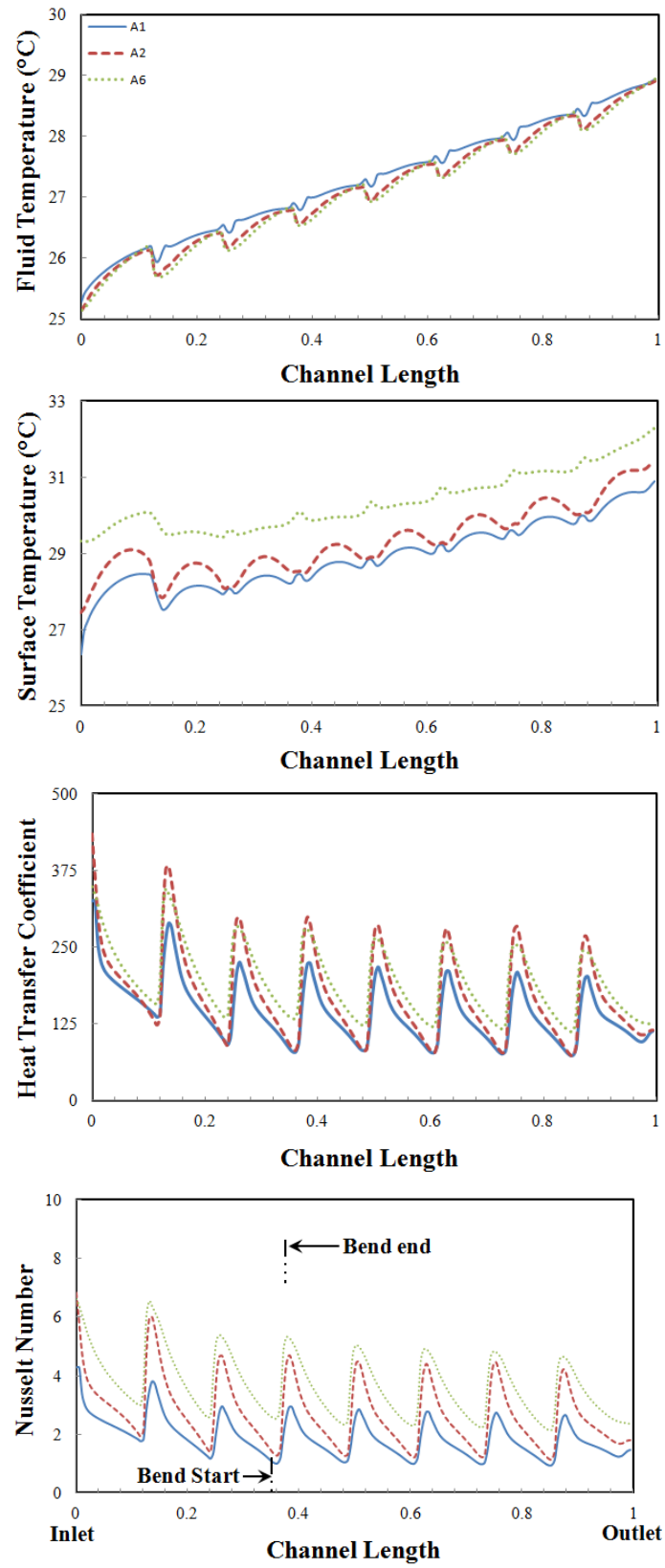
Figure 5.12: Aspect ratio cases. a) T_m, b) T_w, c) h, and d) Nu. The locations for the start and end of the third bend are indicated.

end of the bend ($\phi = 180$). The sudden increase in Nu number observed in Figure 5.12d is attributed to the enhanced heat transfer in the outer region of the bends shown in Figure 5.11d.

The effect of the aspect ratio on thermo-hydraulic properties can be seen from Figure 5.13. The pressure drop Δp between the inlet and the outlet rises as the aspect ratio increases. Compared to the baseline case, Δp for case A1 is about 50% larger. The variation in the Re number shown in Figure 5.13b is due to the changes in the hydraulic diameter (see Table 5.3), with the minimum Re number for the largest A_R. As expected, Δp is inversely proportional to D_h. One of the key parameters in battery thermal management system is the temperature variation on the cooling plate surface. The maximum, minimum, and average temperatures (T_{max}, T_{min}, and T_{avg}) on the cooling plate surface are measured to assess the temperature variation. Figure 5.13c shows that all three temperatures rise as the channel aspect ratio decreases, indicating less efficient heat removal from the coolant channel. It is found that aspect ratio has a strong effect on the surface temperature variation; T_{min} rises faster than T_{max} for small A_R cases.

The temperature uniformity on the cooling plate surface is measured as the rms temperature fluctuation. Figure 5.13d shows that large A_R cases have better temperature uniformity as suggested in Figure 5.9. An important requirement of battery cooling is to have a small temperature variation across the battery surface with a low T_{max}, combined with a lower coolant pressure drop. Based on the pressure drop and the temperature uniformity, case A2 appears to be most attractive among all A_R cases. The large A_R case (A1) would have too high a penalty on pressure drop, and the small A_R cases (A3, A4, A5 and A6) would allow too much temperature variation on the surface. In the following sections, case A2 is further investigated.
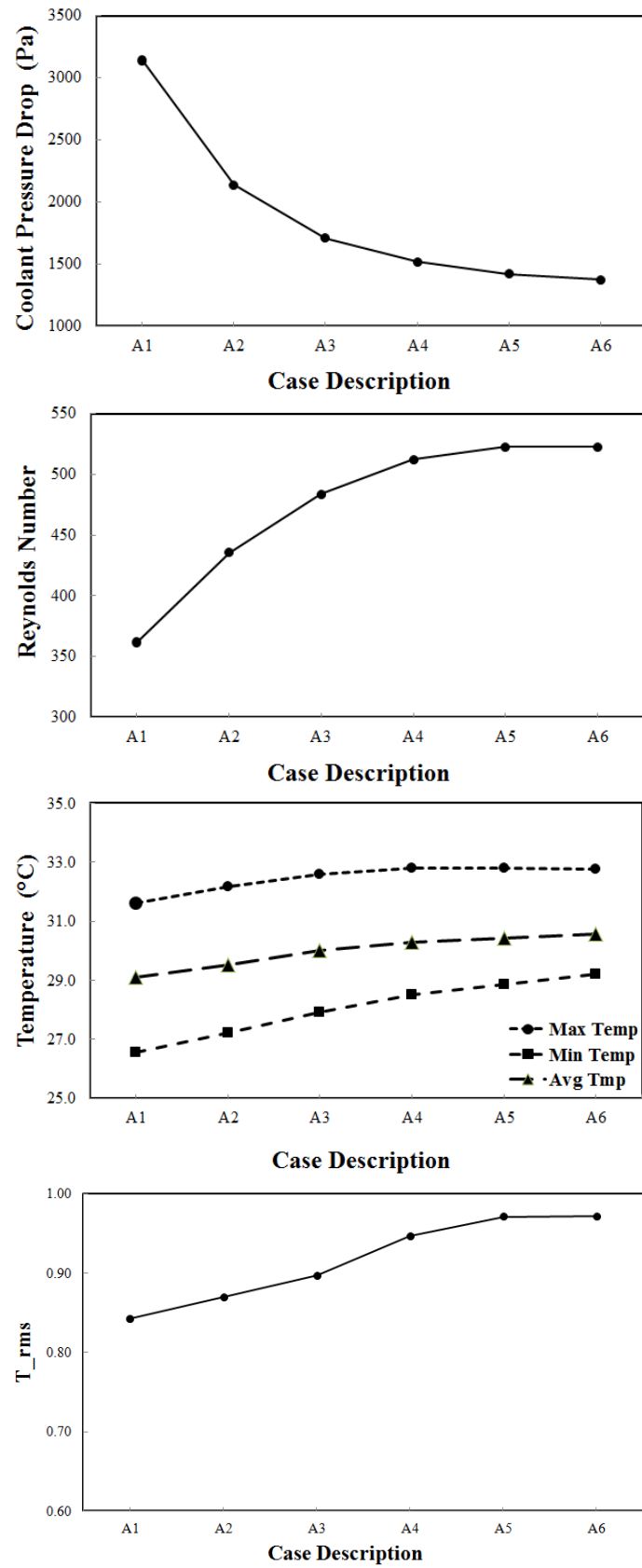
Figure 5.13: Aspect ratio cases. a) Δp, b) Re, c) T_{max}, T_{min}, T_{avg}, and d) temperature uniformity index.
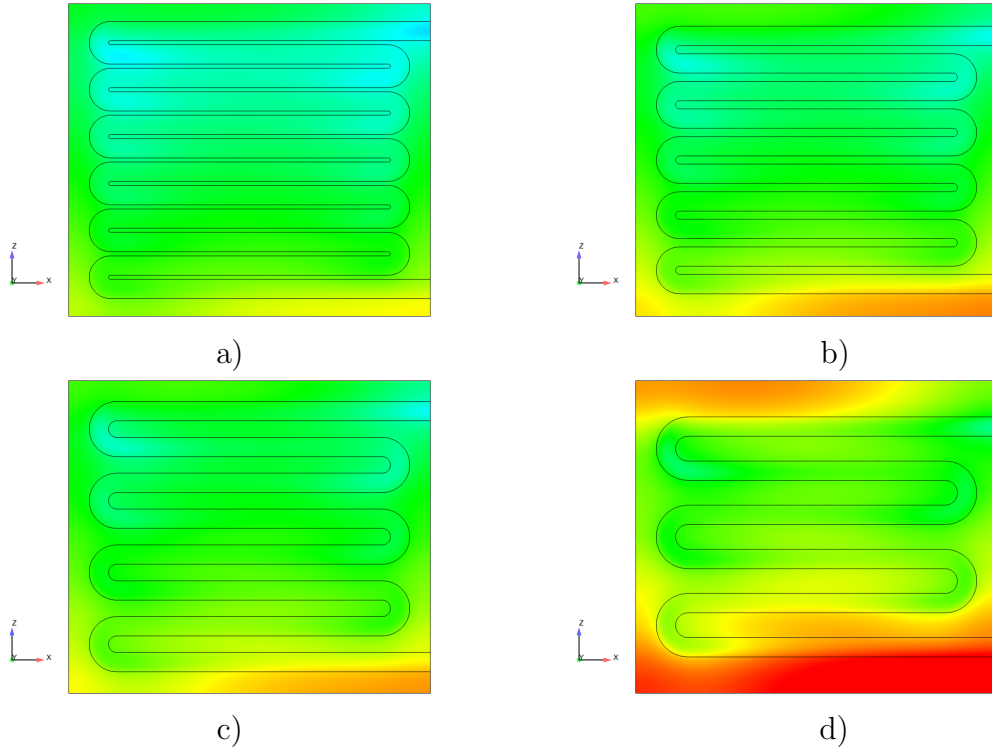
Figure 5.14: Average wall temperature contours for radius of curvature cases. a) C1, b) C2, c) C3, and d) C4. Contour plot legend: High (Red), Low (Blue)

5.4.3   Radius of curvature

Next, the effect of the radius of curvature (r_c) of the bend on the cooling plate conjugate heat transfer was investigated. The radius of curvature was changed from the baseline case while all other parameters remained the same. As $g = 2r_c$, the radius of curvature determines the gap between the coolant channels, and hence the number of bends in the coolant channel. Four different r_c values were considered, corresponding to 5, 7, 9, and 11 bends. Details are shown in Table 5.4. Please note that case C3 is identical to the baseline case (A2). Figure 5.14 shows temperature contours on the cooling plate surface for four r_c cases. It can be clearly seen from the figure that the cooling plate surface temperature variation is significantly affected by the radius of curvature. For small r_c cases, the surface temperature exhibits relatively small variation, with a lower T_{max}. This is mainly attributed to the fact that a small r_c case has a large projection area on the cooling

plate; the projection area is roughly proportional to the number of bends. Details are given in Section . The temperature uniformity on the cooling plate surface deteriorates as r_c increases; areas of high temperature appear for the largest r_c case, in particular near the channel outlet (Figure 5.14d). The effect of r_c on thermo-hydraulic properties of coolant channel can be seen in Figure 5.15. As expected, the pressure drop increases as the radius of curvature decreases and the number of bends increases. As mentioned earlier, a smaller r_c case contains a larger number of bends and a larger projection area, demanding a higher pumping power. All three wall temperatures (T_{max}, T_{min}, and T_{avg}) increase with r_c. The configuration with the largest r_c value has the highest T_{max} and T_{rms}. Considering both the pressure penalty and heat transfer efficiency, case C3 appears to be the most attractive. The small r_c cases (C1 and C2) would have too high a pressure penalty, and the large r_c case (C4) would allow too much temperature variation on the cooling plate surface.

5.4.4   Mass flow rate

Finally, the effect of the mass flow rate ($\dot{m}$) on various thermo-hydraulic properties was examined. The baseline case was chosen here. Figure 5.16 shows the variations of different thermo-fluid parameters along the centerline of the coolant channel. As expected, both the coolant temperature (T_m) and the channel wall temperature (T_w) decrease with the flow rate. However, the overall trend of T_m and T_w are quite similar for all cases, suggesting the underlying thermo-fluid characteristics remain unchanged. A sudden decrease followed by a gradual increase in T_m denotes the location of the bends. The variation in T_w at the bend location is smaller for higher Re numbers. The heat transfer coefficient and Nu are shown in Figures 5.16c and 5.16d. The Re number effect is discernible, albeit small; large Nu numbers are observed for high Re flows, but the effect is mainly confined to the bend region. Figure 5.17 shows the bulk mean fluid temperature at various coolant flow rates.
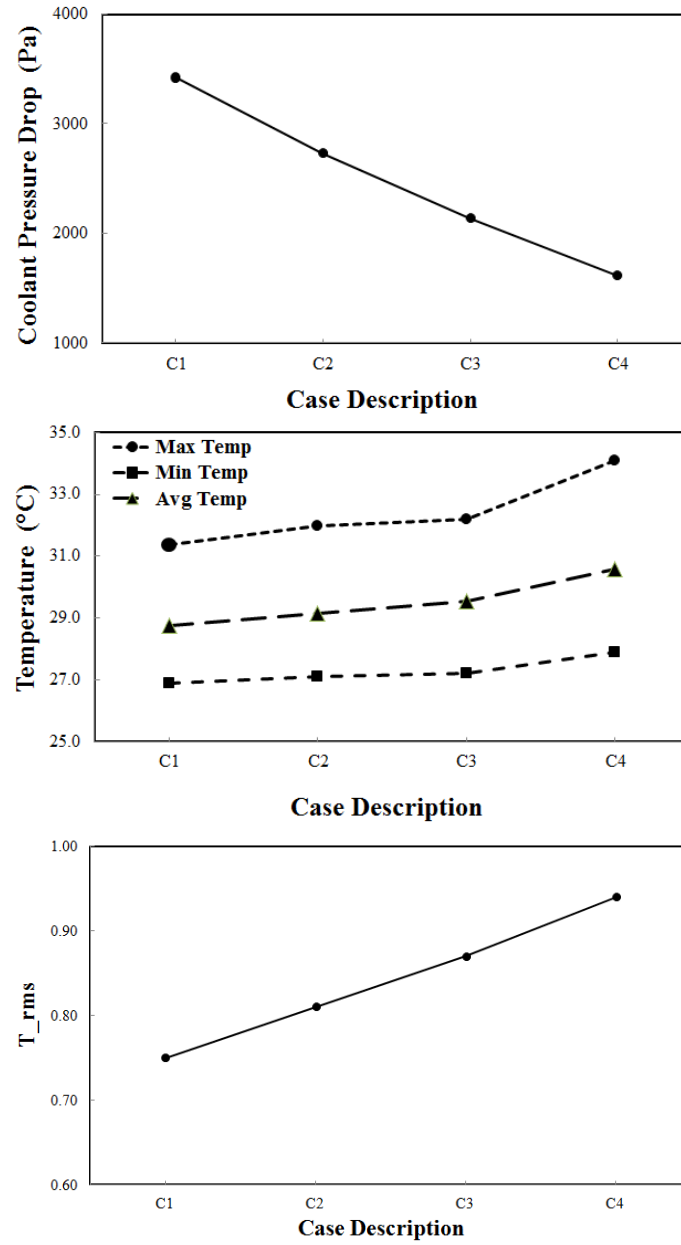
Figure 5.15: Radius of curvature cases. a) Δp, b) T_{max}, T_{min}, T_{avg}, and c) temperature uniformity.
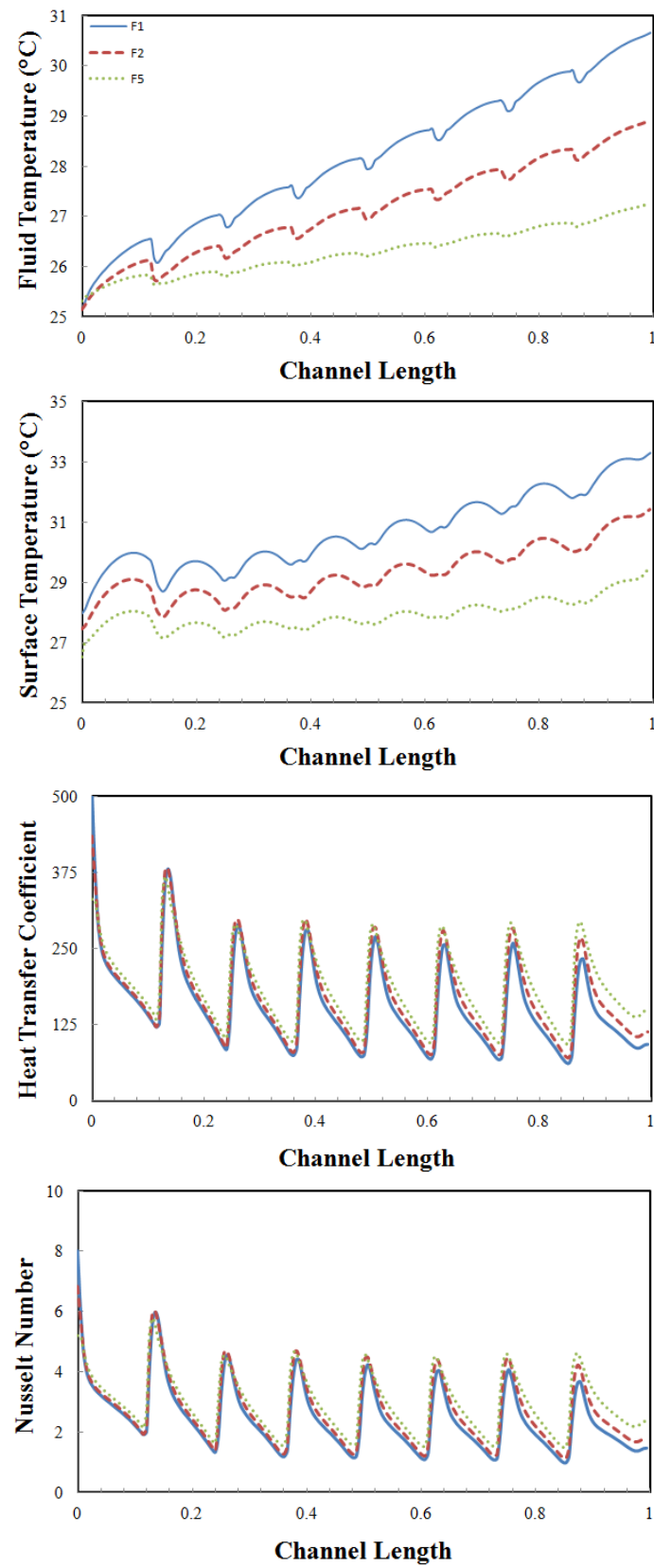
Figure 5.16: Mass flow rate cases. a) T_m, b) T_w, c) h, and d) Nu.
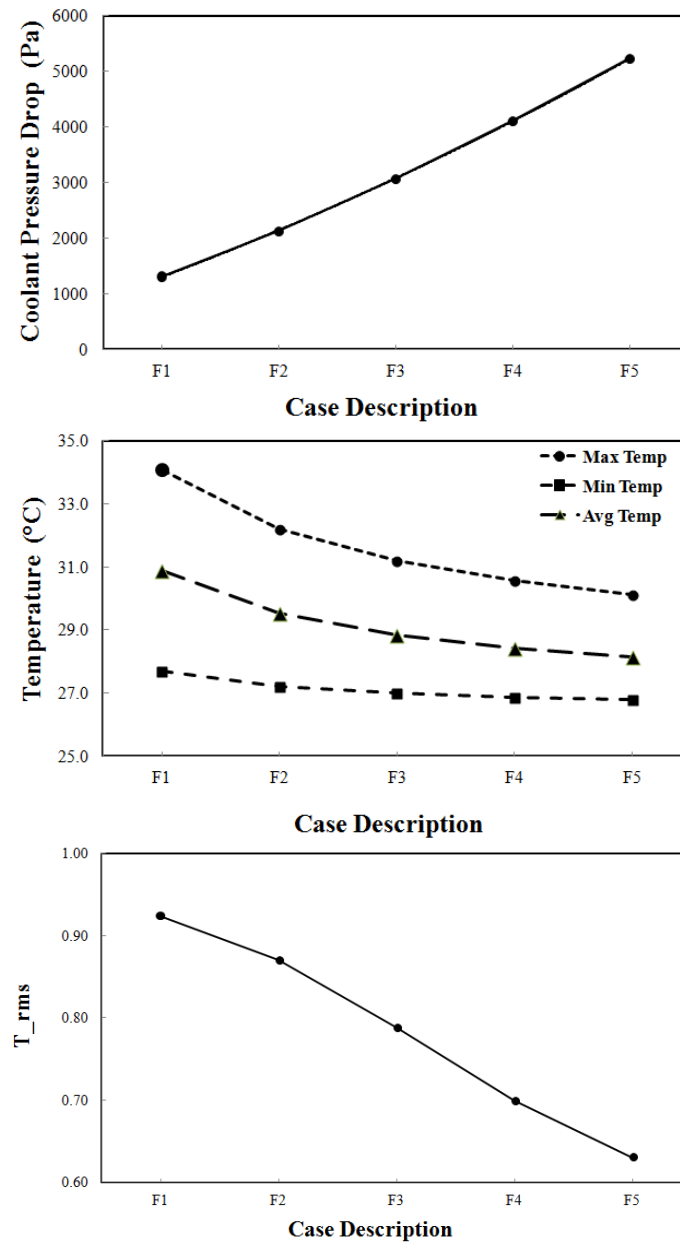
Figure 5.17: Mass flow rate cases. a) Δp, b) T_{max}, T_{min}, T_{avg}, and c) temperature uniformity.
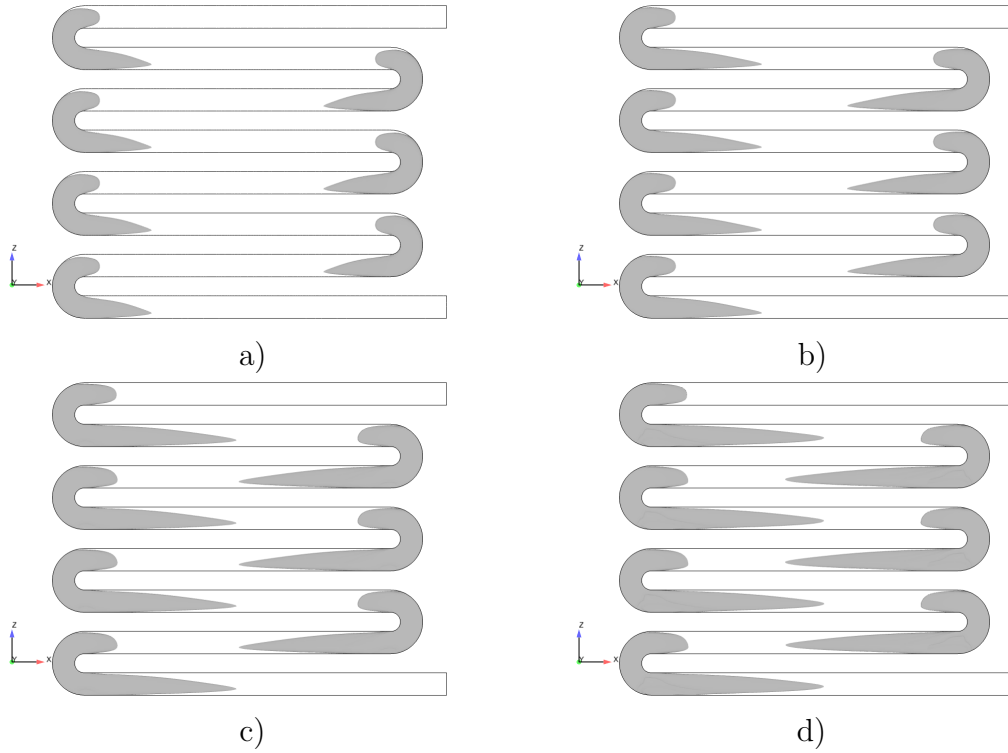
Figure 5.18: Coolant channel helicity patterns for various mass flow rate cases with a contour value of 1.7. a) M1, b) M2, c) M3, and d) M4.

The mass flow rate has clearly improved the temperature uniformity, so that the temperature difference is reduced from 4°C for case F1 to 0.5°C for case F5. The largest Re number flow still remains laminar, supporting the earlier observation in Figure 5.16d that the main heat transfer characteristics are unchanged. The pressure drop increases sharply with the Re number. The rate of increase is larger than expected from the straight channel case, suggesting that the Re number effect may be more prominent in the bend region. This point is further studied in terms of the helicity [128] in Figure 5.18. A normalised helicity is used to detect and visualise vortex cores [129]:

$$H_n = \frac{\overrightarrow{u} \cdot \overrightarrow{\omega}}{|\overrightarrow{u}||\overrightarrow{\omega}|}, \tag{5.19}$$

where $\overrightarrow{u}$ and $\overrightarrow{\omega}$ are velocity and vorticity vectors, respectively. Figure 5.18 shows that there is a enhanced mixing at the bends resulting from the formation of Dean

vortices. It can be seen that the iso-surface volume increases with the Re number, indicating stronger mixing and enhanced heat transfer as shown from the temperature and Nusselt number profiles in Figure 5.16.

Considering the pressure drop and the surface temperaure in Figure 5.17, case F2 with $Re = 435$ is found to be the optimum case where the pressure penalty for the heat transfer gain is small. This flow rate (case F2) also results in the right level of temperature variation (uniformity index).

5.5   Conclusions

Conjugate laminar heat transfer simulations have been performed for a battery cooling plate with serpentine channels of a rectangular cross section. In this study, the effect of the channel aspect ratio and the radius of curvature on the thermohydraulic performance of serpentine coolant channels was studied. Constant heat flux was applied on the surface of the cooling plate to consider the heat generation from a battery module. Key performance indicators such as temperature uniformity and maximum temperature were evaluated at several Re numbers with a view to maximising the heat transfer while minimising the pressure drop of the serpentine channels. It is found that the aspect ratio had a strong effect on the surface temperature variation. Temperature uniformity on the cooling plate surface was improved for a small radius of curvature although the pressure drop penalty was high. The temperature hot spots were clearly seen on the cooling plate surface around the outlet of the serpentine channel, and the size of the temperature hot spots increased as the aspect ratio decreased and the radius of curvature increased. In this study, the potential of conjugate heat transfer simulations in battery thermal management has been demonstrated.

6

Conclusion

6.1 Conclusion

Two key aspects of advanced thermal management were studied in this study. This includes numerical modeling of heat generated from Li-ion cells and laminar conjugate heat transfer from the cell through a cooling plate with rectangular serpentine channels. In addition to a laminar flow regime, heat transfer in turbulent flow is also studied to benchmark the capabilities of different RANS and LES models.

The numerical study of heat generated by Li-ion cells has been covered in Chap-

ter 4. A fully coupled, new three-dimensional electro-thermal cell model has been proposed and implemented based on finite volume method has been developed. This model is capable of predicting the electrical and thermal behavior of a Li-ion polymer cell. Various performance experiments have been done on different types and formats of cells to gain an initial understanding of the behavior of Li-ion cells. A Li-ion pouch cell was characterised electro-thermally in detail to provide data for the cell model development. The characterisation tests were carried out in a thermally controlled environment inside a climatic chamber. The data for discharge dependency of the cell on current and temperature for a known load cycle was also generated for model validation. The electro-thermal model was seen to predict the cell temperature and voltage magnitudes accurately for the test load cycle. The electro-thermal model was then used to predict the cell level performance for two real world vehicle drive cycles, the first one reflected a mild EV operating condition, and the other a more severe operating condition. It is clearly seen that during the severe real world drive cycle there is a substantial increase in cell temperatures. It is clear that effective thermal management is required in such instances to ensure optimal cell performance. This understanding is key to further thermal management study and such insights along with other information such as surface temperature variation on cell surface would play a key role resulting in better design of thermal management systems. In a separate study, the proposed electro-thermal cell model is being implemented to predict cell thermal performance estimations in battery management system and vehicle drive cycle modelling applications. The current work is also being extended to model the cell electrical dynamics and their effect on the voltage and temperature.

Laminar conjugate heat transfer simulation of a battery cooling plate with rectangular serpentine channels has been performed in Chapter 5. This study assesses the effects of the channel aspect ration and radius of curvature on the thermo-hydraulic performance of the channels. A constant heat flux was applied to the

cooling plate faces to reflect the a battery module heat rejection for a EV application. Thermal management performance indicators such as temperature uniformity, maximum temperature were monitored at several Re numbers with a view to maximising the heat transfer while minimising the pressure drop of the serpentine channels. It is clearly evident that aspect ratio had a strong impact on the surface temperature. With reduction in radius of curvature the temperature uniformity increased although the pressure penalty was high. The temperature hot spots were clearly seen around the cooling plate surface close to the outlet of the serpentine channel. The size of the temperature hot spot increased as the aspect ratio decreased and radius of curvature increased. Ability to predict the temperature uniformity and maximum temperature are key to thermal management studies and the conjugate heat transfer simulations here have clearly demonstrated its potential use in such applications.

Heat transfer in turbulent flow applications to benchmark the capabilities of different RANS and LES models has been covered in Appendix. Numerical simulations of a triple jet flow were performed to assess the capability and accuracy of LES and RANS models. Various grid resolutions were used, the fine grid LES, which used a modest number of grid points, showed good agreement with the available experimental data. The temperature fluctuations were accurately predcited by the LES. This study clearly demonstrate the capability and potential of LES for heat transfer studies. RANS simulations with two turbulence models were also conducted along with LES. The SA and realizable $k - \varepsilon$ turbulence models predicted the mean flow and thermal fields reasonably well, although an over-prediction of the maximum values was observed with the realizable $k - \varepsilon$ turbulence model. However, the prediction of the temperature fluctuations by the two RANS models was very poor, indicating that LES not RANS is the appropriate tool to predict the coolant temperature fluctuations associated with high-Reynolds number turbulent thermal mixing.

Appendices

A

Triple jet simulations

Finally, in addition to the laminar heat transfer, a turbulent heat transfer to benchmark the capabilities of different RANS and LES models in a triple jet is studied with a view to apply the understanding to a high discharge battery thermal management application. Non-isothermal turbulent jets generate an intense mixing of different temperature fluids before they develop fully further downstream, resulting in strong temperature variations in time. Thermal striping refers to these temperature fluctuations that are observed at the interface between the two non-isothermal jets. The thermal striping occurs in many engineering applications including liquid metal cooled fast reactors (LMFR), where severe temperature fluctuations occur

from the mixing of high and low temperature sodium flowing across the reactor core subassemblies. In sodium-cooled faster reactor, a typical temperature difference between the flow streams emanating from the fuel subassemblies and the control subassemblies is of the order of 100°C [130]. The large temperature fluctuations are a primary cause for thermal stresses in the LMFR, and can cause thermal fatigue failure. The thermal striping is one of the major factors to consider in the design and life management of components of LMFR, and understanding this phenomenon is important in maintaining high safety standards in LMFR. An accurate heat transfer analysis is required to find its effects on the solid boundary where the fluid temperature changes rapidly and cyclically.

A.1   Introduction

Thermal striping has been studied experimentally with water, air and sodium as a working fluid. Wakamatsu *et al.* [131] carried out an experiment to understand the thermal striping observed in a faster reactor. The experiment was designed to reproduce a similar condition in the upper plenum of an LMFR. Hot and cold water was injected through two rectangular nozzles, and a solid plate was placed at a small distance above the nozzles. As the two parallel jets impinged on the solid plate, the incomplete mixing of hot and cold jets of fluid gave rise to large temperature fluctuations. Tenchine and co-workers [132, 133, 134] used co-axial jets of air, water and sodium in their experiments. They found that the air tests can be used to predict the thermal fluctuation behaviour in the sodium reactor [133]. A parallel triple jet configuration has also been used for thermal striping studies [135, 136, 137]. Kimura and co-workers [135, 136] used a cold fluid in the centre and hot fluid on both sides to model the configuration of the reactor core outlet of control rods surrounded with fuel subassemblies. They used both water and sodium as a working fluid. Recently, Nam and Kim [137] used an air triple jet as a mockup of the

outlet of the LMNR fuel subassemblies. A large thermal fluctuations were measured in their experiment with various combinations of inlet velocity and temperature.

There have been a continual effort to predict the temperature fluctuations in thermal striping using numerical simulations. Many variants of turbulence models have been used in Reynolds-Averaged Navier-Stokes (RANS) simulations with some varying successes in terms of predicting mean velocity and thermal fields [138, 139, 140, 141]. Recently, Choi and Kim [142] performed numerical simulations of the triple jet experiments conducted by Nam and Kim [137]. They found that only the $\overline{v^2} - f$ model [143] was able to predict the temperature fluctuations, while other turbulence models resulted in a steady state flow. However, the amplitude of the fluctuation predicted was still significantly smaller than the experimental value; the $\overline{v^2} - f$ model predicted only a fraction of the amplitude of the temperature fluctuations observed in the experiment. None of the above RANS models were able to predict the correct level of temperature fluctuations observed in the experiments, which is the main cause of thermal striping fatigue damage in LMNR structures.

While RANS models are not able to predict the temperature fluctuations, a large eddy simulation (LES) technique has been used in limited areas of nuclear applications to investigate unsteady flow and thermal fluctuations. A few example of the use of large eddy simulations for calculating turbulent flows and heat transfer in the nuclear field are given in Grötzbach and Wörner [144] and Simoneau *et al*. [145]. The main objectives of this study were to assess the capability and accuracy of LES in the thermal striping study. To this end, unsteady numerical simulations were performed to predict the temperature fluctuations in a triple jet using LES. This is, to the authors' knowledge, the first LES study of the thermal striping in a triple jet. A detailed analysis of the flow and thermal fields was carried out and the results were compared with the available experimental data.
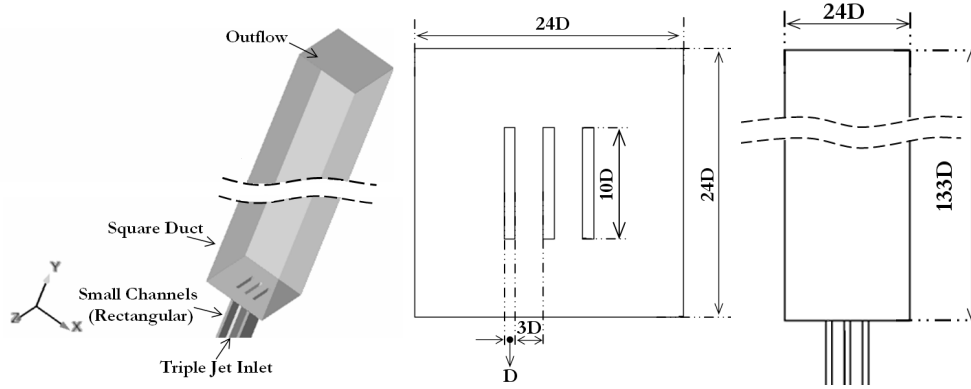
Figure A.1: a) A schematic diagram of triple jet geometry, b) top view, and c) side view.

A.2   Triple jet

In this study, a simplified triple jet geometry was considered for numerical simulations to model the thermal striping phenomenon in the outlet of the LMNR fuel subassemblies. The triple jet geometry was chosen to be the same as in the experiments of Nam and Kim [137]. This geometry is very similar to the model used in Kimura et al. [136]. The geometry of the triple jet and the computational domain are given in Figure A.1. The computational domain was composed of three inlet channels and a main square duct. The three channels were attached to the the base of the square duct, and the jets were issued from the nozzle. The experiment was designed to be two-dimensional by using nozzles with a rectangular cross section, and the previous numerical studies used a two-dimensional grid [141, 142]. However, we performed three-dimensional numerical simulations using LES technique in this study. All the geometric quantities were normalized with the nozzle width, D, equal to $0.015m$. The rectangular cross section of the nozzle was $D \times 10D$, and the corresponding hydrodynamic diameter is $D_h = 1.82D$. The gap between the neighbouring rectangular nozzles was $2.5D$, and this is the same as the value used in Kimura et al. [136]. The cross section of the square duct ($L \times L = 24D \times 24D$) was identical to the test section used in the experiments [137]. The main square

duct was $133D$ long, and this was long enough to capture the downstream behaviour of triple jet mixing.

The numerical simulations were concerned with the thermal mixing of an heated central jet (referred to as hot) in between two adjacent unheated jets at a lower temperature (referred to as cold). The inlet temperature of the hot jet was $T_h = 65°C$, while the two cold jets had a lower inlet temperature of $T_c = 41°C$; the discharged temperature difference between the hot and the cold jets was $\Delta T = 24°C$. The exit velocities at the three nozzles of the triple jet were all equal to $U_j = 10$ m/s. The Reynolds number based on the nozzle width and the nozzle exit velocity was about $Re_D = U_j D/\nu = 1 \times 10^4$.

A.3   Numerical simulation

A.3.1   Large eddy simulation and RANS models

In LES, the Smagorinsky-Lilly model was used to model the sub-grid scale (SGS) stress tensor ($\tau_{ij} = \overline{u_i u_j} - \overline{u}_i \overline{u}_j$). The SGS stress tensor is modelled as a linear function of the large-scale strain rate tensor, S_{ij}:

$$\tau_{ij} - \frac{1}{3}\delta_{ij}\tau_{kk} = -2\nu_{SGS}S_{ij}, \tag{A.1}$$

$$S_{ij} = \frac{1}{2}\left(\frac{\partial \overline{u}_i}{\partial x_j} + \frac{\partial \overline{u}_j}{\partial x_i}\right), \tag{A.2}$$

where $\nu_{SGS} = L_s^2 \left|\overline{S}\right|$ is the SGS viscosity, and $\left|\overline{S}\right| \equiv \sqrt{2\overline{S}_{ij}\overline{S}_{ij}}$. L_s is the length scale for SGS and defined as $L_s = \min\left(\kappa d, C_s \Delta\right)$, where the Kármán constant is $\kappa = 0.42$, and d is the distance to the closest wall. The value of the Smagorinsky constant is chosen as $C_s = 0.1$, which has been proven to yield good results for a wide range of flow conditions [122]. The grid filter width is defined as $\Delta = V^{1/3}$,

where V is the volume of the computational cell.

In addition to LES, two turbulence models were also considered in the present study. Spalart-Allmaras (SA) model [146] was chosen as a relatively simple one-equation model. The SA model solves the transport equation for the turbulent viscosity, $\bar{\nu}$:

$$\frac{\partial}{\partial t}(\rho\bar{\nu}) + \frac{\partial}{\partial x_i}(\rho\bar{\nu}u_i) = G_\nu + \frac{1}{\sigma_{\bar{\nu}}}\left[\frac{\partial}{\partial x_j}\left\{(\mu + \rho\bar{\nu})\frac{\partial\bar{\nu}}{\partial x_j}\right\} + C_{b2}\left(\frac{\partial\bar{\nu}}{\partial x_j}\right)^2\right] - Y_\nu + S_{\bar{\nu}}, \text{ (A.3)}$$

where G_ν is the production of turbulent viscosity and Y_ν is the destruction of turbulent viscosity that occurs in the near wall region due to wall blocking and viscous damping. $\sigma_{\bar{\nu}}$ and C_{b2} are constants, and $S_{\bar{\nu}}$ is a source term. As a second turbulence model, the realizable k-ε (RKE) model [147] was chosen in this study. The transport equations for k and ε are:

$$\frac{\partial}{\partial t}(\rho k) + \frac{\partial}{\partial x_j}(\rho k u_j) = \frac{\partial}{\partial x_j}\left[\left(\mu + \frac{\mu_t}{\sigma_k}\right)\frac{\partial k}{\partial x_j}\right] + G_k + G_b - \rho\varepsilon - Y_M + S_k, \qquad \text{(A.4)}$$

$$\frac{\partial}{\partial t}(\rho\varepsilon) + \frac{\partial}{\partial x_j}(\rho\varepsilon u_j) = \frac{\partial}{\partial x_j}\left[\left(\mu + \frac{\mu_t}{\sigma_\varepsilon}\right)\frac{\partial\varepsilon}{\partial x_j}\right] + \rho C_1 S\varepsilon - \rho C_2\frac{\varepsilon^2}{k + \sqrt{\nu\varepsilon}} + C_{1\varepsilon}\frac{\varepsilon}{k}C_{3\varepsilon}G_b + S_\varepsilon,$$

$$\text{(A.5)}$$

where G_k and G_b are the generation of turbulence kinetic energy due to the mean velocity gradients and due to buoyancy, respectively. $S = \sqrt{2S_{ij}S_{ij}}$, and S_k and S_ε are source terms. σ_k and σ_ε are turbulent Prandtl numbers for k and ε, respectively. A full description of those models can be found in Spalart and Allmaras [146] and Shih *et al.* [147].

A.4 Numerical Method

The above equations were solved using a second-order finite volume method and the PISO algorithm [148] for pressure-velocity coupling. Non-iterative time advancement (NITA) has been chosen for time control with a second order implicit scheme. For discretisation, a second-order accurate bounded central differencing scheme is used. The second-order upwind scheme was used for turbulence model equations. Simulations were carried out using a commercial CFD code, FLUENT [122]. The three-dimensional computer model was constructed with ICEM [123] software, and hexahedral computational grids were generated for the geometry shown in the Figure A.1.

A.4.1 Boundary Conditions

Simulation conditions were chosen to model the triple jet experiment of Nam and Kim [137] as close as possible. An inlet boundary condition was applied at the inlet of the three channels. The inlet temperatures of the hot and cold jets were at 65°C and 41°C, respectively. An outflow boundary condition was applied at the computational domain exit. No slip boundary conditions were applied along the side wall of the duct. It is worth noting that the previous RANS study [142] modelled only the core part of the test section using slip boundary conditions at the wall. Adiabatic boundary conditions were applied at solid walls. This thermal boundary condition is different from the experiment, where the duct was surrounded by air at room temperature. In this study, the ambient air surrounding the duct was not modelled, instead simple adiabatic conditions were used. The main interest in this study was to assess the capability of LES to predict the temperature fluctuations observed in thermal striping, and this difference in the thermal boundary condition did not affect the thermal striping phenomenon as the nozzles were located in the

middle of the duct (see Figure A.1). Because of this, the thermal field was compared with the experiment in the core region away from the side walls.

A.5   Results and discussion

Several simulations were performed on different computational grids and the results were compared with the experiment of Nam and Kim [137] to establish the accuracy of the present LES study. Three hexahedral grids were used with 1×10^6 (coarse), 2×10^6 (medium) and 4×10^6 (fine) grid points. The first grid point was located at $0.0067D$ in the fine grid, and the near-wall model was applied in the simulations.

First, instantaneous temperature from LES with three different resolutions is monitored and compared with the experiment. Figure A.3 shows the time history of temperature at a monitoring point ($x/D = 2$, $y/D = 15$ and $z/D = 0$). The monitoring point was located between the hot and cold jets in the mid plane. Note that the centres of the hot and cold jets were located at $x/D = 0$, and $x/D = 3.5$, respectively (see Figure A.1). The temperature was recorded at $1\ kHz$ in the LES, while the experimental data was measured at $4\ kHz$. The experimental data shown in Figure A.3(a) clearly demonstrates a highly oscillating nature of the temperature fluctuations. Please note that the oscillation in the experiment is not a sinusoidal oscillation but an irregular oscillation. The peak-to-peak temperature difference is about 20°C. This is very large temperature fluctuations, given that the discharge temperature difference between the hot and cold jets is $\Delta T = 24$°C.

Since the prediction of the thermal striping was the main objective of this study, instantaneous temperature fluctuations were monitored and compared with the experiment. Figure A.3 shows the time history of temperature at a monitoring point ($x/D = 2, y/D = 15$ and $z/D = 0$). The monitoring point was located between the hot and cold jets in the mid plane. Note that the centres of the hot and cold
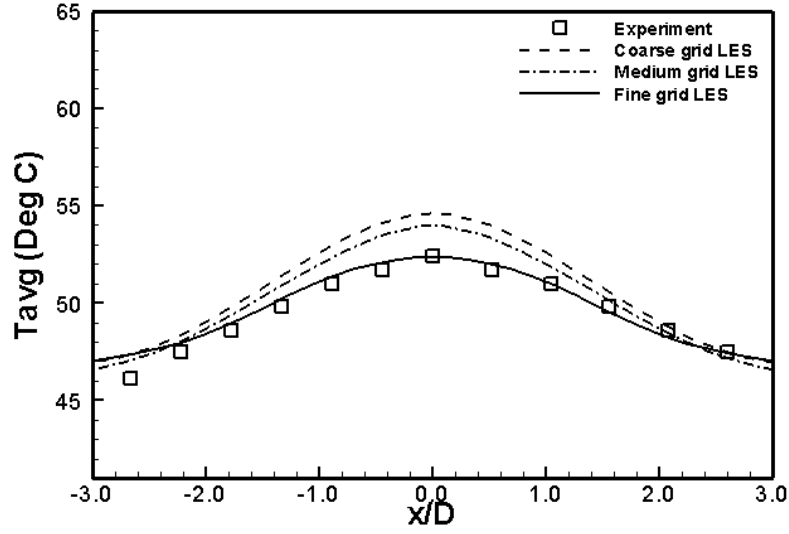
Figure A.2: Grid refinement tests. The time-averaged temperature profiles in the mid-span $(z/D = 0)$ at $y/D = 18$.

jets were located at $x/D = 0$, and $x/D = 3.5$, respectively. The temperature was recorded at $1kHz$ in the LES, while the experimental data was measured at $4kHz$. The experimental data shown in Figure A.3a clearly demonstrates a highly oscillating nature of the temperature fluctuations. Please note that the oscillation in the experiment is not a regular periodic oscillation. The peak-to-peak temperature difference was about 20°C. This is a very large temperature variation, given that the discharge temperature difference between the hot and cold jets was $\Delta T = 24$°C. The prediction of the correct amplitude of temperature fluctuations is very important in the thermal fatigue study [130], and also is the main reason for the use of LES in this study.

The temperature oscillation with three different grid resolutions are shown in Figure A.3. All three LES results predicted a high level of temperature fluctuations. Upon close inspection, however, some differences were found between the three LES results. The mean temperature in the coarse grid LES (Figure A.3d) was significantly higher than the experiment, resulting in a negative value of skewness.
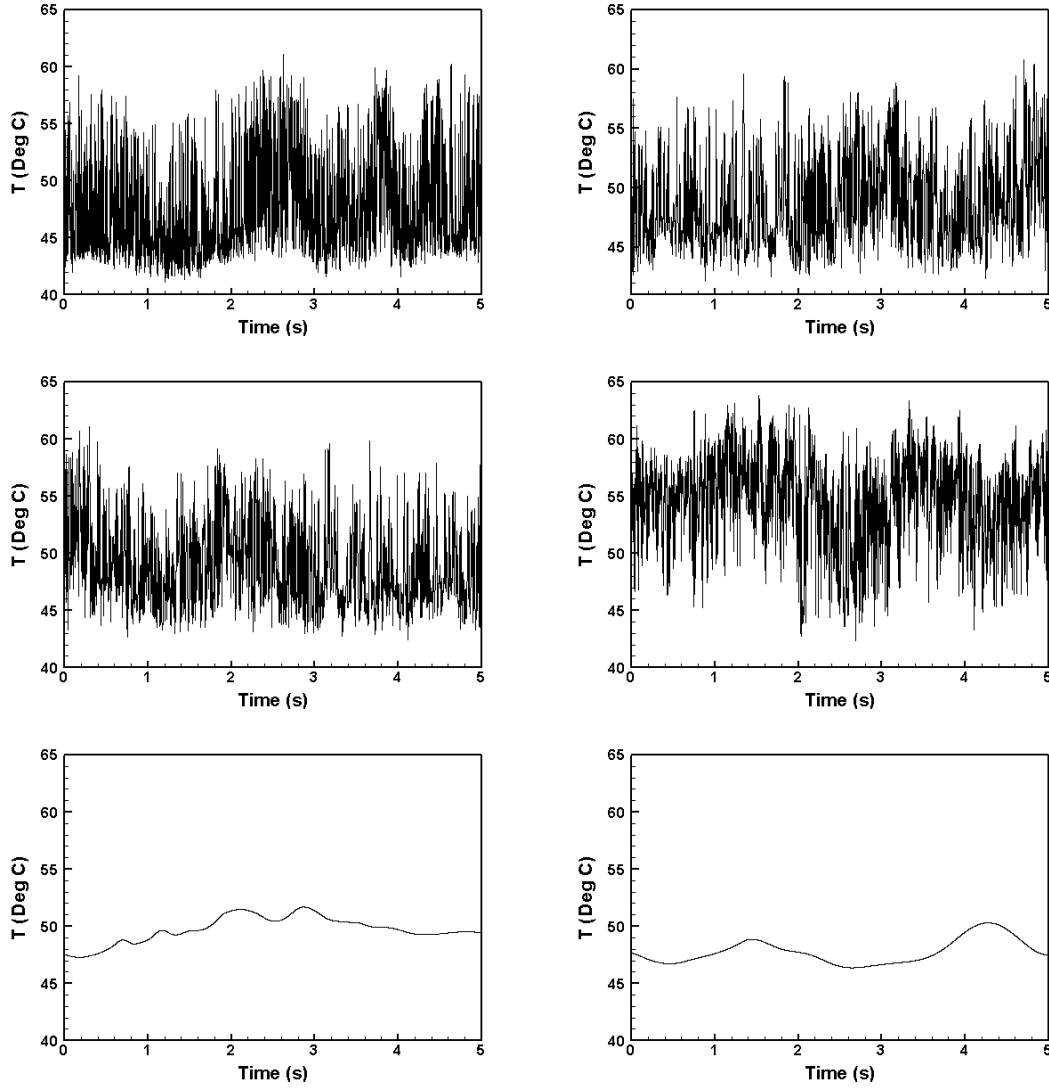
Figure A.3: Time history of instantaneous temperature at the measuring point $x/D = 2$, $y/D = 15$ and $z/D = 0$: a) experiment, b) fine grid LES, c) medium grid LES, d) coarse grid LES, e) SA model, and f) RNG $k - \varepsilon$ model.

The positive skewness of the fluctuation was correctly predicted in the medium grid LES (Figure A.3c), but the amplitude of temperature fluctuations was substantially larger than the experiment. The results improved further with the grid refinement, and the fine grid LES (Figure A.3b) compared well with the experiment in terms of the mean, rms, skewness, and kurtosis of fluctuations. The statistics are summarised in Table A.1. It is found from the grid refinement tests that the fine grid LES can be used to predict the amplitude of temperature fluctuations as well as the time-averaged thermal field observed in the experiment. In the following sections,

Table A.1: Statistical comparison of temperature data at the measuring point ($x/D = 2, y/D = 15$ and $z/D = 0$).

	Mean	RMS	Skewness	Kurtosis
Fine grid LES	48.5	3.4	0.74	2.9
Medium grid LES	49.1	4.6	0.72	2.6
Coarse grid LES	53.6	4.1	-0.41	2.5
Experiment [137]	46.5	3.3	0.97	3.2

the fine grid LES results will be further analysed to investigate the thermal and flow field of the triple jet.

A.5.1   Instantaneous temperature fluctuations

The time histories of temperature fluctuation predicted by the SA and realizable $k - \varepsilon$ turbulence models are also shown in Figure A.3. The incapability of the SA and realizable $k - \varepsilon$ turbulence models to predict the oscillatory behaviour associated with thermal striping is clearly evident. The two turbulence models produced some level of temperature variations but failed to predict the large amplitude temperature fluctuations observed in the experiment. These results are only marginally better than the two-layer [149] and SST $k - \omega$ [150] models used in Choi and Kim [142], where those turbulence models resulted in a steady state flow. It should be noted here that improved results were reported with a few turbulence models. High frequency thermal oscillations were predicted by the $\overline{v^2} - f$ model [143], albeit of smaller amplitudes [142]. Nishimura and Kimura [141] used a low Re number second-moment closure model to predict the low frequency periodic oscillation of a triple jet at $y/D = 5$, but the phase-averaged temperature profiles were over-predicted. The tendency of turbulence models to produce an over-simplified unsteady flow field was previous reported. For example, a laminar like vortex shedding was observed in a super-critical Re number circular cylinder flow with the standard $k - \varepsilon$ model [151].
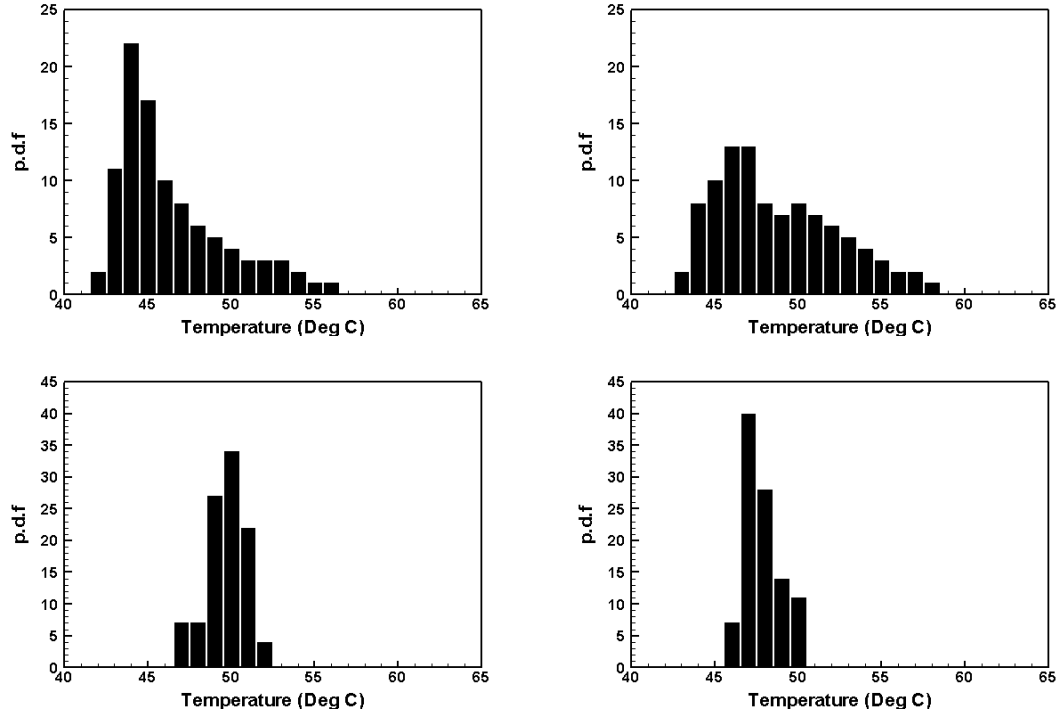
Figure A.4: Probability density functions (p.d.f.) of temperature fluctuations at the measuring point $x/D = 2$, $y/D = 15$ and $z/D = 0$: a) experiment, b) LES, c) SA model, and d) RNG $k - \varepsilon$ model.

On the other hand, the average, maximum and minimum temperatures predicted in the fine grid LES were in good agreement with the experiment, demonstrating that LES can be used to predict large amplitude thermal fluctuations in thermal striping.

The temperature fluctuations at the monitoring point were further analysed. The probability density functions (pdf) from the fine grid LES and the two turbulence models are plotted in Figure A.4. The pdf predicted in the LES was very similar to the one in the experiment. The wide temperature range between the low and high ends was correctly captured in the LES, and the positively skewed distribution shown in the experiment was also accurately predicted in LES, demonstrating that LES is capable of predicting the oscillatory behavior of the thermal striping observed in experiment. On the other hand, the SA and realizable $k - \varepsilon$ models could predict neither the temperature range nor the peak temperature observed in experiment. Instead, the turbulence models had narrow distributions, indicating the limitation
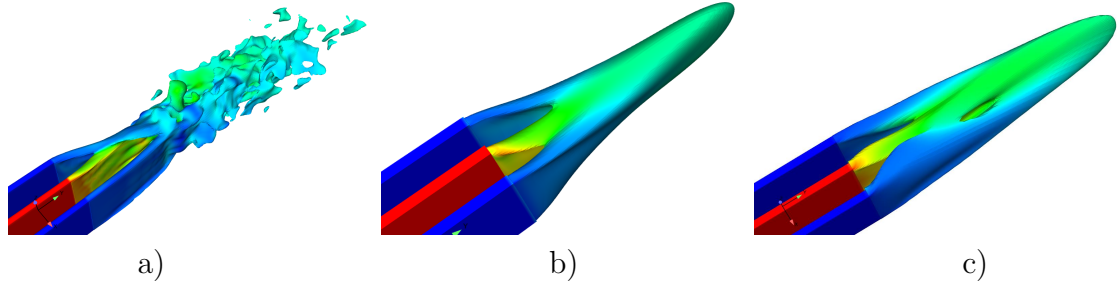
Figure A.5: The three-dimensional velocity contours coloured by temperature showing flow structure of the triple jet: a) LES, b) SA model, and c) RNG $k - \varepsilon$ model. White colour indicates high temperatures and black colour low temperatures. Contour plot legend: High (Red), Low (Blue)

of both RANS models to predict the frequency of temperature fluctuations.

A.5.2   Unsteady flow fields

Figure A.5 shows iso-surfaces of velocity from the LES and the turbulence models. The surfaces were colored by temperature. The unsteady, intermittent nature of flow field is clearly seen in the LES. The hot and cold fluid jets became unstable due to the Kelvin-Helmholtz instability, and interacted to form vortices that travelled downstream. In contrast, unsteady flow structures were missing in the flow field predicted by both turbulence models, again indicating the inability to predict the thermal striping phenomenon.

The instantaneous temperature field of the LES was further analysed. Several snapshots (24D×50D) of temperature in the mid-plane are shown in Figure A.6. The oscillatory behaviour of a triple jet was well captured in the LES. Similar unsteady flow patterns were observed in the experiments of thermal striping [135, 139]. As the jets were issued vertically from the nozzles, the shear layers started to oscillate due to the shear layer instability. It is shown that the downstream development of the triple jet was asymmetric. As the hot jet in the middle oscillated laterally, the interaction with one cold jet became stronger than the other cold jet. This flapping motion resulted in an asymmetric development of downstream mixing. As
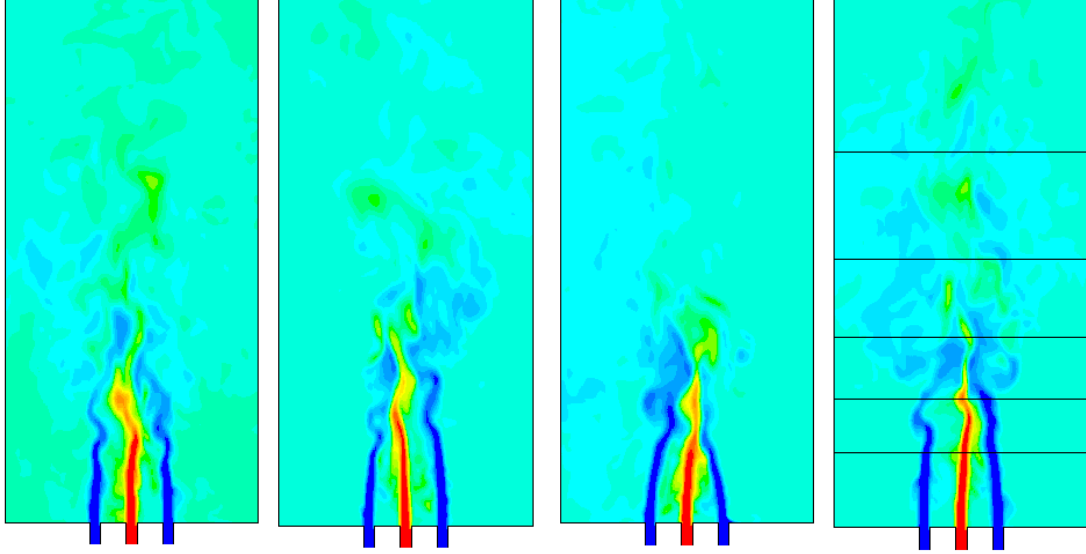
Figure A.6: Instantaneous temperature contour plots of LES results in the mid-plane at several time instants. Horizontal lines inserted indicate $y/D = 7$, 12, 18, 25 and 35. Red colour indicates hot fluid and blue colour cold fluid. Contour plot legend: High (Red), Low (Blue)
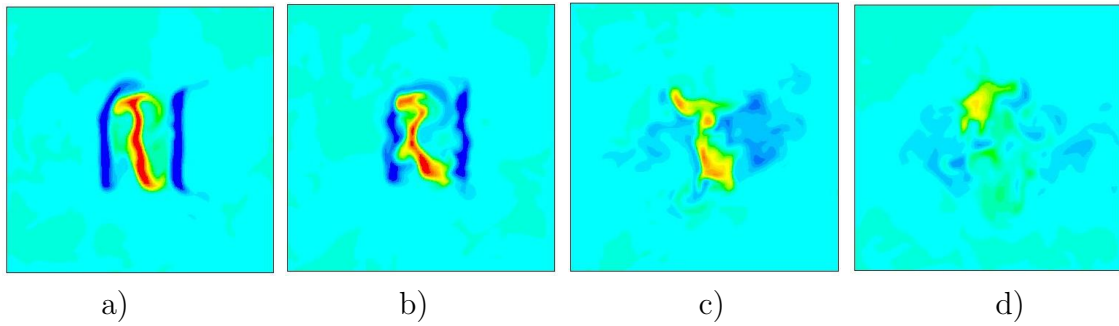
Figure A.7: Snapshots of temperature from the LES results at four cross sections, $y/D = 7$, 12, 18 and 25 from left to right, respectively. Red colour indicates hot fluid and blue colour cold fluid. Contour plot legend: High (Red), Low (Blue)

the lateral motion continues, the hot jet became closer to alternate cold jets and started to merge together (see also Figure A.7b).

Figure A.7 shows snapshots of the LES temperature at axial cross sections ($24D \times 24D$). Four downstream locations $y/D = 7$, 12, 18, and 25 were chosen to cover the whole range of mixing. As shown in Figure A.7a, the rectangular shape of the cold jets were still discernible at $x/D = 7$. The instability started to grow from the both ends of the rectangular jets, and the hot jet in the middle was no longer symmetric but rotated in an anti-clockwise direction. It is clearly seen in Figure A.7b that the
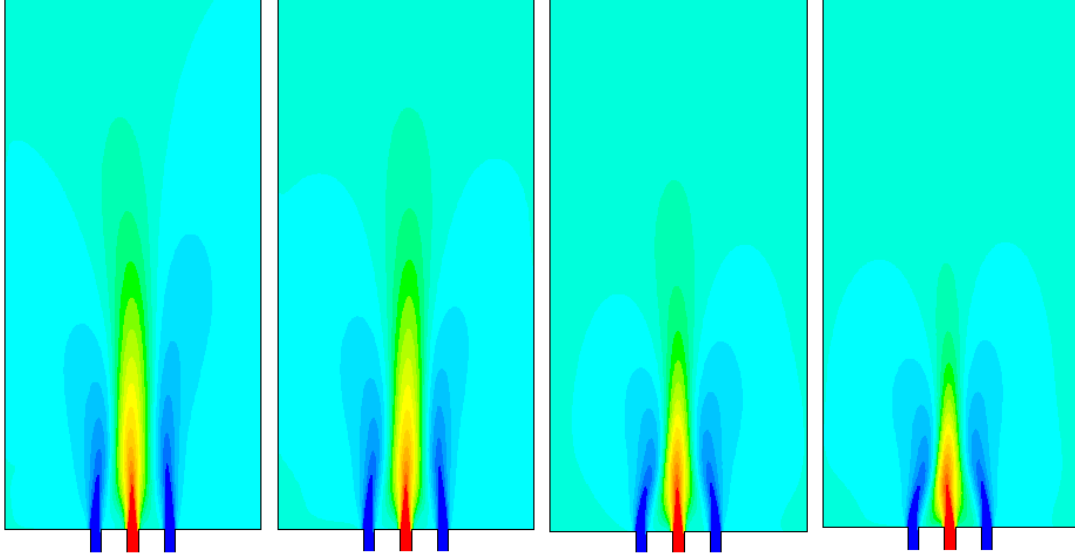
Figure A.8: Instantaneous temperature contour plots of the SA model in the mid-plane at several time instants. While colour indicates hot fluid and dark colour cold fluid. Contour plot legend: High (Red), Low (Blue)

flapping motion observed in Figure A.6 was not two dimensional: instead, the jet oscillated and rotated as they moved downstream. At $x/D = 12$, as the middle part of the hot jet moved to one side, the cold jet on the left hand side became weaker than the other cold jet due to a stronger interaction with the hot jet. As mixing continued further downstream, the hot jet interacted with the cold jets on both side and the initial rectangular shape was completely lost at $x/D = 18$. However, the mixing was still not completed at $x/D = 25$, and local areas of hot and cold fluids were visible in Figure A.7d.   Figures A.8 and A.9 represent snapshots of temperature in the mid-plane for the SA and realizable $k - \varepsilon$ models, respectively. The difference between the LES and the turbulence models is clearly seen. Small variations were visible in the figures but they looked rather similar to the time-averaged temperature field. Both turbulence models were unable to predict the dynamic and oscillatory nature of the triple jet as seen in the LES and experiments [135, 139].
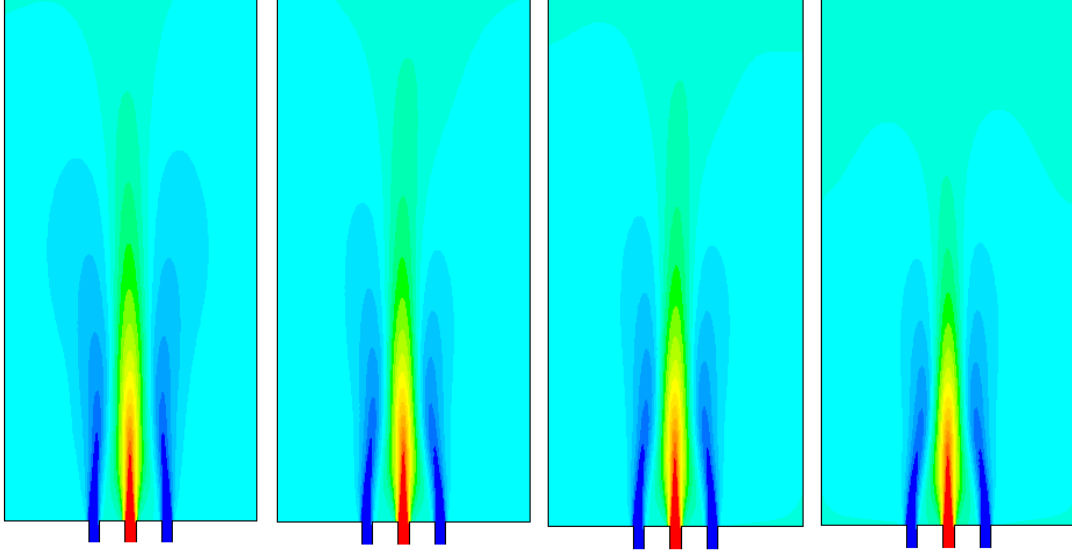
Figure A.9: Instantaneous temperature contour plots of the RNG $k - \varepsilon$ model in the mid-plane at several time instants. Contour plot legend: High (Red), Low (Blue)

A.5.3   Time mean quantities

The vertical mean velocity profiles across the triple jet in the mid-plane are presented in Figure A.10 at four downstream locations. The LES gave good overall agreement with the experimental data. The gradual transition of the triple jet until it merged into a single jet flow was well captured. At $y/D = 35$, the LES velocity profile looked very similar to a single jet profile, indicating that the mixing between the hot and cold jets were completed. The small difference between the LES and the experiment at $y/D = 35$ is due to the slight asymmetry in the experimental data. The realizable $k - \varepsilon$ model predicted a slower downstream mixing of triple jet, resulting in an over-prediction of the maximum velocity at $y/D = 35$. On the other hand, a faster mixing was predicted by the SA model. This is consistent with the flow field shown in Figures A.8 and A.9.

The mean temperatures profiles at the same downstream locations are plotted in Figure A.11. It can be seen that the LES predicted the mean temperature profile well. The agreement with the experiment was very good at $y/D = 12$ and 18. Further downstream at $y/D = 35$, the experimental temperature is significantly
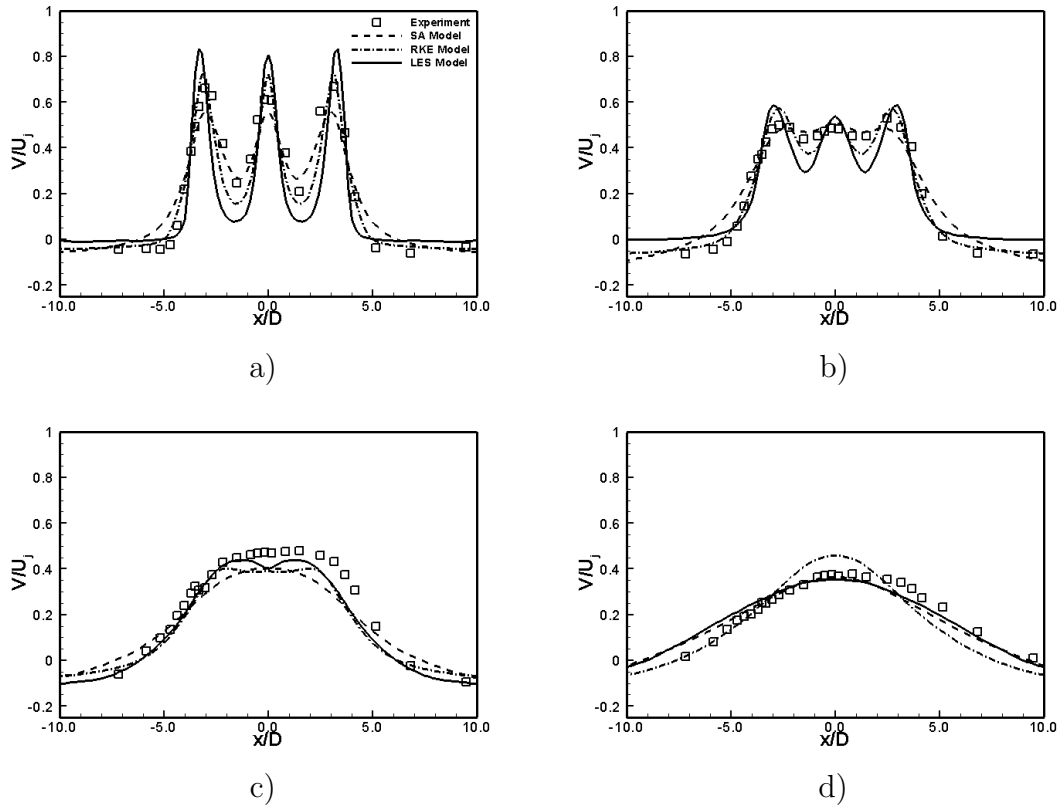
Figure A.10: The time-averaged velocity profiles in the mid-span at a) $y/D = 7$, b) $y/D = 12$, c) $y/D = 18$, and d) $y/D = 35$.
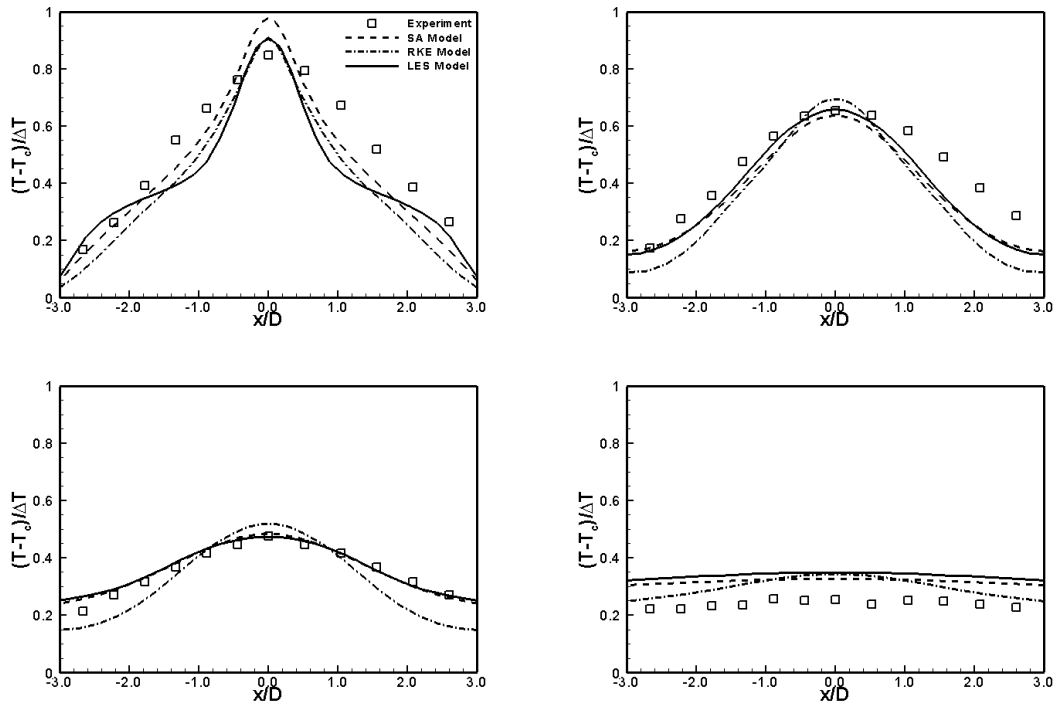
Figure A.11: The time-averaged temperature profiles in the mid-span at a) $y/D = 7$, b) $y/D = 12$, c) $y/D = 18$, and d) $y/D = 35$.
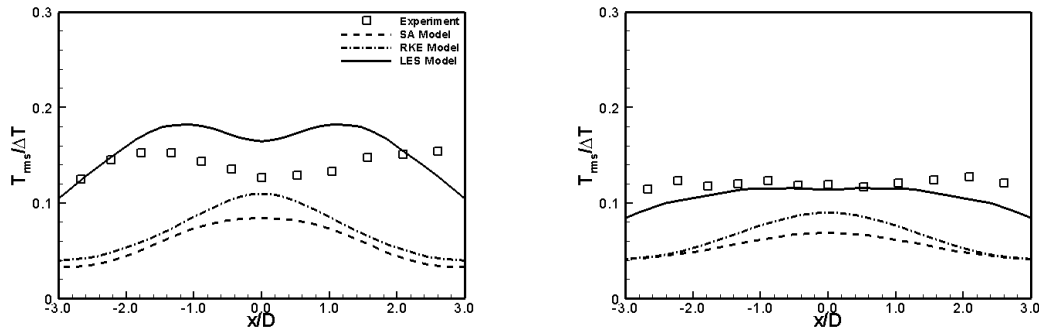
Figure A.12: The rms temperature fluctuation profiles in the mid-span at a) $y/D = 18$ and b) $y/D = 25$.

lower than the LES, and this is due to different thermal boundary conditions; an adiabatic condition was used in the simulations, whereas there was heat loss through the side walls in the experiment. The effect of adiabatic boundary condition became more evident further downstream as more heat was lost laterally. Again, the slower mixing of the realizable $k - \varepsilon$ model was evident at $y/D = 18$, where the maximum temperature was over-predicted.

A.6   Conclusion

In this study, numerical simulations of a non-isothermal triple jet flow were performed to assess the capability and accuracy of LES in thermal striping study. Three different grid resolutions were used, and our fine grid LES, which used a modest number of grid points, showed good agreement with the available experimental data. It is found that LES can predict the large amplitude of temperature fluctuations, which are essential information to analyse thermal striping phenomenon. This study clearly demonstrate the capability and potential of LES in the striping study. RANS simulations with two turbulence models were also conducted along with LES. The SA and realizable $k - \varepsilon$ turbulence models predicted the mean flow and thermal fields reasonably well, although an over-prediction of the maximum values was

observed with the realizable $k - \varepsilon$ turbulence model. However, the prediction of the temperature fluctuations by the two RANS models was very poor, indicating that LES not RANS is the appropriate tool to predict the coolant temperature fluctuations associated with high-Reynolds number turbulent thermal mixing in LMFR.

Bibliography

[1] V. Srinivasan. Batteries for vehicular applications. In *Physics of Sustainable Energy: Using Energy Efficiently and Producing It Renewably, AIP Conference Proceedings*, volume 1044, pages 283–296, Berkeley, CA, USA, 1-2 March, 2008.

[2] D. Linden and T. B. Reddy. *Lindens handbook of batteries*. McGraw Hill, 4th edition, 2011.

[3] S. Al Hallaj, R. Kizilel, A. Lateef, R. Sabbah, M. Farid, and J. R. Selman. Passive thermal management using phase change material (PCM) for EV and HEV Li-ion batteries.

[4] U. S. Kim, C. B. Shin, and C.-S. Kim. Modeling for the scale-up of a lithium-ion polymer battery. *Journal of Power Sources*, 189(1):841–846, 2009.

[5] N. Ford. 360 overview of the global passenger electric vehicle market. In *Sunderland International Automotive Conference*, Sunderland, UK, 20-21 April, 2010.

[6] A. Dinger, R. Martin, X. Mosquet, M. Rabi, D. Rizzoulis, M. Russo, and G. Sticher. Batteries for electric cars: Challenges, opportunities and the outlook to 2020. BCG Report, The Boston Consulting Group, 2010.

[7] A. A. Pesaran, A. Vlahinos, and T. Stuart. Cooling and preheating of batteries in hybrid electric vehicles. In *6th ASME-JSME Thermal Engineering Conference*, Hawaii, USA, 2003.

[8] EiG Battery. Product data sheets.

[9] S. Chacko and S. Charmer. An arrangement for battery thermal management. Patent application no. 1448/mum/2011 (India), Patent Pending, 2011.

[10] M. Wada. Research and development of electric vehicles for clean transportation. *Journal of Environmental Sciences*, 21(6):745–749, 2009.

[11] K. T. Chau, Y. S. Wong, and C. C. Chan. An overview of energy sources for electric vehicles. *Energy Conversion and Management*, 40(10):1021–1039, 1999.

[12] M. Simens, J. Jiminez, S. Hoyas, and Y. Mizuno. Plug-in hybrid fuel cell vehicles market penetration scenarios. *International Journal of Hydrogen Energy*, 35(18):10024–10030, 2010.

[13] S. Eaves and J. Eaves. A cost comparison of fuel-cell and battery electric vehicles. *Journal of Power Sources*, 130(1-2):208–212, 2004.

[14] G. G. Harding. Numerical calculation of time-dependent viscous incompressible flow of fluid with free surface. *Journal of Power Sources*, 78(1-2):193–208, 1999.

[15] C. E. Thomas. Fuel cell and battery electric vehicles compared. *International Journal of Hydrogen Energy*, 34(15):6005–6020, 2009.

[16] A. Cooper. Development of a lead-acid battery for a hybrid electric vehicle. *Journal of Power Sources*, 133(1):116–125, 2004.

[17] P. H. Andersen, J. A. Mathews, and M. Rask. Integrating private transport into renewable energy policy: The strategy of creating intelligent recharging grids for electric vehicles. *Energy Policy*, 37:2481–2486, 2009.

[18] P. A. Nelson, K. G. Gallagher, L. Bloom, and D. W. Dees. Modeling the performance and cost of Lithium-Ion batteries for electric vehicles. In *Argonne national laboratory report*, 2011.

[19] M. A. Delucchi and T. E. Lipman. An analysis of the retail and lifecycle cost of battery powered electric vehicles. *Transportation Research Part D*, 6:371–404, 2001.

[20] P. T. Moseley and A. Cooper. Progress towards an advanced lead-acid battery for use in electric vehicles. *Journal of Power Sources*, 78(1-2):244–250, 1999.

[21] P. T. Moseley. Characteristics of a high-performance lead/acid battery for electric vehicles - an ALABC view. *Journal of Power Sources*, 67(1):115–119, 1997.

[22] U. Kohler, J. Kumpers, and M. Ullrich. High performance nickel-metal hydride and lithium-ion batteries. *Journal of Power Sources*, 105(2):139–144, 2002.

[23] M. Zolot, A. A. Pesaran, and M. Mihalic. Thermal evaluation of Toyota Prius battery pack. In *Hyatt Crystal City: Future Car Congress*, 2002.

[24] S. K. Teo. Technological assessment and evaluation of high power batteries and their commercial values. Master's thesis, Massachusetts Institute of Technology, USA, 2006.

[25] B. Kennedy, D. Patterson, and S. Camilleri. Use of lithium-ion batteries in electric vehicles. *Journal of Power Sources*, 90(4):156–162, 2000.

[26] S. Megahed and W. Ebner. Lithium-ion battery for electronic applications. *Journal of Power Sources*, 54(155-162), 1995.

[27] L. Brooke. Cheverolet volt: Development story of the pioneering electrified vehicle. SAE International, 978-0-7680-4765-3, 2003.

[28] A. Madani. The EV & HEV market and trends - batteries. In *International Power Supply Conference and Exhibition*, French Rivera, 30 September - 2 October, 2009.

[29] A. Khaligh and Z. Li. Battery, ultracapacitors, fuel cell and hybrid energy storage systems for electric, hybrid electric, fuel cell and plug-in hybrid electric vehicles:State of the art. *IEEE*, 59(6):2806–2814, 2010.

[30] J. P. Aditya and M. Ferdowsi. Comparision of NiMH and Li-ion batteries in automotive applications. In *IEEE vehicle power and propulsion conference(VPPC)*, 2008.

[31] USABC battery test procedures. Version 2, USABC, 1996.

[32] C. Zhu and N. Nigro. Plug-In electric vehicle deployment in the northeast, a market overview and literature review. New York State Energy Research and Development Authority, New York, USA, 2012.

[33] G. Berdinchevsky, K. Kelty, J. B. Straubel, and E. Toomre. The tesla roadster battery system. Internal report, Tesla Motors, 2006.

[34] J. Nguyen and C. Taylor. Safety performance for phosphate based large format lithium-ion battery. In *26th Annual International Telecommunications Energy Conference*, pages 146–148, 2004.

[35] R. B. Wright, J. P. Christophersen, C. G. Motloch, J. R. Belt, C. D. Ho, V. S. Battaglia, J. A. Barnes, T. Q. Duong, and R. A. Sutula. Power fade and capacity fade resulting from cycle-life testing of advanced technology development program lithium-ion batteries. *Journal of Power Sources*, 119(SI):865–869, 2003.

[36] R. B. Wright, C. G. Motloch, J. R. Belt, J. P. Christophersen, C. D. Ho, R. A. Richardson, I. Bloom, S. A. Jones, V. S. Battaglia, G. L. Henriksen, T. Unkelhaeuser, D. Ingersoll, H. L. Case, S. A. Rogers, and R. A. Sutula. Calendar- and cycle-life studies of advanced technology development program generation 1 lithium-ion batteries. *Journal of Power Sources*, 110(2):445–470, 2002.

[37] Z. Zhang, L. Zhang, K. Youssef, and K. Amine. Advanced electrolyte additives for phev/ev lithium-ion battery. *Vehicle Technologies Program Annual Merit Review and Peer Evaluation Meeting*, 2012.

[38] W. A. V. Schalkwijk and B. Scrosati. *Advances in Lithium-Ion Batteries.* Plenum Publishers, 1st edition, 2002.

[39] Y. Kida, k. Yanagida, A. Funahashi, T. Nohma, and I. Yonezu. Electrochemical characteristics of graphite, coke and graphite/coke hybrid carbon as negative electrode materials for lithium secondary batteries. *Journal of Power Sources*, 94:74–77, 2001.

[40] C. R. Park. *Next generation lithium ion batteries for electrical vehicles*, volume 1. In-Teh publishers, 2010.

[41] M. Root. *The TAB Battery Book, An In-Depth Guide to Construction, Design, and Use*, volume 1. The McGraw-Hill, 2011.

[42] Y. Chen and J. Evans. 3-dimensional thermal modeling of lithium-polymer batteries under galvanostatic discharge and dynamic power profile. *Journal of Electrochemical Society*, 141(11):2947–2955, 1994.

[43] C. G. Motloch, J. P. Christophersen, J. R. Belt, R. B. Wright, G. L. Hunt, R. A. Sutula, T. Q. Duong, T. J. Tartamella, H. J. Haskins, and T. J. Miller. High-power battery testing procedures and analytical methodologies for HEVs. SAE International, 2002-01-1950, 2002.

[44] S. Chacko and S. Charmer. Concept development and CAE for EV battery thermal management. In *IMechE Conference VTMS10*, pages C1305–028, Gaydon, UK, 2011.

[45] V. Johnson, A. Pesaran, and T. Sack. Charging algorithms for increasing lead acid battery cycle life for electric vehicles. In *17th Electric Vehicle Symposium*, Montreal, Canada, 2000.

[46] J. Newman. *Electrochemical Systems*. Prentice-Hall, Englewood Cliffs, NJ, USA, 1st edition, 1973.

[47] J. S. Newman. *Electrochemical Systems*. Prentice-Hall, Englewood Cliffs, NJ, USA, 2nd edition, 1991.

[48] J. Newman and K. E. Thomas-Alyea. *Electrochemical Systems*. Wiley-Interscience, 3rd edition, 2004.

[49] C. M. Shepherd. Design of primary and secondary cells. I. Effect of polarization and resistance on cell charcteristics. *Journal of Electrochemical Society*, 112(3):252–257, 1965.

[50] C. M. Shepherd. Design of primary and secondary cells. II. An equation describing battery discharge. *Journal of Electrochemical Society*, 112(7):657–664, 1965.

[51] H. A. Kiehne. *Battery technology handbook*. Expert Verlag, 2003.

[52] B. V. Ratnakumar, M. C. Smart, G. Halpert, A. Kindler, H. Frank, S. Di Stefano, R. Ewell, and S. Surampudi. Lithium batteries on 2003 Mars Rover. In *17th Annual Battery Conference on Applications and Advances*, pages 47–51, 15-18 January, 2002.

[53] J. Yamaki, M. Ihara, and S. Okada. Improvement of thermal stability of lithium ion batteries by using methyl difluoroacetate as an electrolyte solvent.

In *25th Annual International Telecommunications Energy Conference*, pages 59–65, 19-23 October, 2003.

[54] K. White, Q. Horn, S. Singh, R. Spray, and N. Budiansky. Thermal stability of lithium-ion cell as function of chemistry, design and energy. In *Proceedings,28th International Battery Seminar and Exhibit*, Lauderdale, Florida, March 14-17, 2011.

[55] A. A. Pesaran and M. Keyser. Thermal characteristics of selected EV and HEV batteries. In *16th Annual Battery Conference on Applications and Advances*, pages 219–225, Hawaii, USA, 2001.

[56] P. M. Gomadam, J. W. Weidner, R. A. Dougal, and R. E. White. Mathematical modeling of lithium-ion and nickel battery systems. *Journal of Power Sources*, 110(2):267–284, 2002.

[57] H. Maleki, G. Deng, A. Anani, and J. Howard. Thermal stability studies of Li-ion cells and components. *Journal of Electrochemical Society*, 146:3224–3239, 1999.

[58] K. Brandt. Historical developments of secondary lithium batteries. *Solid State Ionics*, 69:172–183, 1994.

[59] H. Huang, T. Faulkner, J. Barker, and M. Y. Saidi. Lithium metal phosphates, power and automotive applications. *Journal of Power Sources*, 189:748–751, 2009.

[60] S. Chacko and S. Charmer. Lithium-ion thermal modeling and evaluation of indirect liquid cooling for electric vehicle battery thermal management. In *Innovations in Fuel Economy and Sustainable Road Transport*, C1321, Pune, India, 2011.

[61] International Electrotechnical Commission (IEC). Secondary lithium-ion cells for the propulsion of electric road vehicles - Part 1: Performance testing. IEC 62660-1:2010, Copyright 2010 IEC, Geneva, Switzerland.

[62] C.-W. Park and A. K. Jaura. Dynamic thermal model of Li-ion battery for predictive behavior in hybrid and fuel cell vehicles. SAE International, 2003-01-2286, 2003.

[63] R. Mahamud and C. Park. Reciprocating air flow for Li-ion battery thermal management to improve temperature uniformity. *Journal of Power Sources*, 196:5685–5696, 2011.

[64] J.-P. Semerie. Lithium-ion batteries for geosynchronous satellites. Qualification test results of the STENTOR battery. In *35th Intersociety Energy Conversion Engineering Conference and Exhibit*, volume 1, pages 621–628, 24-28 July, Las Vegas, NV, USA, 2000.

[65] J. R. Selman, S. Al Hallaj, I. Uchida, and Y. Hirano. Cooperative research on safety fundamentals of lithium batteries. *Journal of Power Sources*, 97:726–732, 2001.

[66] Y. Saito. Thermal behaviors of lithium-ion batteries during high-rate pulse cycling. *Journal of Power Sources*, 146(1-2):770–774, 2005.

[67] K. Tamura and T. Horiba. Large-scale development of lithium batteries for electric vehicles and electric power storage applications. *Journal of Power Sources*, 82:156–161, 1999.

[68] R. Sabbah, R. Kizilel, J. R. Selman, and S. Al Hallaj. Active (air-cooled) vs. passive (phase change material) thermal management of high power lithium-ion packs: limitation of temperature rise and uniformity of temperature distribution. *Journal of Power Sources*, 182(2):630–638, 2008.

[69] A. A. Pesaran. Battery thermal models for hybrid vehicle simulations. *Journal of Power Sources*, 110(2):377–382, 2002.

[70] N. Sato. Thermal behavior analysis of lithium-ion batteries for electric and hybrid vehicles. *Journal of Power Sources*, 99(1-2):70–77, 2001.

[71] R. Kizilel, R. Sabbah, J. R. Selman, and S. Al-Hallaj. An alternative cooling system to enhance the safety of Li-ion battery packs. *Journal of Power Sources*, 194(2):1105–1112, 2009.

[72] A. N. Jansen, D. W. Dees, D. P. Abraham, K. Amine, and G. L. Henriksen. Low-temperature study of lithium-ion cells using a liysn micro-reference electrode. *Journal of Power Sources*, 174(2):373–379, 2007.

[73] P. Nelson, D. Dees, K. Amine, and G. Henriksen. Modeling thermal management of lithium-ion PNGV batteries. *Journal of Power Sources*, 110(2):349–356, 2002.

[74] Y. Lou. Nickel-metal hydride battery cooling system research for hybrid electric vehicle. Report, (in Chinese), Shanghai Jiao Tong University, 2007.

[75] M. S. Wu, K. H. Liu, Y. Y. Wang, and C. C. Wan. Heat dissipation design for lithium-ion batteries. *Journal of Power Sources*, 109(1):160–166, 2002.

[76] Y. Chen and J. Evans. Heat transfer phenomena in lithium/polymer-electrolyte batteries for electric vehicle applications. *Journal of Electrochemical Society*, 140(7):1833–1838, 1993.

[77] A. A. Pesaran. Battery thermal management in EVs and HEVs: Issues and solutions. In *Advanced automotive battery conference*, Las Vegas, Nevada, 2001.

[78] A. A. Pesaran, A. Burch, and T. Keyser. An approach for designing thermal management systems for electric and hybrid vehicle battery packs. In *Fourth*

vehicle thermal management systems conference and exhibition, London, UK, 1999.

[79] S. Jayaraman, G. Anderson, S. Kaushik, and P. Klaus. Modeling of battery pack thermal system for a plug-in hybrid electric vehicle. SAE International, 2011-01-0666, 2011.

[80] R. S. Gaugler. Heat pipe. US Patent:2350348, 1944.

[81] J.-C. Jang and S.-H. Rhi. Battery thermal management system of future electric vehicles with loop thermosyphon. In *US-Korea Conference on Science, Technology, and Entrepreneurship (UKC)*, Seattle, WA, USA, 2010.

[82] S. A. Khateeb, M. M. Farid, J. R. Selman, and S. Al-Hallaj. Design and simulation of a lithium-ion battery with a phase change material thermal management system for an electric scooter. *Journal of Power Sources*, 128(2):292–307, 2004.

[83] S. Al Hallaj and J. R. Selman. A novel thermal management system for EV batteries using phase change material (PCM). *Journal of Electrochemical Society*, 147:3231–3236, 2000.

[84] S. Al Hallaj and J. R. Selman. Thermal modeling of secondary lithium batteries for electric vehicle/hybrid electric vehicle applications. *Journal of Power Sources*, 110:341–348, 2002.

[85] A. Mills and S. Al-Hallaj. Simulation of passive thermal management system for lithium-ion battery packs. *Journal of Power Sources*, 141(2):307–315, 2005.

[86] S. A. Khateeb, S. Amiruddin, M. M. Farid, J. R. Selman, and S. Al-Hallaj. Thermal management of Li-ion battery with phase change material for electric scooters: experimental validation. *Journal of Power Sources*, 142(2):345–353, 2005.

[87] R. Kizilel, A. Lateef, R. Sabbah, M. M. Farid, J. R. Selman, and Al. S. Hallaj. Passive control of temperature excursion and uniformity in high-energy Li-ion battery packs at high current and ambient temperature. *Journal of Power Sources*, 183(1):370–385, 2008.

[88] T. M. Bandhauer, S. Garimella, and T. F. Fuller. A critical review of thermal issues in lithium-ion batteries. *Journal of Electrochemical Society*, 158(3):R1–R25, 2011.

[89] M. Doyle, T. F. Fuller, and J. Newman. Modeling of galvanostatic change and discharge of the lithium/polymer/insertion cell. *Journal of Electrochemical Society*, 140(6):1526–1533, 1993.

[90] M. Doyle, J. Newman, A. S. Gozdz, C. N. Schmutz, and J. M. Tarascon. Comparison of modeling predictions with experimental data from plastic lithium ion cells. *Journal of Electrochemical Society*, 143:1890–1903, 1996.

[91] T. F. Fuller, M. Doyle, and J. Newman. Simulation and optimization of the dual lithium ion insertion cell. *Journal of Electrochemical Society*, 141(1):1–10, 1994.

[92] K. H. Kwon, C. B. Shin, T. H. Kang, and C.-S. Kim. A two-dimensional modeling of lithium-polymer battery. *Journal of Power Sources*, 163(1):151–157, 2006.

[93] D. Bernardi, E. Pawlikowski, and J. Newman. A general energy balance for battery systems. *Journal of Electrochemical Society*, 132(1):5–12, 1985.

[94] W. B. Gu and C. Y. Wang. Thermal-electrochemical modeling of battery systems. *Journal of Electrochemical Society*, 147:2910–2922, 2000.

[95] C. R. Pals and J. Newman. Thermal modeling of the lithium/polymer battery.

II. Temperature profiles in a cell stack. *Journal of Electrochemical Society*, 142(10):3282–3288, 1995.

[96] E. Barsoukov and J. R. MacDonald. *Impedance Spectroscopy: Theory, Experiment, and Applications*. Wiley-Interscience, 2nd edition, 2005.

[97] T. K. Dong, A. Kirchev, F. Mattera, J. Kowal, and Y. Bultel. Dynamic modeling of Li-ion batteries using an equivalent electrical circuit. *Journal of Electrochemical Society*, 158(3):A326–A336, 2011.

[98] J. Gomez, R. Nelson, E. E. Kalu, M. H. Weatherspoon, and J. P. Zheng. Equivalent circuit model parameters of a high-power Li-ion battery: Thermal and state of charge effects. *Journal of Power Sources*, 196(10):4826–4831, 2011.

[99] C. R. Pals and J. Newman. Thermal modeling of the lithium/polymer battery. I. Discharge behavior of a single cell. *Journal of Electrochemical Society*, 142(10):3274–3281, 1995.

[100] H. Gu. Mathematical analysis of a Zn/NiOOH cell. *Journal of Electrochemical Society*, 130:1459–1464, 1983.

[101] W. Tiedemann and J. Newman. Nonuniform current and potential distribution in composite sheet type battery electrodes. *Journal of Electrochemical Society*, 126(8):C323–C323, 1979.

[102] Y. Chen and J. Evans. Thermal-analysis of lithium polymer electrolyte batteries by a 2-dimensional model - thermal behavior and design optimization. *Electrochemica Acta*, 39(4):517–526, 1994.

[103] J. Lee, K. W. Choi, N. P. Yoo, and C. C. Christianson. 3-dimensional thermal modeling of electric vehicle-batteries. *Journal of Electrochemical Society*, 133(7):1286–1291, 1986.

[104] L. Song and J. W. Evans. Electrochemical-thermal model of lithium polymer batteries. *Journal of Electrochemical Society*, 147(6):2086–2095, 2000.

[105] U. S Kim, J. Yi, C. B. Shin, T. Han, and S. Park. Modeling the thermal behavior of a lithium-ion battery during charge. *Journal of Power Sources*, 196(11):5115–5121, 2011.

[106] S. C. Chen, C. C. Wan, and Y. Y. Wang. Thermal analysis of lithium-ion batteries. *Journal of Power Sources*, 140:111–124, 2005.

[107] J. Newman and W. Tiedemann. Potential and current distribution in electrochemical cells. Interpretation of the half-cell voltage measurements as a function of reference-electrode location. *Journal of Electrochemical Society*, 140(7):1961–1968, 1993.

[108] C. Y. Wang and V. Srinivasan. Computational battery dynamics (CBD) - electrochemical/thermal coupled modeling and multi-scale modeling. *Journal of Power Sources*, 110(2):364–376, 2002.

[109] U. S. Kim, C. B. Shin, and C.-S. Kim. Effect of electrode configuration on the thermal behavior of a lithium-polymer battery. *Journal of Power Sources*, 180(2):909–916, 2009.

[110] L. Rao and J. Newman. Heat-generation rate and general energy balance for insertion battery systems. *Journal of Electrochemical Society*, 144(8):2697–2704, 1997.

[111] K. Smith and C.-Y. Wang. Power and thermal characterization of a lithium-ion battery pack for hybrid-electric vehicles. *Journal of Power Sources*, 160:662–673, 2006.

[112] Tata Motors European Technical Centre (TMETC). Hot environment test. Internal and confidential report, 2011.

[113] S. H. Yu, S. Sohn, J. H. Nam, and C.-J. Kim. Numerical study to examine the performance of multi-pass serpentine flow-fields for cooling plates in polymer electrolyte membrane fuel cells. *Journal of Power Sources*, 194(2):697–703, 2009.

[114] J. C. Kurnia, A. P. Sasmito, and A. S. Mujumdar. Numerical investigation of laminar heat transfer performance of various cooling channel designs. *Appled Thermal Engineering*, 31(6-7):1293–1304, 2011.

[115] W. M. Rohsenow, J. P. Hartnett, and E. N. Ganic. *Handbook of Heat Transfer Applications*. McGraw-Hill, New York, 1985.

[116] C. B. Sobhan and S. V. Garimella. A comparative analysis of studies on heat transfer and fluid flow in microchannels. *Microscale Thermophysical Engineering*, 5(4):293–311, 2001.

[117] F. C. Chen, Z. Gao, R. O. Loutfy, and M. Hecht. Analysis of optimal heat transfer in a PEM fuel cell cooling plate. *Fuel Cells*, 3(4):181–185, 2004.

[118] H. S. Kou, J. J. Lee, and C. W. Chen. Optimum thermal performance of micro channel heat sink by adjusting channel width and height. *International Communications in Heat and Mass Transfer*, 35(5):577–582, 2008.

[119] J. Yuan, M. Rokni, and B. Sunden. Simulation of fully developed laminar heat and mass transfer in fuel cell ducts with different cross sections. *International Journal of Heat and Mass Transfer*, 44:4047–4058, 2001.

[120] P. S. Lee and S. V. Garimella. Thermally developing flow and heat transfer in rectangular microchannels of different aspect ratios. *International Journal of Heat and Mass Transfer*, 49(17-18):3060–3067, 2006.

[121] X. L. Xie, Z. J. Liu, Y. L. He, and W. Q. Tao. Numerical study of laminar

heat transfer and pressure drop characteristics in a water-cooled minichannel heat sink. *Appled Thermal Engineering*, 29(1):64–74, 2009.

[122] Fluent. *version 6.3.26, documentation.*

[123] Ansys. *ICEM CFD Hexa 12.0, documentation.*

[124] R. K. Shah and A. L. London. *Laminar flow forced convection in ducts: A source book for compact heat exchanger analytical data.* New York: Academic Press, 1st edition, 1978.

[125] Y. M. Chung, P. G. Tucker, and D. G. Roychowdhury. Unsteady laminar flow and convective heat transfer in a sharp 180°bend. *International Journal of Heat and Fluid Flow*, 24(1):67–76, 2003.

[126] P. Hille, R. Vehrenkamp, and E. O. Schulz-Dubois. The development and structure of primary and secondary flow in a curved square duct. *Journal of Fluid Mechanics*, 151:219–241, 1985.

[127] K. N. Ghia and J. S. Sokhey. Laminar incompressible viscous flow in curved ducts of regular cross-sections. *ASME: Journal of Fluids Engineering*, 99:640–648, 1977.

[128] H. K. Moffat. Helicity in laminar and turbulent flow. *Annual Review of Fluid Mechanics*, 24:281–312, 1992.

[129] Y. Y. Levy, D. Degani, and A. Seginer. Graphical visualization of vortical flows by means of helicity. *AIAA Journal*, 28(8):1347–1352, 1990.

[130] P. Chellapandi, S. C. Chetal, and B. Raj. Thermal striping limits for components of sodium cooled fast spectrum reactors. *Nuclear Engineering and Design*, 239(12):2754–2765, 2009.

[131] M. Wakamatsu, H. Nei, and K. Hashiguchi. Attenuation of temperature fluctuations in thermal striping. *Journal of Nuclear Science and Technology*, 32(8):752–762, 1995.

[132] J. P. Moro and D. Tenchine. Mixing of coaxial jets: Comparison of sodium and air experiments. In *IAEA International Working Group on Fast Reactors, Specialist Meeting on Correlation Between Material Properties and Thermo-Hydraulics Conditions in LMFBRs*, pages 1/16–6/16, 1994.

[133] D. Tenchine and J. P. Moro. Experimental and computational study of turbulent mixing jets for nuclear reactors applications. ISTP-12, 16-20 July, Istanbul, Turkey, 2000.

[134] D. Tenchine. Some thermal hydraulic challenges in sodium cooled fast reactors. *Nuclear Engineering and Design*, 240(5):1195–1217, 2010.

[135] A. Tokuhiro and N. Kimura. An experimental investigation on thermal striping: Mixing phenomena of a vertical non-buoyant jet with two adjacent buoyant jets as measured by ultrasound doppler velocimetry. *Nuclear Engineering and Design*, 188(1):49–73, 1999.

[136] N. Kimura, H. Miyakoshi, and H. Kamide. Experimental investigation on transfer characteristics of temperature fluctuation from liquid sodium to wall in parallel triple-jet. *International Journal of Heat and Mass Transfer*, 50(9-10):2024–2036, 2007.

[137] H. Y. Nam and J. M. Kim. Thermal striping experimental data. Internal report LMR/IOC-ST-002-04-Rev.0/04, KAERI, 2004.

[138] S. Ushijima, N. Tanaka, and S. Moriya. Turbulence measurements and calculation of non-isothermal coaxial jets. *Nuclear Engineering and Design*, 122(1-3):85–94, 1990.

[139] M. Nishimura, A. Tokuhiro, N. Kimura, and H. Kamide. Numerical study on mixing of oscillating quasi-planar jets with low Reynolds number turbulent stress and heat flux equation models. *Nuclear Engineering and Design*, 202(1):77–95, 2000.

[140] N. Kimura, M. Nishimura, and H. Kamide. Study on convective mixing for thermal striping phenomena (Experimental analyses on mixing process in parallel triple-jet and comparisons between numerical methods). *JSME International Journal Series B*, 45(3):592–599, 2002.

[141] M. Nishimura and N. Kimura. URANS computations for an oscillatory non-isothermal triple-jet using the $k - \varepsilon$ and second moment closure turbulence models. *International Jounal for Numerical Methods in Fluids*, 43(9):1019–1044, 2003.

[142] S.-K. Choi and S.-O. Kim. Evaluation of turbulence models for thermal striping in a triple jet. *ASME: Journal of Pressure Vessel Technology*, 129(4):583–592, 2007.

[143] G. Medic and P. A. Durbin. Toward improved prediction of heat transfer on turbine blades. *ASME: Journal of Turbomachinery*, 124(2):187–192, 2002.

[144] G. Grötzbach and M. Wörner. Direct numerical and large eddy simulations in nuclear applications. *International Journal of Heat and Fluid Flow*, 20(3):222–240, 1999.

[145] J.-P. Simoneau, J. Champigny, and O. Gelineau. Applications of large eddy simulations in nuclear field. *Nuclear Engineering and Design*, 240(2):429–439, 2010.

[146] P. R. Spalart and S. R. Allmaras. A one-equation turbulence model for aerodynamic flows. In *30th AIAA Aerospace Sciences Meeting and Exhibit, Reno, NV, USA*, AIAA Paper 92-0439, 1992.

[147] T.-H. Shih, W. W. Liou, A. Shabbir, Z. Yang, and J. Zhu. A new $k - \varepsilon$ eddy viscosity model for high reynolds number turbulent flows: Model development and validation. *Computers and Fluids*, 24(3):227–238, 1995.

[148] R. I. Issa. Solution of the implicitly discretised fluid flow equations by operator-splitting. *Journal of Computational Physics*, 62(1):40–65, 1986.

[149] H. C. Chen and V. C. Patel. Near-wall turbulence models for complex flows including separation. *AIAA Journal*, 26(6):641–648, 1988.

[150] F. R. Menter. Two equation eddy-viscosity turbulence models for engineering applications. *AIAA Journal*, 32(8):1598–1604, 1994.

[151] P. Catalano, M. Wang, G. Iaccarino, and P. Moin. Numerical simulation of the flow around a circular cylinder at high reynolds numbers. *International Journal of Heat and Fluid Flow*, 24(4):463–469, 2003.